Distribution Agreement

In presenting this thesis or dissertation as a partial fulfillment of the requirements for an advanced degree from Emory University, I hereby grant to Emory University and its agents the non-exclusive license to archive, make accessible, and display my thesis or dissertation in whole or in part in all forms of media, now or hereafter known, including display on the world wide web. I understand that I may select some access restrictions as part of the online submission of this thesis or dissertation. I retain all ownership rights to the copyright of the thesis or dissertation. I also retain the right to use in future works (such as articles or books) all or part of this thesis or dissertation.

Signature:

_____   _____

Shanshan Li   Date

Renormalization Group in Dynamical Processes on Hierarchical Networks

By

Shanshan Li

Doctor of Philosophy

Physics

Stefan Boettcher
Advisor

Michele Benzi
Committee Member

H. George E. Hentschel
Committee Member

Ilya Nemenman
Committee Member

Sergei Urazhdin
Committee Member

Accepted:

Lisa A. Tedesco, Ph.D.
Dean of the James T. Laney School of Graduate Studies

Date

Renormalization Group in Dynamical Processes on Hierarchical Networks

By Shanshan Li

Advisor: Stefan Boettcher, Ph.D.

An abstract of a dissertation submitted to the Faculty of the

James T. Laney School of Graduate Studies of Emory University

in partial fulfillment of the requirements for the degree of

Doctor of Philosophy in Physics, 2017

Abstract

Renormalization Group in Dynamical Processes on Hierarchical Networks

By Shanshan Li

Hierarchical structures have been found in actual complex systems. Certain hierarchical networks, with a self-similar structure, exhibit novel properties in a broader spectrum of dynamics such as synchronization, quantum walks and the epidemic process, which we explore in this thesis by applying analytical and numerical methods. We study the structural and spectral properties of large scale networks, as well as various phenomena on them with the Renormalization Group (RG) approach. In particular, by applying RG, we explore the Laplacian spectrum, which is related to asymptotic structural features of networks, ranging from the number of spanning trees to synchronizability. The spectral analysis also reveals a deep connection between dynamics and the underlying structure in processes that include quantum walks and the unusual Griffiths phase on hierarchical networks considered in this thesis. This thesis highlights effects of spectral properties on dynamical processes on networks, and indicates the applicability of RG to various contexts.

Renormalization Group in Dynamical Processes on Hierarchical Networks

By Shanshan Li

Advisor: Stefan Boettcher, Ph.D.

A dissertation submitted to the Faculty of the

James T. Laney School of Graduate Studies of Emory University

in partial fulfillment of the requirements for the degree of

Doctor of Philosophy in Physics, 2017

Contents

List of Figures

6

List of Tables

Chapter 1

Introduction

Networks dominate research on the identification and characterization of the system-level organization in complex systems. A discrete function of a complex system can be rarely attributed to any individual component. It arises from the complicated interactions of numerous components. It is a key issue to understand the structure of the interaction web that contributes to the organization and function of a system. Complicated patterns of interactions can be qualitatively described by various type of networks. The remarkable discovery in network science is that despite of the rich nature of complex systems, the architecture of networks is determined by simple principles that many networks share [13]. Simplest graphs include lattices, hypercubes, complete graphs, and Erdös Renyi graphs (we also note random networks interchangeably). In particular, random networks can be a naive model for complex systems, which have a remarkable feature on the distribution of node degrees, i.e. a Poisson distribution. Despite of the simplicity and elegance of random networks, they cannot capture the topology of real networks including many of scientific and technological networks, ranging from the World Wide Web (WWW) to biological networks.

A distinguishing feature is that many real networks follow a power law distribution of the node degree, i.e. the probability that a randomly selected node has k edges (i.e. degree k) follows $P(k) \sim k^{-\gamma}$ with the degree exponent γ. The value of γ for real networks lies between 2 and 3 [12]. This characteristics is captured by the scale free networks [6]. Scale free networks are highly heterogeneous. The whole network is integrated by a few existing highly connected nodes, also called hubs. It contradicts random networks where the average node degree are considered as typical. Another significant feature of real networks is the small-world topology, i.e. the average of shortest path lengths between any

pair of nodes follows logarithmically with the network size, i.e. $l \sim \ln N$. Random networks are small world, and scale-free networks with $\gamma \in (2, 3)$ are ultra-small, i.e. $l \sim \ln \ln N$ [46]. Small diameters of networks indicates local perturbations could reach the whole network quickly.

Definition of shortest path length

$$l = \frac{1}{N(N-1)} \sum_{x \neq y} d_{xy}, \tag{1.1}$$

where d_{xy} is the shortest distance between node x and y.

Scale-free networks originate from the network evolution and preferential attachment where highly connected nodes gain more edges than the less connected nodes [11]. In biological networks such as metabolic and protein interaction, and technological networks such as WWW, a dis-assortative nature exists. Highly connected nodes avoid linking directly to each other and instead connect to numerous nodes within a few edges [87]. Modular function is seen in these cellular networks, Internet, and social networks. A module is a group of nodes that are densely connected, whereas inter-module connections are rather sparse. In the network characteristics, a high clustering coefficient is a signature for the potential modularity. The average clustering coefficient $\langle C \rangle$ of real networks is independent of the network size N, and obviously higher than that of random networks of the same size and average degree, i.e. $\langle C \rangle \sim \langle k \rangle / N$.

Definition of clustering coefficient

$$C_x = 2n_x / [k_x (k_x - 1)]$$

where k_x is the number of neighbors for node x, $[k_x (k_x - 1)]/2$ is the number of allowable edges between them, and n_x is the number of existing edges [135].

The coexistence of scale-free property and modularity is found in protein interaction networks [132], WWW [115, 6] and social networks [95]. As an example, let us consider the cellular network to show a typical combination of the scale-free property, the dis-assortative nature and high clustering. In cellular metabolism, metabolic substrates are densely interconnected via biochemical reactions.

The probability that a substrate can react with other k substrates follows a a power law decay [133], suggesting a scale-free topology. Simultaneously, the analysis on functional capabilities and the pure topology of metabolic networks suggests the existence of separable functional elements and high clustering [118, 133]. However, clear-cut modular structures that compose densely connected modules while interconnected with others through a few edges impose restrictions on the degree distribution. Modules in biological networks and communities in social networks [45] by definition are relatively isolated from the rest of the system, whereas in the scale free topology, hubs connect a high fraction of nodes. The scale-free property and modularity are not exclusive for a large number of real networks. This dilemma is fixed by considering the hierarchical organization, a generic structure in real systems. Hierarchical networks capture the topology of diverse systems where groups of densely connected components exist in multiple scales, and they are not independent [114, 115].

Hierarchical modularity exhibit a high degree of clustering that is regarded as a sign for modularity. Hierarchical organization is investigated on several real networks in [114], which shows the clustering coefficient depends on the degree of a node $C_k \sim k^{-1}$. It indicates that nodes that have a few edges is highly interconnected inside modules, whereas hubs that have numerous edges play the role of linking different modules and they have a low clustering coefficient. Hierarchical modularity is proposed as a model for certain networks that reconciles the scale-free topology, high and size-independent clustering coefficient, and the power law scaling of C_k [115]. Such an model is shown in Fig.(1.1.a).

The existence of hierarchy is consistent with the small-world property [45]. Many real networks are small-world networks, whereas there also exist various systems that possess a large-world architecture, such as lattices and numerous fractals. Alternatively, the scaling of the shortest path lengths l with the network size N can be measured by the fractal dimension d_f. It describes the number of nodes that can be reached from a starting node within l steps, averaged over all initial nodes, i.e. $N \sim l^{d_f}$. Quantifying the average of shortest path lengths with d_f, small-world networks have a fractal dimension $d_f \to \infty$.

Although networks that model the real systems often have the stochastic nature, hierarchical structures can be a result of deterministic construction procedures [14]. The framework of deterministic iterations produces various classes of hierarchical structures. With different rules of construction, it is easy to tune network characteristics. One example is pseudo fractals that are generated via iterations [53]. They are the apparent but not actual self-similar hierarchical networks, providing excellent models of random scale-free networks and lending themselves to exact analytic treatment. One graph
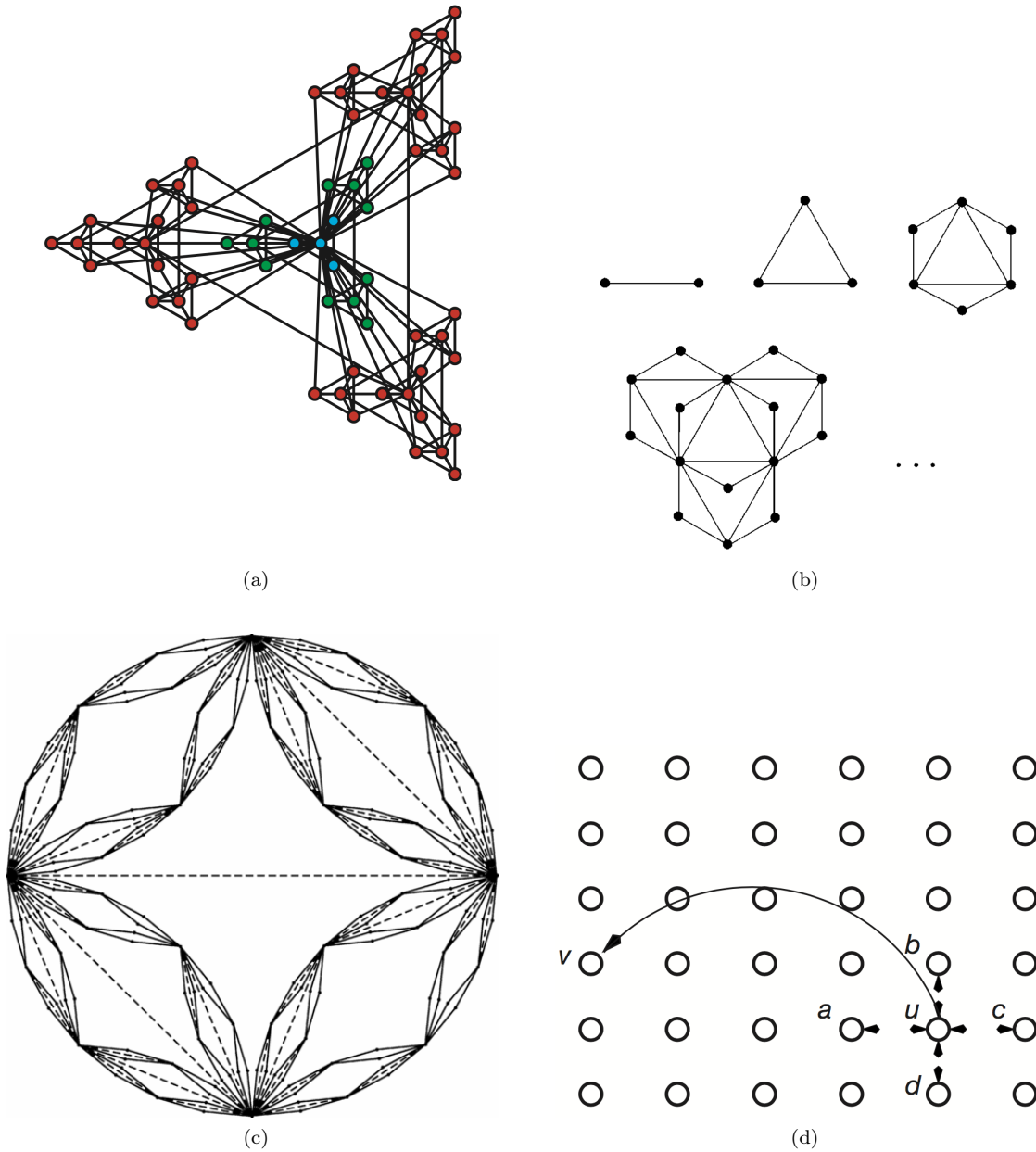
Figure 1.1: (a) The hierarchical network has a scale-free topology with embedded modularity [115]. (b) Scheme of the growth of the scale-free pseudo fractal graph [53]. The growth starts from a single edge connecting two vertices. At each time step, every edge generates an additional vertex, which is attached to both end vertices of the edge. (c) An example of the hierarchical lattice after $g = 4$ steps in the construction, for long-range edge probability $p = 0.6$ [70]. (d) Small world network embedded in $2-$d lattice, with short-range connections to all nodes within k lattice steps and long-range connections generated with a probability $p = l^{-\alpha}$ [78].

realization of pseudo fractals is shown in Fig.(1.1.b). The scale-free pseudo fractal graph has a cumulative degree distribution with exponent $\gamma = 1 + \ln 3/\ln 2$. It has a one-on-one correspondence between C_x and node degree k_x as $C_x = 2/k_x$. The average of shortest path lengths in pseudo fractals is estimated as $l \sim \ln N/\ln \langle k \rangle$. Hierarchical lattices, as another example shown in Fig.(1.1.c), can be tuned to have random long-range edges that are wired with a probability p [71]. The cluster coefficient increases linearly with p, and the average path length scales as $l \sim N^{1/2}$ for $p = 0$, $l \sim \ln N$ for $p = 1$. Although the degree distribution is discontinuous, the cumulative distribution has an exponent -2 for large k. Another deterministic network is called Apollonian Networks from granular packings [10]. This network arises from the space-filling packing of spheres according to the ancient Greek mathematician Apollonius of Perga. The recursive generation contributes a cumulative degree distribution with $\gamma = 1 + \ln 3/\ln 2$ and high clustering with $C = 0.828$. The small-world effect is verified through an average path length $l \sim (\ln N)^{\alpha}, \alpha \approx 3/4$.

Another important class of deterministic hierarchical networks are real self-similar fractals. Fractals are spatial networks that are embedded in the low-dimensional real space, i.e. networks whose nodes occupy a precise position in two or three-dimensional Euclidean space [24]. Typical real spatial networks include neural network, communication networks [104], electric power grids [7], transportation systems [81]. These networks have strong geographical and node-degree constraints due to the real physical connections. Small-world features can be combined into low dimensional Euclidean spaces. Watts-Strogatz (WS) networks are embedded on the $1 - d$ loop with long range edges rewired with probability p [28, 135]. Another model incorporates long range edges with $p \sim l^{-\alpha}$, for example on a square lattice in Fig.(1.1.d) [78]. An application of fractal topology is to model the hierarchical modularity in information processing networks such as brains that embed topologically complex systems in a relatively low-dimensional physical space [88, 19]. Fractals that possess self-similar structures provides a broad spectrum of graphs that capture features ranging from high clustering to low clustering, from the small-world to the large-world property. They are a family of graphs that exhibit self-similar structures in every scale, which are constructed in a recursive, hierarchal manner that lends themselves to exact renormalization. This thesis explores diverse fractal networks to understand the effects of hierarchical structures on dynamical processes.

Small-world properties added to trivial fractals or regular lattices lead to an entire new set of phenomena. An unusual phase, called inverted Berezinskii-Kosterlitz-Thouless singularity, is found between the low-temperature and high-temperature phase in ferromagnetic Ising model on hierarchical

lattices where long-range edges are randomly linked with $p \geq 0.494$ [71]. In this case, hierarchical lattices are highly clustered and small-world. In another context, by adding small-world features to regular lattices, percolation with explosive cluster growth emerges at the critical point [35]. A "patchy" percolation has been found in a small-world Hanoi network, where a spanning cluster is obtained with a finite probability unlike the 0-1 transition found in regular lattices [29].

Beyond small-world networks, hierarchical organization can form networks with a finite fractal dimension d_f [52, 18]. A broaden critical region is reported on brain network models that have a finite fractal dimension d_f [92]. On hierarchical structures that model modular architecture of neurons, a number of metastable states exist in the spin system where the coupling decays with the distance [3]. This can be used to study the modular architecture and parallel processing in neuron networks [4]. In this thesis, we focus on two classes of fractals, Hanoi networks and hierarchical lattices, which contain types of hierarchical structures from regular to non-regular, small-world to non small-world, low clustering to high clustering, and finite fractal dimension to infinite fractal dimension.

This paper is organized as follow. In Chapter 2, we introduce hierarchical networks studied in this thesis, and describe basics of Renormalization Group (RG) techniques that are used to derive geometric and spectral properties of hierarchical networks. The ultimate goal of the study on the network structure is to understand and explain the workings of systems built on those networks. We would like to understand how the network hierarchical structure affects the quantum diffusion process and the epidemic process, and explore the analytic treatment for these processes with RG techniques. Specifically, we investigate the continuous time quantum walk in Chapter 3, and study the asymptotic behavior to reveal the dominant factor that decides the long time dynamics. As another category of quantum walks, the discrete time quantum walk is explored in Chapter 4 where RG is helpful to yield the scaling collapse of the spreading behavior. We also investigate the phenomenon of a Griffiths phase that is proposed to be a working mechanism on brain architecture, using the epidemic model SIS in Chapter 5. In the conclusion, Chapter 6, we summarize this thesis, and discuss open questions in the subjects we studied.

Chapter 2

Hierarchical Networks

In this Chapter, we introduce two families of self-similar hierarchical structures, the first of which are Hanoi networks. Hanoi networks were introduced first to resemble the small-world properties in spatial networks in which small-world edges are deterministic unlike the inherently disordered long-range connections as the original Watts-Strogatz network [28, 135]. The degree distribution of Hanoi networks is neither a power law as in scale-free networks, nor shaped as WS networks, which is similar to random networks that have a pronounced peak at $\langle k \rangle$ and decays exponentially for large k. The degree distribution is either a delta function centered at a degree K, or an exponential function of the hierarchy. As we introduced the general structural characteristics in Chap.1, these networks have simple and deterministic geometric structures but exhibit novel dynamics in percolation and the Ising Ferromagnet [29, 26]. In this chapter, we provide a detailed description to these fractals.

The second class of networks are hierarchical lattices. Hierarchical lattices are generated from Migdal-Kadanoff Renormalization Group (MKRG) theory [90, 74, 22]. Migdal-Kadanoff RG is useful for physical systems in low dimensions, and is widely studied in statistical physics [59, 108, 105]. In this section, we describe instances of graphs that have exactly identical fractal dimension d_f and spectral dimension d_s that can take an arbitrary real value. The spectral dimension d_s is the scaling of the smallest nonzero eigenvalue of the network Laplacian with system size N. The degree distribution of hierarchical lattices is an exponential function of the hierarchy that has a a power law cumulative distribution at large degree k. An instance of hierarchical lattices have been studied for the ferromagnetic Ising model in [71], on which the cumulative degree distribution is a pow law with exponent -2.

2.1 Structural Properties

In this section, we formulate mathematically the construction of Hanoi networks and hierarchical lattices. The iterative construction is the origin of self-similarity in fractals, and indicates the validity of RG to fractals.

2.1.1 Hanoi Networks

Hanoi networks are based on the one-dimensional line of N nodes, $[0, N-1]$. Thus, each node is at least connected to its nearest left and right neighbor on the line. Construction of hierarchical structure is based on a mathematical parameterization, which labels each node $x > 0$ using a pair of integers (i, j), $i \geqslant 1$ and $1 \leqslant j \leqslant 2^{g-i}$ such that

$$x \quad = \quad 2^{i-1}\left(2j - 1\right), \tag{2.1}$$

where i represents the level in the hierarchy, and g is the total number of levels, whereas j labels nodes in order within the same level. Long-range edges are formed by connecting nodes of different j within the same level i. Hierarchical pattern can be intuitively seen through two planar networks, HN3 and HN5 as in Fig.(2.1). A planar graph is a graph that can be embedded in the plane in such a way that its edges intersect only at their end nodes. As an extension to HN3 and HN5, HNNP and HN6 in Fig.(2.2) are designed to be nonplanar but fully renormalizable.

We obtain the 3-regular network HN3, i.e. all nodes have a degree of 3, by connecting node 1 to 3, 5 to 7, 9 to 11, etc, for $i = 1$, 2 to 6, 10 to 14, etc, for $i = 2$, and 4 to 12, 20 to 28, etc, for $i = 3$, and so on, as shown in Fig.(2.1). With mathematical formulation, the long-range edges are linked by consecutive nodes $x = 2^{i-1}(4j - 3)$ and $y = 2^{i-1}(4j - 1)$ for $1 \leq j \leq 2^{g-i-1}$ in the same hierarchical level i. We can also build a 4-regular network HN4 by connecting to consecutive nodes in both left and right direction, i. e., 1 to 3, 3 to 5, 5 to 7, etc, for $i = 1$, 2 to 6, 6 to 10, etc, for $i = 2$, and so forth. For each node in HN3, the clustering coefficient is

$$C_x \quad = \quad \begin{cases} 0 & x = 4m, \\ 1/3 & x \neq 4m, \end{cases}$$
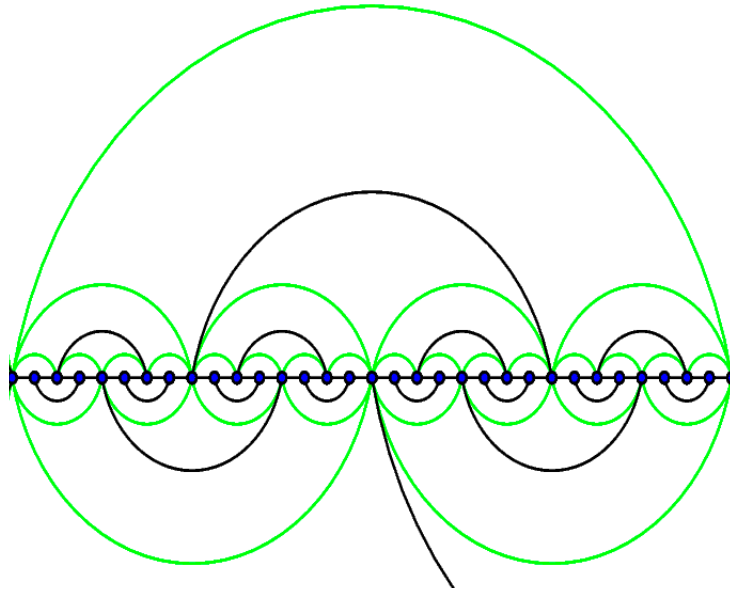
Figure 2.1: Depiction of the Hanoi networks HN3 and HN5. The 3-regular network HN3 corresponds to the solid (black) lines alone, while HN5 in addition also consists of the (green-) shaded lines. For HN5, sites on the lowest level of the hierarchy have degree 3, then degree 5, 7, etc, concerning a fraction of $1/2$, $1/4$, $1/8$, etc., of all sites, which makes for an average degree 5 in this network. Note that both networks are planar.
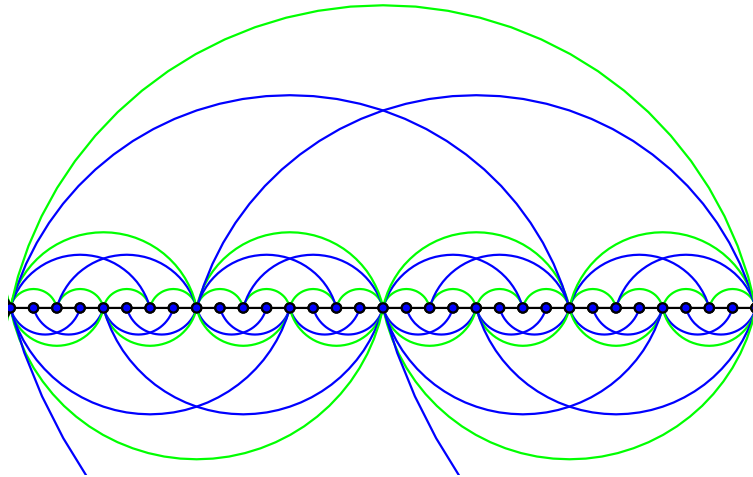
Figure 2.2: Depiction of the nonplanar Hanoi networks HNNP and HN6. Again, starting from a 1d-backbone (black lines), in HNNP a set of long-range links (blues-shades lines) is added that break planarity but maintain the hierarchical pattern set out in Eq. (2.1) that leads to a network of average degree 4. If we add again the same links that distinguished HN3 and HN5 in Fig. 2.1, we obtain HN6 with average degree 6. In all cases, the RG on these networks remains exact.
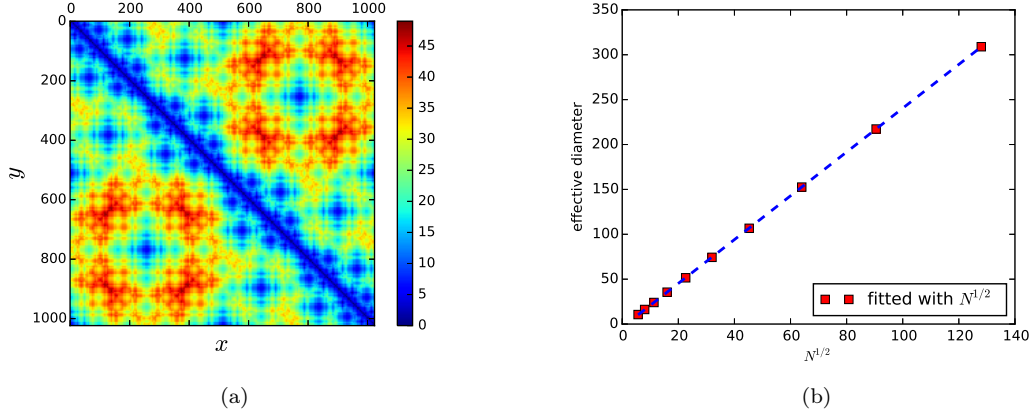
Figure 2.3: (a) the hierarchical pattern of the shortest path length from each node x to y in HN3 of generation $g = 10$. (b) the effective diameter of HN3 scales as $\sim \sqrt{N}$.

where the clustering coefficient is 0 if the label of node x is a multiple of 4, otherwise is $1/3$. The average clustering coefficient is $1/4$. The hierarchical pattern in structure can also be illustrated and quantified through shortest path lengths from each node to all the others, shown in Fig.(2.3.a). The largest of all the shortest path lengths is the diameter of network. It can be approximated with the effective diameter i.e. the minimum number of hops in which 90% of all connected pairs of nodes can reach each other. Measurement on effective diameters is fast and efficient for massive real networks [76]. For HN3, the effective diameter scales as $\sqrt{N}$, as shown in Fig.(2.3.b). It suggests that although long-range edges are added to HN3, it is a large-world network with a finite fractal dimension $d_f = 2$.

One extension of HN3 that leads to a small-world network is the planar network with an average degree of 5, hence denoted as HN5. In addition to edges in HN3, in HN5 we link all even nodes to both of their consecutive even nodes recursively shown in Fig.(2.1). As a result, the network remains planar but now nodes have a level-dependent degree in the hierarchy. To obtain the average degree, we observe that $1/2$ of all nodes have degree 3, $1/4$ have degree 5, $1/8$ have degree 7, and so on, leading to an exponentially decreasing degree distribution of $P\left(k = 2i + 1\right) \propto 2^{-i}$. At large i, the cumulative probability $1 - 2^{-i}$, which does not fit a power law. For nodes 0 and 2^{k-1}, special consideration is required for the degree. The total number of edges in the network of size $N = 2^g$ is

$$2g \times 2 + \sum_{i=1}^{g-1} \left(2i + 1\right) 2^{g-i} \quad = \quad 5 \times 2^g - 6,$$
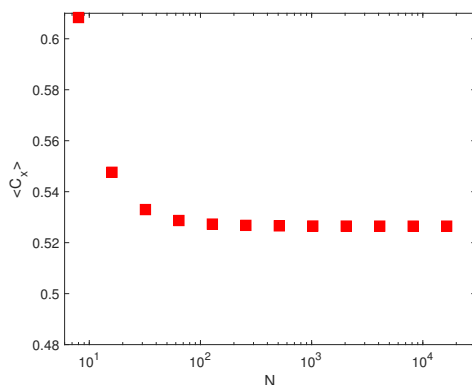
Figure 2.4: the average clustering coefficient $\langle C_n \rangle$ versus g for HN5

and therefore the average degree $\langle k \rangle = 5$. The clustering coefficient for each node in each hierarchy is

$$
C_x \quad = \quad
\begin{cases}
2/3 & i = 1 \\
1/2 & i = 2 \\
1/3 & i = 3 \\
\vdots & \vdots \\
1/(g-2) & i = g-2
\end{cases}
\quad ,
$$

Special case takes place for node 0 and 2^{g-1}, i.e. $i = g$, for which $C_0 = C_{2^{g-1}} = 1/(g-1)$. For nodes in hierarchy $i = g-1$, C_x is $\frac{3}{5}, \frac{8}{21}, \frac{5}{18}, \frac{12}{55}, \frac{7}{39}, \frac{16}{105}, \frac{9}{68} \dots$ for $g = 3, 4, 5, 6, 7, 8, 9 \dots$. We find that the cluster coefficient in HN5 is level dependent, and the average is $\langle C \rangle \approx 0.527$, shown in Fig.(2.4). Shortest path lengths from each node to all the others also have a hierarchical pattern, shown in Fig.(2.5.a). The effective diameter in HN5 scales as $\ln N$, shown in Fig.(2.5.b).

2.1.2   Hierarchical Lattices

Hierarchical lattices arise from the theory of MKRG, which is a bond-moving scheme that approximates d-dimensional lattices. A single edge in the generation μ is replaced with a new subgraph, thus forming the graph of the subsequent $\mu + 1$ generation. Hierarchical lattices are easy to be tuned to obtain a wide spectrum of structural properties as needed, one instance of which is shown in Fig.(1.1.c) where additional random long-range edges are wired to obtain a small-world networks with high clustering. We here briefly introduce the bond-moving scheme to generate basic subgraphs that are used for
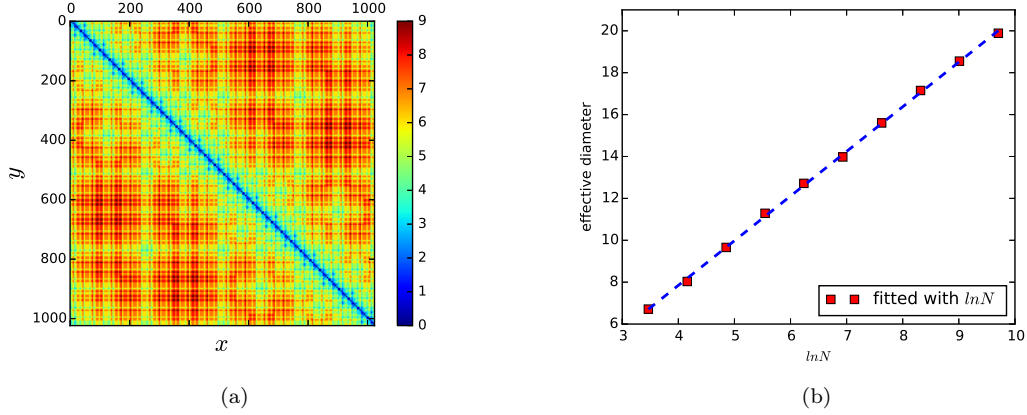
Figure 2.5: (a) the hierarchical pattern of shortest path length from each node x to y in HN5 of generation $g = 10$. (b) the effective diameter of HN5 scales as $\ln N$.

iterative constructions. In statistical physics, this structure of the subgraph arises from the bond-moving scheme in d dimensions [90, 74], as depicted in Fig.(2.6): In a hyper-cubic lattice of unit bond length, at first all $l - 1$ intervening hyper-planes of bonds, transverse to a chosen direction, are projected into every l^{th} hyper-plane, followed by the same step for $l - 1$ hyper-planes being projected onto the lth plane in the next direction, and so on. In the end, one obtains a renormalized hyper-cubic lattice (of bond length l) in generation $\mu + 1$ with a renormalized bond of generation $\mu + 1$ consisting of a sub-graph of

$$b = l^{d-1} \tag{2.2}$$

parallel branches, each consisting of a series of l bonds of generation μ. In turn, we can rewrite Eq.(2.2) as

$$d = 1 + \frac{\ln(b)}{\ln(l)}, \tag{2.3}$$

anticipating analytic continuation in l and b to obtain results for arbitrary, real dimensions d. In the following, we consider a general series of Migdal-Kadanoff networks by varying b while fixing $l = 2$.

For any integer value of b, for graph of the $g-$th generation, there are a total of $N_g = 2 + \frac{b(2^g b^g - 1)}{2b - 1}$ nodes. Initially, there are two end nodes in the $0-$th hierarchy. After one-step of recursion, b more nodes are generated. Another step of recursion generates $b(2b)$ more nodes. Hence, $i-$th step of recursion generates $b(2b)^{i-1}$ more nodes. The degree for two end nodes in the $0-$th hierarchy is therefore b^g. For nodes in ith hierarchy, the node degree is $k_i = 2\, b^{g-i}$. The average degree satisfies
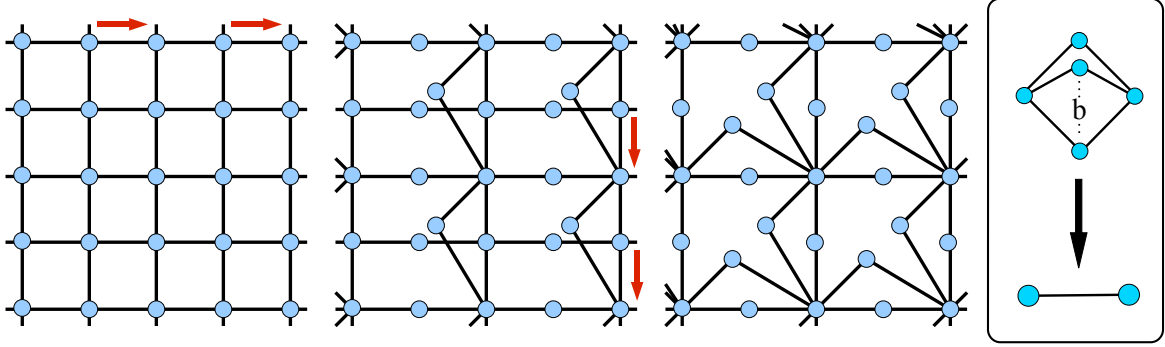
Figure 2.6: Bond-moving scheme in the Migdal–Kadanoff renormalization group, here for a square lattice ($d = 2$) with $l = 2$, i. e. $b = 2$ in Eq. (2.2). Starting from the lattice with unit bonds (a), bonds in intervening hyper-planes are projected onto every l^{th} plane in one direction while bonds connect to the lth plane only at every l^{th} vertex (b), which is then repeated in subsequent directions (c), to re-obtain a similar hyper-cubic lattice, now of bond-length l (a). The renormalized bonds in this case consist of $b = l^{d-1} = 2$ branches, each of a series of $l = 2$ bonds; the general RG-step for $l = 2$ and arbitrary branches b is depicted in (d).

$$N_g \langle k \rangle = 2 \times b^g + \sum_{i=1}^{g} \left[b \left(2b \right)^{i-1} \right] \left[2 \, b^{g-i} \right],$$

which results in a average degree $\langle k \rangle$ of value $[3, 3.9]$ for $b \in [2, 20]$ with $g = 50$. The cumulative distribution at large k converges to a power law with exponent $- \ln \left(2b \right) / \ln b$, which is consistent with the exponent -2 for $b = 2$ reported in [71]. For a scale-free network, $P_{cum} \left(k \right) \sim k^{1-\gamma}$ with $N \to \infty$. In the hierarchical lattices with $b = 2$, $\gamma = 3$ is comparable to the real scale free networks [6]. The clustering coefficient for each node is $C_x = 0$. For the hierarchical lattice with $b = 2$, the average path length scales as $\sqrt{N}$, which shows the hierarchical lattice is a large world network [71]. To obtain the small world property, long range edges are added with a probability p, which provide a linear increasing average of clustering coefficients with p, and decreasing average of shortest path lengths towards $\ln N$ [71].

2.2   Spectral properties of network Laplacians

In addition to structural characteristics that can be studied directly in Sec.2.1, the spectrum of the network Laplacian matrix also provides information on geometry, which is used in various practical applications. For example, synchronizability of a network is indicated by the ratio of the largest and

smallest nonzero eigenvalue[15]. Permeability and well-connectedness of networks can be defined in terms of the spectral gap [86]. The spectrum is also applied to analyze the algorithmic efficiency in continuous-time quantum search algorithms [42, 84], graph partitioning [110, 69] and image processing [106]. There has been a strong motivation to study the Laplacian spectrum on fractals[51, 111, 61, 112, 120, 123]. In this section, we show the application RG to spectrum of the Laplacian, from which we obtain the analytic expression for the enumeration of spanning trees in a network and its synchronizability.

The adjacency matrix of an unweighted network is defined as A_{xy}, which is 1 if node x and y are connected, and otherwise is 0. The Laplacian matrix is given by

$$\mathbf{L}_{xy} \quad = \quad k_x \delta_{xy} - A_{xy}. \tag{2.4}$$

For undirected networks concerned in this thesis, $\mathbf{L}$ is symmetric. All row or column sums vanish in $\mathbf{L}$, $\sum_x \mathbf{L}_{xy} = \sum_y \mathbf{L}_{xy} = 0$. The fundamental property characterizing the Laplacian matrix is its spectrum of eigenvalues, i.e. the solutions λ_i of the secular equation

$$\det\left[\mathbf{L} - \lambda\mathbf{1}\right] \quad = \quad 0. \tag{2.5}$$

The Laplacian matrix is positive semidefinite, i.e. $\lambda_i \geq 0$ and $\lambda_1 = 0$. The smallest nonzero λ_2 defines the spectral gap. This spectrum is highly nontrivial for hierarchical lattices and Hanoi networks, which can nevertheless be studied by the RG approach.

2.2.1 Spanning Trees on a Network

We first consider the enumeration of spanning trees in a graph based on which we introduce the idea of RG. The number of spanning tress of a graph, also referred to as "graph complexity" [85], is obtained by taking $\epsilon \to 0$,

$$\#_{\text{ST}} = -\lim_{\epsilon \to 0} \frac{\det\left[\mathbf{L} + \epsilon\mathbf{1}\right]}{\epsilon N}, \tag{2.6}$$

which is one of the oldest results in algebraic graph theory, due to Kirchhoff [23]. Spanning trees describe the size of the attractor state in the self-organized critical sandpile model [49], characterize the optimal paths between any two nodes in a network [138], and are also related to optimal synchronizability of a network [97]. The number of spanning trees is of fundamental interest in mathematics

and physics. For example, it is related to the partition function of q−state Potts model in the limit $q \to 0$ [50, 137]. Thus, studies on the asymptotic growth of spanning trees are well motivated not only for regular lattices [121], but also on self-similar structures [40, 124, 126]. If the number of spanning trees $\#_{ST}$ exponentially increases with N, it can be characterized by the tree entropy, which is the entropy-density of spanning trees [85, 40, 125],

$$s \;=\; \lim_{N\to\infty} \frac{\ln\left(\#_{\mathrm{ST}}\right)}{N}. \tag{2.7}$$

The number of spanning trees on fractals can be easily derived from the evaluation of the Laplacian via the RG procedure. We will show later that geometry of networks affects its asymptotic growth.

The determinant of $\mathbf{L} + \epsilon\mathbf{1}$ for fractals can be evaluated asymptotically in a recursive decimation scheme. We have already described the procedure in [32, 34], and present great details in Sec.7.1. In general, we employ the well-known formal identity [113],

$$\frac{1}{\sqrt{\det \mathbf{L}}} \;=\; \int \cdots \int_{-\infty}^{\infty} \left(\prod_{i=1}^{N} \frac{dx_i}{\sqrt{\pi}}\right) \exp\left\{-\sum_{n=1}^{N}\sum_{m=1}^{N} x_n \mathbf{L}_{n,m} x_m\right\}. \tag{2.8}$$

For RG, we employ a hierarchical scheme by which at each step μ a fraction $1/f$ of all remaining variables get integrated out while leaving the integral in Eq.(2.8) invariant. For Hanoi networks as an example, we integrate out every odd-indexed variable in a network at step μ. We separate $\prod_{i=1}^{N} dx_i = \prod_{i=1}^{N/2} dx_{2i} \prod_{j=1}^{N/2} dx_{2j+1}$, integrate to receive

$$\frac{1}{\sqrt{\det \mathbf{L}}} = C' \int \cdots \int_{-\infty}^{\infty} \left(\prod_{i=1}^{\frac{N}{2}} \frac{dx_{2i}}{\sqrt{\pi}}\right) \exp\left\{-\sum_{n=1}^{\frac{N}{2}}\sum_{m=1}^{\frac{N}{2}} x_{2n} \mathbf{L}'_{n,m} x_{2m}\right\}, \tag{2.9}$$

where the reduced Laplacian $\mathbf{L}'$ is now a $\frac{N}{2} \times \frac{N}{2}$ matrix that is formally identical with with $\mathbf{L}$ and C' is an overall scale-factor. If $\mathbf{L} = \mathbf{L}\left(q, p, \ldots\right)$ depends on some parameters, then $\mathbf{L}' = \mathbf{L}'\left(q', p', \ldots\right)$ depends on those parameters in the same functional form, thereby revealing the RG-recursion relations, $q' = q'\left(q, p, \ldots\right)$, $p' = p'\left(q, p, \ldots\right)$, etc, and $C' = C'\left(q, p, \ldots\right)$, that contains all the information of the original Laplacian. After a sufficient number of such RG-steps, a reduced Laplacian of merely a few variables remains that can be solved by elementary means.

We show here how to use recursions of parameters $(q, p, l \ldots)$ to calculate the Laplacian determinant

on HN3 and HN5. The recursions are

$$
\begin{aligned}
q_{\mu+1} &= q_\mu + 2l_\mu - 2\frac{p_\mu^2}{q_\mu - 1}, \\
p_{\mu+1} &= l_\mu + \frac{p_\mu^2}{q_\mu - 1}, \\
l_{\mu+1} &= l_0 + \frac{p_\mu^2}{q_\mu^2 - 1},
\end{aligned}
\tag{2.10}
$$

and

$$
C_g^{(\mu)} = \prod_{i=0}^{\mu-1} [q_i^2 - 1]^{-2^{k-3-i}},
\tag{2.11}
$$

such that the determinant of the Laplacian of HN3 after $g - 2$ RG-steps becomes:

$$
\begin{aligned}
\det\left[\mathbf{L}_g^{(3)} + \epsilon\mathbf{1}\right] &= \frac{1}{\left[C_g^{(g-2)}\right]^2} \det\begin{bmatrix} q_{g-2} + 2l_{g-2} & -p_{g-2} & l_0 - 2l_{g-2} - 1 & -p_{g-2} \\ -p_{g-2} & q_{g-2} & -p_{g-2} & -1 \\ l_0 - 2l_{g-2} - 1 & -p_{g-2} & q_{g-2} + 2l_{g-2} & -p_{g-2} \\ -p_{g-2} & -1 & -p_{g-2} & q_{g-2} \end{bmatrix} \\
&= \left[C_g^{(g-2)}\right]^{-2} (q_{g-2} + 1)(q_{g-2} + 4l_{g-2} + 1)\left[(q_{g-2} - 1)^2 - 4p_{g-2}^2\right].
\end{aligned}
\tag{2.12}
$$

For the Laplacian determinant of HN5, special consideration is required for the on-site factor of node 0 and 2^{g-1} due to their initial degree. Hence the determinant is evaluated by introducing one more parameter r_{g-2} that is exactly determined by all of the others,

$$
\begin{aligned}
\det\left[\mathbf{L}_g^{(5)} + \epsilon\mathbf{1}\right] &= \frac{1}{\left[C_g^{(g-2)}\right]^2} \det\begin{bmatrix} r_{g-2} & -p_{g-2} & l_0 - 2l_{g-2} - 1 & -p_{g-2} \\ -p_{g-2} & q_{g-2} & -p_{g-2} & -1 \\ l_0 - 2l_{g-2} - 1 & -p_{g-2} & r_{g-2} & -p_{g-2} \\ -p_{g-2} & -1 & -p_{g-2} & q_{g-2} \end{bmatrix} \\
&= \left[C_g^{(g-2)}\right]^{-2} (q_{g-2} + 1)(2l_{g-2} + r_{g-2})\left[(1 - q_{g-2})(2l_{g-2} - r_{g-2}) - 4p_{g-2}^2\right].
\end{aligned}
\tag{2.13}
$$

The initial conditions on the RG-recursions that distinguish between HN3 and HN5 are:

$$
\begin{aligned}
C_k^{(0)} &= 1, \\
q_0 &= 3 + \epsilon, \\
p_0 &= 1, \\
l_0 &= \begin{cases} 0, & \text{for HN3} \\ 1, & \text{for HN5} \end{cases}.
\end{aligned}
\tag{2.14}
$$

As shown in [32, 34], the parameters $\{q_{k-2}, p_{k-2}, l_{k-2}\}$ in Eq.(2.10) in HN3 approach fixed points as

$$
\begin{aligned}
q_\mu &\sim 1 + \left(\frac{2}{\phi}\right)^{-\mu} \left(Q_0 + \epsilon \left(\frac{4}{\phi}\right)^{\mu} Q_1 + \epsilon^2 \left(\frac{4}{\phi}\right)^{2\mu} Q_2 \ldots \right), \\
p_\mu &\sim \left(\frac{2}{\phi}\right)^{-\mu} \left(P_0 + \epsilon \left(\frac{4}{\phi}\right)^{\mu} P_1 + \epsilon^2 \left(\frac{4}{\phi}\right)^{2\mu} P_2 \ldots \right), \\
l_\mu &\sim \left(\frac{2}{\phi}\right)^{-\mu} \left(L_0 + \epsilon \left(\frac{4}{\phi}\right)^{\mu} L_1 + \epsilon^2 \left(\frac{4}{\phi}\right)^{2\mu} L_2 \ldots \right),
\end{aligned}
\tag{2.15}
$$

where $\phi = \left(\sqrt{5} + 1\right)/2$. In turn, the set of parameters in Eq.(2.10) for HN5 approach the fixed points as

$$
\begin{aligned}
q_\mu &\sim \frac{5 + \sqrt{41}}{2} + \left(\epsilon 2^{\mu} Q_1 + \epsilon^2 2^{2\mu} Q_2 \ldots \right), \\
p_\mu &\sim \frac{3 + \sqrt{41}}{4} + \left(\epsilon 2^{\mu} P_1 + \epsilon^2 2^{2\mu} P_2 \ldots \right), \\
l_\mu &\sim \frac{3 + \sqrt{41}}{8} + \left(\epsilon 2^{\mu} L_1 + \epsilon^2 2^{2\mu} L_2 \right).
\end{aligned}
\tag{2.16}
$$

The pre-factor becomes $\left[C_g^{(g-2)} \right]^{-2} \sim \alpha^N$. Parameter α is a constant that can be determined to any accuracy from Eq. (2.11), which is estimated as $\alpha \approx 2.018999052$ for HN3 at $k = 30$. Inserted into Eq.(2.12), we obtain

$$
\det \left[\mathbf{L_g^{(3)}} + \epsilon \mathbf{1} \right] \quad \sim \quad \alpha^N \phi^{3k} / N^2 \epsilon,
\tag{2.17}
$$

Table 2.1: Entropy-densities from Eq. (2.7) for spanning trees on Hanoi networks.

Hanoi networks	$s = \frac{1}{N} \ln\left(\#_{ST}\right)$
HN3	$0.7026018\ldots$
HN5	$1.2573823\ldots$
HNNP	$1.0814688\ldots$
HN6	$1.4104309\ldots$

and the number of spanning trees on HN3 is:

$$\#_{\text{ST}} \sim \alpha^N \left(\phi/2\right)^{3k}, \tag{2.18}$$

whereas for HN5, HNNP, and HN6, the determinant is calculated as

$$\det\left[\mathbf{L_g} + \epsilon\mathbf{1}\right] \quad \sim \quad \alpha^N N\epsilon, \tag{2.19}$$

and the number of spanning trees is:

$$\#_{\text{ST}} \sim \alpha^N, \tag{2.20}$$

We obtain the number of spanning trees characterized by the tree entropy on Hanoi networks, shown in Tab.(2.1).

For hierarchical lattices after g steps of decimation, the pre-factor $\left(C_g\right)^{-2}$ in Eq.(7.37) scales as α^N. We numerically determine the value of α after $g = 50$ is respectively $\alpha = 2.000000000\ldots$, $2.168943542\ldots$, $2.208179027\ldots$, and $2.214346358\ldots$ for $b \in [2,5]$. The determinant is derived as Eq.(7.36) in Sec.7.1.3,

$$\det\left[\mathbf{L_g} + \epsilon\mathbf{1}\right] \quad \sim \quad C_g^{-2} b^{2g} \left(q_g^2/4 - p_g^2\right), \tag{2.21}$$

$$\sim \quad \alpha^N \times b^{2g}\epsilon = \alpha^N \times \left(\frac{b}{2}\right)^g N\epsilon \tag{2.22}$$

and thus the number of spanning trees is

$$\#_{\text{ST}} \sim \alpha^N \times \left(\frac{b}{2}\right)^g. \tag{2.23}$$

We estimate the tree entropy on hierarchical lattices, shown in Tab.(2.2)

Table 2.2: Entropy-densities from Eq. (2.7) for spanning trees on Hanoi networks.

Hierarchical lattices	$s = \frac{1}{N} \ln \left(\#_{ST} \right)$
$b = 2$	$0.6931471 \ldots$
$b = 3$	$0.7742402 \ldots$
$b = 4$	$0.7921682 \ldots$
$b = 5$	$0.7949572 \ldots$

2.2.2 Special Zeta Function and Synchronization

A further application of the Laplacian spectrum is the spectral zeta function, which is related to the evaluation of network synchronizability and the efficiency of continuous time quantum search algorithm. We will discuss the quantum search in Chap.3, and here focus on the network synchronizability. Asymptotic evaluation of the ability to synchronize identical dynamical systems in a network depends on the ratio of largest λ_N to smallest nonzero λ_2 eigenvalue of the Laplacian [15]. The scaling of λ_2 yields from that of the spectral zeta function. λ_N can be estimated with a power method [80]. RG makes the numerical estimation stable and accurate. Details is in Sec.7.2.

The spectral zeta function of the Laplacian is defined as [131, 5, 54],

$$I_j = \frac{1}{N} \sum_{i=2}^{N} \left(\frac{1}{\lambda_i} \right)^j . \tag{2.24}$$

In the evaluation of partition functions in field theory, the I_j often feature in the continuation to non-integer moments, in particular, the limit $j \to 0$ [113]. In almost all cases, with the exception of regular lattices where Fourier transforms can be applied, and some fractals [111], it is impossible to find each eigenvalue in the sum of Eq. (2.24). However, the sum defined in Eq. (2.24) for I_j can be expressed as the j-th derivative of the determinant $\mathbf{L} + \epsilon \mathbf{1}$ in the limit $\epsilon \to 0$:

$$
\begin{aligned}
I_j &= \frac{1}{N} \frac{(-1)^j}{(j-1)!} \left(\frac{\partial}{\partial \epsilon} \right)^j \left. \sum_{i=2}^{N} \ln \left(\lambda_i + \epsilon \right) \right|_{\epsilon \to 0} , \\
&= \frac{1}{N} \frac{(-1)^j}{(j-1)!} \left(\frac{\partial}{\partial \epsilon} \right)^j \left. \ln \left[\frac{1}{\epsilon} \prod_{i=1}^{N} \left(\lambda_i + \epsilon \right) \right] \right|_{\epsilon \to 0} , \\
&= \frac{1}{N} \frac{(-1)^j}{(j-1)!} \left(\frac{\partial}{\partial \epsilon} \right)^j \left. \ln \left[\frac{1}{\epsilon} \det \left(\mathbf{L} + \epsilon \mathbf{1} \right) \right] \right|_{\epsilon \to 0} ,
\end{aligned}
\tag{2.25}
$$

where we have used the fact that $\lambda_1 = 0$. We can use the RG to derive the scaling of I_j without calculating each individual Laplacian eigenvalue λ_i [33, 34]. Results of I_j for HN3 are,

$$I_j \quad \sim \quad \left[\left(\frac{2}{\phi} \right)^{\log_2 N} \right]^j ,$$
$$\sim \quad \left[N^{1 - \log_2 \phi} \right]^j , \tag{2.26}$$

and for HN5 are

$$I_j \quad \sim \quad \begin{cases} \ln N & j = 1, \\ \\ N^{2j/2 - 1} & j \geq 2. \end{cases} \tag{2.27}$$

The zeta-functions for the Laplacian determinants with varying b for hierarchical lattices are eventually evaluated as

$$I_j \quad \sim \quad \begin{cases} N^{2j/(1 + \frac{\ln b}{\ln 2}) - 1} & 2j > (1 + \frac{\ln b}{\ln 2}) \\ \\ \ln N & 2j = (1 + \frac{\ln b}{\ln 2}) \\ \\ const & 2j < (1 + \frac{\ln b}{\ln 2}) \end{cases} \tag{2.28}$$

The spectral dimension d_s refers to the scaling of λ_2 with system size N as,

$$\lambda_i \sim \left(\frac{i}{N} \right)^{\frac{2}{d_s}} , \tag{2.29}$$

which generally on fractals holds for a range of eigenvalues $\lambda_1 < \lambda_i \leq \lambda_{i_c}$ for all $2 \leq i \leq i_c$ up to i_c. We show two examples in Fig.(2.7). Under these assumptions, it is easy to evaluate the spectral zeta-function in Eq. (2.24) in the continuous limit, $\frac{i}{N} \to \theta$ with $d\theta = \frac{1}{N}$, such that

$$\frac{1}{N} \sum_{i=2}^{N} \left(\frac{1}{\lambda_i} \right)^j \quad \sim \quad \int_{\frac{1}{N}}^{\theta_c} d\theta \, \theta^{-\frac{2j}{d_s}} + const,$$
$$\sim \quad N^{\frac{2j}{d_s} - 1} + const, \tag{2.30}$$

which holds if $2j > d_s$, and we assume the scaling is dominated by small eigenvalues with an asymptotical expression in Eq. (2.29). The zeta-functions are again identified as
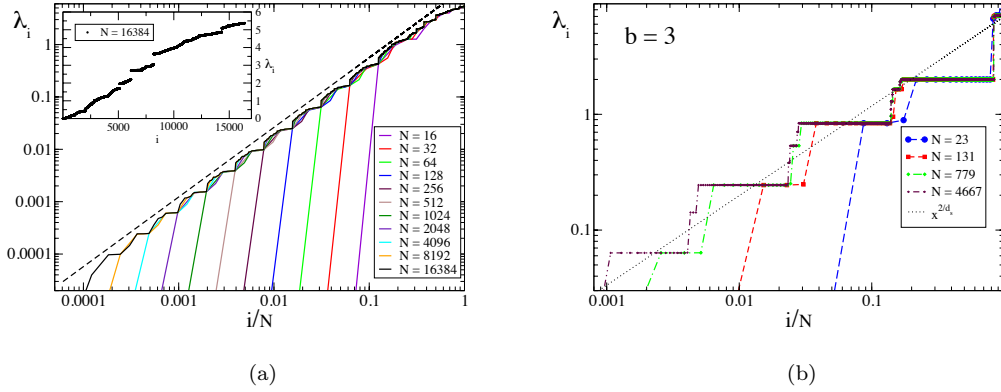
Figure 2.7: Plot of the Laplacian eigenvalues λ_i ordered by rank i as a function of $\frac{i}{N}$ for various system sizes N of the Hanoi network HN3 (left) and MKRG at $b = 3$ (right). The dashed line follows a power law with exponent $2/d_s = d_w/d_f \approx 1.31$ [27] for HN3, and for MKRG with $d_s = 1 + \log_2 3$. The inset for HN3 shows the same data for only $N = 2^{16}$ on a linear scale, showing that the scaling concerns only the part of the spectrum where $\frac{i}{N}$ is small.

$$I_j \quad \sim \quad N^{2j/d_s - 1}, \qquad 2j > d_s. \tag{2.31}$$

Hence, we evaluate d_s in Hanoi networks and hierarchical lattices as,

$$d_s = \begin{cases} 2/\left(2 - \log_2 \phi\right) & HN3 \\ 2 & HN5 \\ 1 + \frac{\ln b}{\ln 2} & MKRG \end{cases} .$$

which is confirmed in [34, 5].

The calculation on λ_2 and λ_N is sufficient for a vague estimation of the synchronizability. The linear stability of the synchronous state is related to an algebraic condition of the Laplacian matrix [15]. The generic requirement for the synchronous state to be linearly stable is $\sigma\lambda_i \in (\alpha_1, \alpha_2)$ for all the nonzero eigenvalues of the Laplacian matrix, where σ is the global coupling, and (α_1, α_2) is the negative region of the master stability function that depends solely on the dynamical system. For dynamical systems on network of arbitrary topology, whether the network is synchronizable is decided by the algebraic condition $\lambda_N/\lambda_2 < \alpha_2/\alpha_1$.

The RG approach that estimates the largest eigenvalue is specified in Sec.7.2. We present the
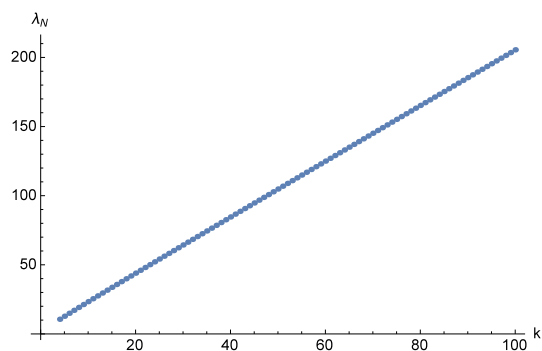
Figure 2.8: Plot of the largest eigenvalue λ_N for HN5 with system size $k\,(= \log_2 N)$, as obtained by the power-method using the recursions in Eq. (7.50) . A linear fit provides a scaling of $\lambda_N \sim$ $2.023588046\ldots k + 3.460393100\ldots$.

results here. For HN3, the largest eigenvalue is bounded by $\lambda_N \leq 6$ that is estimated as $\lambda_N = 5.37272879308215\ldots$. In HN5, the asymptotic value of λ_N for varying size $N = 2^g$ is presented in Fig.(2.8). The largest eigenvalues are shown to scale with $\lambda_N \sim 2\log_2 N$. The asymptotic value of λ_N for hierarchical lattices, which scales as $\lambda_N \sim b^g \sim N$, shown in Fig.(2.9). The eigen-ratios of HN3, HN5 and hierarchical lattices are asymptotically $N^{2-\log_2 \phi}$, $2N\log_2 N$ and $N^{(3+\log_2 b)/(1+\log_2 b)}$. This would imply that the synchronizability for these networks is ranked as HN5>HN3>HL $(b \leq 46)$. This conclusion intuitively suggests that small world edges improve the synchronizability, as seen from the comparison between Hanoi networks and hierarchical lattices.

(a) b=2

(b) b=3

(c) b=4

(d) b=5
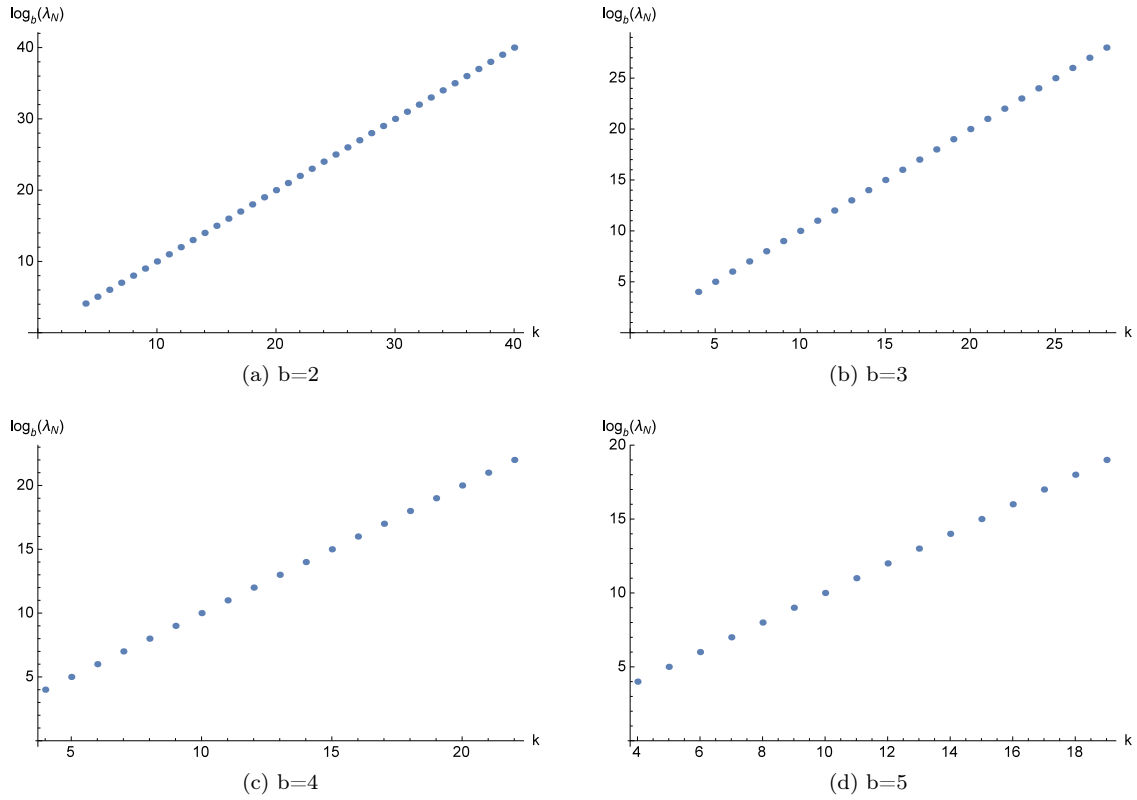
Figure 2.9: Plots of the largest eigenvalue λ_N with system size $k(\sim \log_b N)$ for MKRG with $b = 2, 3, 4, 5$. It can be fitted respectively as $\log_{b=2} \lambda_N = 0.9992544987\ldots k + 0.0213953207\ldots$, $\log_{b=3} \lambda_N = 0.9998501326\ldots k + 0.0030754291\ldots$, $\log_{b=4} \lambda_N = 0.9999427813\ldots k + 0.0009418968\ldots$, and $\log_{b=5} \lambda_N = 0.9999734834\ldots k + 0.0003826594\ldots$, showing that $\lambda_N \sim b^k \sim N$.

Chapter 3

Continuous Time Quantum Search

In this chapter, we study the relation between the Laplacian and continuous time quantum spatial search. Since Grover proposed the quantum algorithm searching an unstructured database with N items in time $\sim \sqrt{N}$, i.e. a quadratic speed-up over classical search algorithms [67], quantum search has been a framework where quantum algorithms beat classical algorithms. The spatial search problem presents a scenario where N items are stored in a $d-$dimensional physical space, and quantum computer explores this database by making local moves. As an analog of the classical random walk, the continuous time quantum walk (CTQW) provides a model for the spatial search on graphs. In an elementary version of CTQW, quantum systems are driven by the Hamiltonian following the definition in [42],

$$\mathcal{H} \;\; = \;\; \gamma\,\mathbf{L} - |w\rangle\,\langle w|\,, \tag{3.1}$$

where $\mathbf{L}$ is the Laplacian matrix, γ is the tunable parameter, and w is the target node.

Study of CTQW on various graphs starts from complete graphs [56], hypercubes [44, 57] and regular lattices. Unlike the first two, CTQW fails to provide a quadratic speedup in regular lattices with $d \leq 4$. Recently, CTQW has been explored on on Erdös-Renyi graphs with N nodes, which is optimal as long as the the wiring probability for an edge between any two nodes is $p \gtrsim \log^{3/2} N/N$ [39]. The particular interest of CTQW on fractal networks has been investigated in [2], where fractals include dual Sierpinski gaskets, T-fractals, Cayley trees, and Cartesian products between Euclidean lattices and dual Sierpinski gaskets. These fractals have different d_f and d_s, which are generally not identical. Numerical experiments in [2] suggest that two factors together determine whether a

(a)

(b)
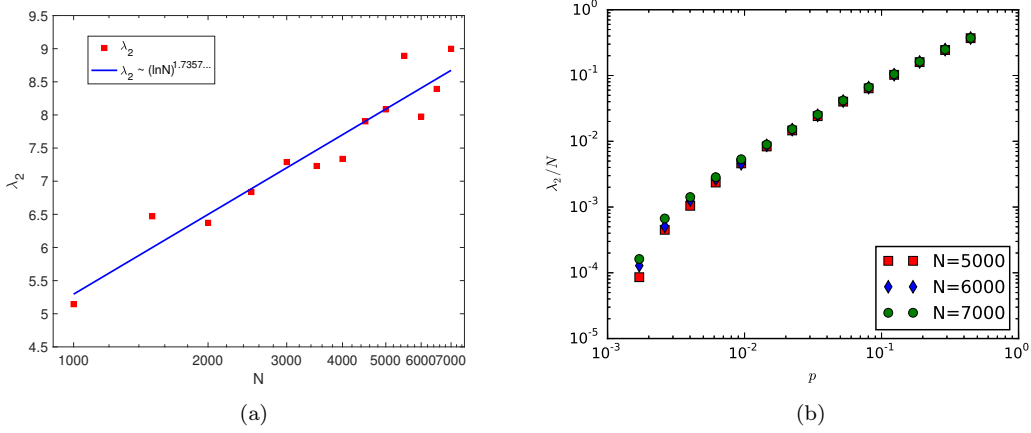
Figure 3.1: (a) λ_2 versus N for random graph with $p = \log^{3/2} N/N$. Red squares are λ_2 averaged over graph realizations for $N \in [1000, 7000]$. Blue line is fitted with $\lambda_2 \sim (\ln N)^\alpha$, $\alpha \approx 1.7357$. (b)λ_2/N versus p for $N = 5000, 6000, 7000$.

quadratic speedup can be achieved. One is that d_s should be larger than 4, and the other is that there is a sharp transition at a critical point γ_c of overlaps of the initial and the target state with the ground and first excited state of the Hamiltonian.

In [42], the critical point γ_c is related to the spectral zeta function of the Laplacian of regular lattices. As discussed in Sec.2.2.2, RG enables us to calculate the spectral zeta function for hierarchical structures. We study analytical expressions of efficiency of CTQW on fractals that include HN3, Sierpinski Gasket, and hierarchical lattices. Results reveal that γ_c and thus the algorithmic efficiency depend only on the spectral dimension d_s. It generalizes theoretical predictions of the algorithmic efficiency on lattices and Erdös-Renyi graphs to any geometric structures. This argument is based on the fact that for lattices, $d_s = d$, and for random graphs with $p \gtrsim \log^{3/2} N/N$, $d_s = \infty$. The spectral dimension d_s on random graphs can be numerically verified by the scaling of λ_2 with N, for example, $\lambda_2 \sim (\ln N)^\alpha$, $\alpha \approx 1.7357$ with $p = \log^{3/2} N/N$, shown in Fig.(3.1.a), and the scaling with N for varying p is shown in Fig.(3.1.b). It suggests an infinite value of d_s considering the definition of d_s, $\lambda_2 \sim N^{-2/d_s}$.

We prove d_s controls the algorithmic efficiency of CTQW with the Hamiltonian in Eq.(3.1). It indicates fractal networks embedded in low dimensional Euclidean space can achieve optimal performance. There exist variations of continuous time quantum search, which are proposed as a solution to improve the performance in low dimensional space. To give a full picture on the quantum search, we introduce a few examples here. Aronson and Zambians proposed an extended quantum search algorithm that

finds a marked entry in time of order $\sim \sqrt{N}$ for lattices with $d > 2$, and in time $\sim \sqrt{N} \log^2 N$ for $d = 2$, using reclusive search on sub-cubes [1]. Using an appropriate lattices version of a Dirac Hamiltonian with extra spin degrees of freedom, Childs and Goldstone proposed a CTQW that competes with a time of order $\sim \sqrt{N}$ for $d > 2$ and of order $\sim \sqrt{N} \log N$ for $d = 2$ [43]. The additional spin space introduces a linear dispersion relation near the Dirac point. Fouler et al [60] exploited the Dirac point of the walk Hamiltonian on a graphene lattice to find the marked entry in time $\sim \sqrt{N} \log^{3/2} N$ for $d = 2$. Childs further generalized the idea of a Dirac point by considering CTQW on crystal lattices, where the Hamiltonian is constructed without external memory by embedding these additional degrees of freedom into the lattice as additional vertices [41] .

3.1 Spectral Zeta Function in CTQW

CTQW with the Hamilton in Eq.(3.1) relates the critical point γ_c to the spectral zeta function. We explain briefly in this section how the critical point determines the algorithmic complexity, and why it is related to the spectral zeta function. First we review some basics of CTQW.

As an analog to random walks, CTQW evolves with the Schrödinger equation in a Hilbert space spanned by the N site-basis state $|x\rangle$,

$$i \frac{d\Psi_x(t)}{dt} = \sum_y \mathcal{H}_{xy} \Psi_x(t), \tag{3.2}$$

where $\Psi_x(t) = \langle x | \Psi(t) \rangle$ is the complex amplitude at node x, and $\mathcal{H}$ is the Hamiltonian defined in Eq.(3.1). We denote eigenvalues and normalized orthogonal eigenstates for $\mathcal{H}$ and $\mathbf{L}$ respectively as $\{E_i, |\psi_i\rangle\}$ for $0 \leq i \leq N - 1$ and $\{\lambda_i, |\phi_i\rangle\}$ for $1 \leq i \leq N$. The search typically evolves from an initial state that is prepared as the uniform superposition over all site-basis states [67], $|s\rangle = \frac{1}{N} \sum_x |x\rangle$. The challenge is to find the optimal value of γ at which a physical transition on the overlaps of $|s\rangle, |w\rangle$ with the first two eigenstates $|\psi_{0,1}\rangle$ of $\mathcal{H}$. The argument for the critical γ_c is explained in [42]. Regardless of graphs, $|s\rangle$ is the first eigenstate of the Laplacian. Thus as $\gamma \to \infty$, it approximates $|\psi_0\rangle$, the ground state of the Hamiltonian. As $\gamma \to 0$, the contribution from the Laplacian can be ignored, $|\psi_0\rangle$ is close to $|w\rangle$. Since $|s\rangle$ is nearly orthogonal to $|w\rangle$, degenerate perturbation theory shows that $|s\rangle$ approximates $|\psi_1\rangle$. Therefore, at some intermediate value of γ, the ground state will switch from $|w\rangle$ to $|s\rangle$, and may have substantial overlaps with both. If the first excited state also has substantial overlaps with

$|w\rangle$ and $|s\rangle$, the Hamiltonian will drive transitions between these two states. The rotation from $|s\rangle$ to $|w\rangle$ takes time of order $t \sim 1/\left(E_1 - E_0\right)$.

The complete graph gives a good example, where it is sufficient to only consider $|s\rangle$ and $|w\rangle$. At $\gamma N = 1$, $|\psi_{0,1}\rangle$ are respectively $\left(|w\rangle \pm |s\rangle\right)/\sqrt{2}$ with a energy gap of $2/\sqrt{N}$. Hamiltonian drives the transition from state $|s\rangle$ to $|w\rangle$ with a transition probability $\Pi_{s,w} = \left|\langle w \left| e^{-iHt} \right| s \rangle\right|^2 = \sin\left(t/\sqrt{N}\right)$, which is first to be in order of $O\left(1\right)$ at time $t = \frac{\pi}{2}\sqrt{N}$. Generally, the ground and first excited state are more complicate than a superposition of $|s\rangle$ and $|w\rangle$. However, the objective of CTQW remains to be finding the critical value γ_c such that the overlaps between $|s\rangle$, $|w\rangle$ and $|\psi_{0,1}\rangle$ are substantial, and the transition from $|s\rangle$ to $|w\rangle$ takes place in an optimal time.

The relation between γ_c and $\Pi_{s,w}$ with the spectral zeta function is discovered in [42, 2] by introducing a spectral function for $\mathcal{H}$ in terms of the Laplacian eigenvalues and eigenvectors,

$$F\left(E\right) \quad = \left\langle w \left| \frac{1}{\gamma\mathbf{L}-E} \right| w \right\rangle = \sum_{i=1}^{N} \frac{|\langle w|\phi_i\rangle|^2}{\gamma\lambda_i - E}, \tag{3.3}$$

which originally is derived for lattices, and extended to fractals. It satisfies the condition on the Hamiltonian eigenvalues,

$$F\left(E_i\right) = 1. \tag{3.4}$$

With $F\left(E\right)$, one can evaluate the overlap of any eigenstate of the Hamiltonian with the initial state $|s\rangle$ as

$$\left|\langle s \left| \psi_i \right.\rangle\right|^2 = \frac{1}{N\,E_i^2\,F'\left(E_i\right)}, \tag{3.5}$$

and the transition amplitude that concerns the optimization of CTQW as

$$\langle w \left| e^{i\mathcal{H}t} \right| s \rangle = -\frac{1}{\sqrt{N}} \sum_{i=1}^{N} \frac{e^{iE_i t}}{E_i F'\left(E_i\right)}. \tag{3.6}$$

The spectral function $F\left(E\right)$ is complicated generally. In particular, it depends on $|\langle w|\phi_i\rangle|^2$, which is nontrivial, and may not be $1/N$ as it is in regular lattices. Therefore, evolution of $F\left(E\right)$ can be a difficult task. However, if we make the assumption on the overlap $|\langle w|\phi_i\rangle|^2$, it turns out to simplify the evolution to a large extent. We assume that at typical sites w of some fractal networks, the overlaps

with eigenvectors of the Laplacian still satisfy

$$|\langle w|\phi_i\rangle|^2 \sim \frac{1}{N}. \tag{3.7}$$

In Hanoi networks, the number of nodes at each hierarchical level i is 2^{g-i}, and g is the number of total levels, discussed in Sec.2.1.1. In hierarchical lattices, the number of nodes at each level i is $b\,(2b)^{i-1}$, and b is the number of branches of the sub-graplcet. In the case of Hanoi networks, although in the mathematical parameterization of Eq.(2.1) nodes with $i = 1$ may appear to be in the lowest hierarchy, in the perspective of recursive construction and decimation, they belong to the highest hierarchy, i.e. generated in the last step or decimated in the first step. Therefore, we define levels from the highest to the lowest in Hanoi networks in order of $i = 1, 2, \ldots, g$. Since nodes in highest levels constitute the largest fraction, they exhibit what can be considered as the typical behavior.

The assumption in Eq.(3.7) on overlaps for target site w with all eigenvectors $|\phi_i\rangle$ of the Laplacian can be numerically verified. In Fig.(3.2), we plot the overlaps averaged separately over all w in the highest, 2nd-highest, and 3rd-highest levels for hierarchical lattices with $b = 2$ after $g = 6$ and $b = 3$ after $g = 5$. In Fig.(3.3), we plotted the averaged overlap for the highest, 2nd-highest, and 3rd-highest levels of HN3 and HN5 as a function of the eigenstate index rescaled with N, i.e. i/N. We found the overlaps collapse well for different Ns. Furthermore, $N\,|\langle w|\phi_i\rangle|^2$ is of the order of $O\,(1)$, the maximum of which increases logarithmically as the level of hierarchy. This fact suggests that CTQW differs mildly between node w in different hierarchies. For our purpose here, we conclude that nodes in the highest level are the most representative.

With this essential assumption, and using $\lambda_1 = 0$, Eq.(3.3) can be rewritten as

$$F(E) \sim -\frac{1}{N\,E} + \frac{1}{\gamma}I_1 + \frac{1}{N}\sum_{i=2}^{N}\frac{E}{\gamma\lambda_i\,(\gamma\lambda_i - E)}, \tag{3.8}$$

with the first spectral zeta function I_1. Since d_s is the key factor for I_j as shown in Eq.(2.31), d_s affects $F\,(E)$ and physical observables in CTQW explicitly. In fact, as observed in [42], CTQW becomes optimal for lattices of any dimension when there is a phase transition in the overlaps $|\langle s|\psi_0\rangle|^2$ and $|\langle s|\psi_1\rangle|^2$ at a critical point of γ. This critical point occurs for

$$\gamma \sim \gamma_c = I_1. \tag{3.9}$$
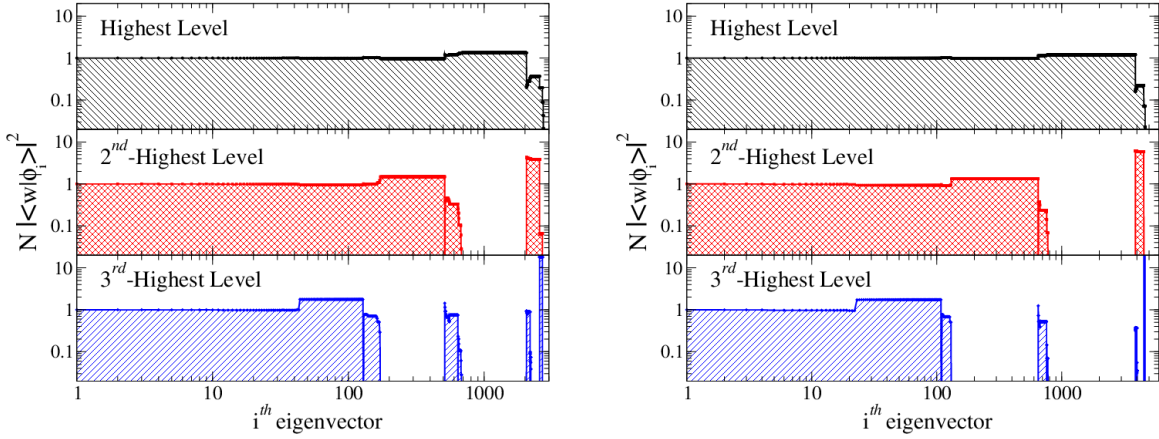
Figure 3.2:   Plot of the overlaps $|\langle w|\phi_i\rangle|^2$ in MKRG for the searched-for sites w with the Laplacian eigenvectors ϕ_i as a function of i, ordered such that respective eigenvalues satisfy $\lambda_i \leq \lambda_{i'}$ for any two indices $i \leq i'$. The MKRG used here [25] rescales length by $l = 2$ with (a) $b = 2$ and (b) $b = 3$ branches in each RG-step for an effective dimension $d = 1 + \log_l b$ of (a) $d = 2$ and (b) $d = 2.585\ldots$. The RG has been iterated for $g = 6$ generations in the hierarchy in (a), forming a lattice of $N = 2 + \frac{b}{2b-1}\left[(2b)^g - 1\right] = 2732$ sites, and in (b) for $g = 5$ with $N = 4667$ sites. In the top panel of both, (a) and (b), the overlaps (rescaled by a factor of N) were averaged over all sites w in the highest hierarchical level g, in the middle panel overlaps were averaged only over those w in level $g - 1$, and in the respective bottom panel for level $g - 2$. Note that every level the number of sites increases by a factor of $\sim 2b$, such that the vast majority of all sites w are typically located in these highest levels of the hierarchy. For those, these plots show that indeed $N|\langle w|\phi_i\rangle|^2 \sim 1$, typically, as assumed in Eq. (3.7), although these overlaps progressively vanish for those w in lower levels for eigenvectors of larger index i.
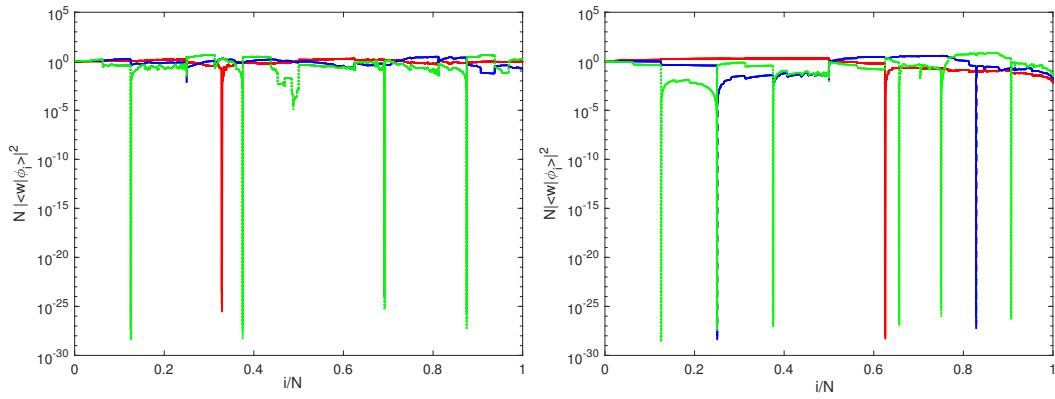
Figure 3.3: Plot of the overlaps $N \left| \langle w | \phi_i \rangle \right|^2$ in Hanoi networks for the searched-for node w with the Laplacian eigenvectors ϕ_i as a function of i/N, i.e. rescaled with the system size. Left is for HN3 and right is for HN5 with $g = 10, 11, 12, 13$. The red solid line is the overlap averaged over nodes in the highest hierarchy. Blue dashed line is the overlap averaged over second highest hierarchy. Green dotted line is the overlap averaged over third highest hierarchy. After rescaling the x-axis, those curves for each hierarchy of different systems size collapse well. $N \left| \langle w | \phi_i \rangle \right|^2$ is of the order $O(1)$, the maximum of which increases with hierarchical level l as $\ln l$.

According to Eq.(2.31), we find for general fractal networks that

$$\gamma_c \sim \begin{cases} N^{\frac{2}{d_s}-1}, & d_s < 2, \\ \\ const, & d_s > 2. \end{cases}$$

(3.10)

3.2 Evaluation of Efficiency of CTQW

To obtain the runtime complexity for the quantum search, we have to distinguish the following cases: For $d_s > 4$ both $I_{1,2}$ remain constant. It is then self-consistent to consider the spectral function in Eq.(3.8) for energies $|E| \ll \gamma_c \lambda_2$, which applies to both the ground state E_0 and the first excited state E_1 of $\mathcal{H}$ near the optimal γ_c. Expanding the remaining sum in Eq.(3.8) to leading order in E yields

$$F(E) \sim -\frac{1}{NE} + \frac{1}{\gamma} I_1 + \frac{E}{\gamma^2} I_2 + \dots, \qquad (|E| \ll \gamma_c \lambda_1),$$

(3.11)

Since $F(E_{0,1}) = 1$ from the eigenvalue condition in Eq.(3.4), we obtain a consistent balance to leading and sub-leading order only for $\gamma = \gamma_c = I_1$, thereby validating Eq.(3.9), and for $\frac{1}{NE_{0,1}} \sim \frac{E_{0,1}}{\gamma^2} I_2 \ll 1$, yielding

$$E_{0,1} \sim \pm \frac{1}{\sqrt{N}} \frac{I_1}{\sqrt{I_2}} = O\left(N^{-\frac{1}{2}}\right).$$

(3.12)

Then, the derivative of Eq.(3.11) provides $F'(E_{0,1}) \sim 2I_2/I_1^2$ such that according to Eq.(3.5) the initial state $|s\rangle$ overlaps with equal and finite weight with both, ground state and first excited state:

$$|\langle s \mid \psi_{0,1}\rangle|^2 \quad \sim \tfrac{1}{2} \quad .$$

(3.13)

As $E_i > \gamma_c \lambda_2$ for all $i \geq 2$, higher energy eigenstates do not contribute for large N, and we obtain from the first two terms of the transition amplitude in Eq.(3.6),

$$\left|\langle w \left| e^{i\mathcal{H}t} \right| s \rangle\right|^2 \sim \frac{1}{N} \left| \frac{e^{iE_0 t}}{E_0 F'(E_0)} + \frac{e^{iE_1 t}}{E_1 F'(E_1)} \right|^2,$$

(3.14)

$$\sim \frac{I_1^2}{I_2} \sin^2\left(\frac{2I_1}{\sqrt{I_2}} \frac{t}{\sqrt{N}}\right).$$

(3.15)

Thus, the transition probability oscillates and reaches its first maximum at a time

$$t = t_{\text{opt}} \sim \frac{\sqrt{I_2}}{I_1} \sqrt{N} = O\left(N^{\frac{1}{2}}\right), \tag{3.16}$$

at which point the transition probability becomes

$$p_{\text{opt}} = \left|\left\langle w \left| e^{i\mathcal{H}t_{\text{opt}}} \right| s \right\rangle\right|^2 \sim \frac{I_1^2}{I_2} = O(1). \tag{3.17}$$

Finally, to find the target node w with a probability of order unity, we need to run the quantum search $\sim 1/p_{\text{opt}}$ times, each for a time of t_{opt} at which a measurement must be executed. Thus, the runtime complexity for a successful search is given by

$$\frac{t_{\text{opt}}}{p_{\text{opt}}} \sim \left(\frac{I_2}{I_1^2}\right)^{\frac{3}{2}} \sqrt{N} = O\left(N^{\frac{1}{2}}\right), \qquad (d_s > 4). \tag{3.18}$$

For case $d_s = 4$, I_1 remains constant while $I_2 \sim \ln N$ acquires a logarithmic correction in the limit $d_s \to 4$. With that, the analysis of the previous case remains applicable, although the condition $|E| \ll \gamma_c \lambda_2$ is merely logarithmically satisfied. Thus, we obtain from Eq. (3.18) in this interpretation that

$$\frac{t_{\text{opt}}}{p_{\text{opt}}} = O\left(N^{\frac{1}{2}} \ln^{\frac{3}{2}} N\right), \qquad (d_s = 4). \tag{3.19}$$

For case $2 < d_s < 4$, I_1 remains constant while $I_2 \sim N^{\frac{4}{d_s}-1}$. However, by Eq.(3.12), this would imply $E_{0,1} \sim N^{-\frac{2}{d_s}}$, which would violate the condition of $E_{0,1} \ll \gamma_c \lambda_2$ where $\lambda_2 \sim \Lambda N^{-\frac{2}{d_s}}$. As a consequence, the expansion in Eq.(3.11) is no longer is valid and we have to reconsider Eq.(3.8) anew at $\gamma = \gamma_c \sim I_1$, but with $\gamma_c \lambda_2 \sim E_{0,1} = e_{0,1} I_1 \Lambda N^{-\frac{2}{d_s}}$. Then, Eq.(3.8) provides

$$F\left(E_{0,1}\right) \sim 1 - \frac{1}{I_1 \Lambda e_{0,1}} N^{\frac{2}{d_s}-1} + \frac{e_{0,1}}{I_1 \Lambda \left(1 - e_{0,1}\right)} N^{\frac{2}{d_s}-1} + \dots, \tag{3.20}$$

where the two leading corrections cancel self-consistently with a negative (positive) solution for e_0 (e_1). Then, $E_{0,1} F'\left(E_{0,1}\right) \sim N^{\frac{2}{d_s}-1}$, such that by Eq. (3.15), the transition probability diminishes for falling d_s and is at best

$$\left|\left\langle w \left| e^{i\mathcal{H}t} \right| s \right\rangle\right|^2 \lesssim \frac{1}{N} \left|\frac{1}{E_0 F'\left(E_0\right)}\right|^2 \sim N^{1-\frac{4}{d_s}}. \tag{3.21}$$

In turn, to accomplish any significant change in this transition amplitude requires at time of at least $t_{opt} \gtrsim \left| \langle w \left| e^{i\mathcal{H}t} \right| s \rangle \right| \sqrt{N} \sim N^{1-\frac{2}{d_s}}$. Thus, the runtime complexity finally is asymptotically bounded by

$$\frac{t_{opt}}{p_{opt}} \quad \gtrsim \quad N^{\frac{2}{d_s}}, \qquad (2 < d_s < 4). \tag{3.22}$$

which for $d_s \to 2$ also reproduces the known conclusion for the $2d$ regular lattice, up to logarithmic corrections.

The dynamics of CTQW is deeply related to the Laplacian and its spectral zeta function. RG applied on hierarchical networks reveals the dominant role of the spectral dimension d_s determining the transition probability and time complexity of CTQW. Fractals are geometries with arbitrary dimensions d. Conclusions derived through fractals reproduce the known results in regular lattices and random networks, where d_s is simply the spatial dimension of Euclidean space d or approaches to infinity. We suggest a condition for attaining the Grover limit using CTQW with the Hamiltonian in Eq.(3.1) is $d_s > 4$.

Chapter 4

Discrete Time Quantum Walk

Discrete-time quantum walks (DTQW) can be regarded as an analog of discrete-time random walks. In this chapter, we will describe basics in DTQW, and explore how the RG techniques can be used to analyze the numerical results, which reveal a general relation between the walk dimensions d_w of random walks and that of quantum walks with the Grover coin [36].

4.1 DTQW and the Walk Dimension

In random walks on graphs that is known as a stochastic process, a random walker jumps from one node to neighboring nodes. This process can be described mathematically in term of the probability $\rho(x, t)$ of finding the walker at node x after t time steps from the initial position. It can be written in a compact form as,

$$|\rho_{t+1}\rangle = \mathcal{U} \cdot |\rho_t\rangle, \tag{4.1}$$

where $|\rho_t\rangle$ is the vector with $\rho(x, t)$ as its $x-$Th. component. The transition matrix $\mathcal{U}$ is stochastic, whose columns sum to 1 as the conservation of probability. For random walks at large times, the probability density obeys the scaling collapse [68],

$$\rho(x, t) \sim t^{-\frac{d_f}{d_w}} f\left(\frac{l}{t^{\frac{1}{d_w}}}\right), \tag{4.2}$$

in which l is the distance of a node x from the initial position, d_f and d_w are the fractal dimension and walk dimension of underlying graphs, and f is a Gaussian scaling function.

The quantity often used to describe the spreading dynamics is mean-square displacement $\left\langle x^2 \right\rangle_t \sim t^{2/d_w}$ [55] or the first-passage times [116, 47]. On a translationally invariant lattice in any dimension d, random walks are diffusive with $d_w = 2$, while anomalous diffusion with $d_w \neq 2$ may arise in many transport processes [68, 38, 136, 72].

The master equation for a discrete time quantum walk can be similarly written as,

$$|\Psi_{t+1}\rangle = \mathcal{U} \cdot |\Psi_t\rangle, \tag{4.3}$$

where $|\Psi_t\rangle$ is the wave vector with $\Psi(\vec{x}, t)$ as its component. The probability of finding the walker in the node x at time t is $\rho(x, t) = \langle \Psi(\vec{x}, t) | \Psi(\vec{x}, t) \rangle$. The conservation of probability requires the unitarity of the transition matrix $\mathcal{U}$, $\mathcal{U}^\dagger \mathcal{U} = \mathbf{1}$, which affects significantly the structure of $\mathcal{U}$. In direct analogy to random walks, a quantum walk on a graph moves, in superposition, to neighboring nodes with equal amplitudes. However, such a process is non-unitary. The only exception is the trivial motion in a single direction on one dimensional line [127]. If the motion of the walker is assisted by an extra degree of freedom, it is possible to construct a unitary process at every point. The internal degree of freedom at each node is referee to the coin state or chirality [8]. The minimum dimension of the internal degree of freedom is matched to the degree of node.

The evolution operator for coined quantum walks is the combination of a shift and coin operator, called S and $\mathcal{C}$ respectively,

$$\mathcal{U} = S \cdot (\mathcal{C} \otimes \mathbf{1}_{N \times N}). \tag{4.4}$$

The propagator $\mathcal{U}$ is some $M \times M$ matrix with M reflecting a combination of a discrete set of N nodes and a certain number of internal degrees of freedom at each node. The walker lives in a Hilbert space $\mathcal{H}_t = \mathcal{H}_p \otimes \mathcal{H}_c$. It is customary to use the canonical basis as position site for the walker. The walker is usually initialized at the original, $|\psi_p\rangle_{initial} = |0\rangle_p$. The coin has a Hilbert space $\mathcal{H}_c$, which may take the canonical basis states, for example, $|0\rangle_c$ and $|1\rangle_c$ in one dimensional line as left and right chirality states. The initial state for the total system is $|\Psi\rangle_{initial} = |\psi_p\rangle_{initial} \otimes |\psi_c\rangle_{initial}$. To illustrate more details, we use quantum walks on one dimensional line with the Hadamard coin that is defined as

$$\mathcal{C} = \frac{1}{\sqrt{2}} \left(|0\rangle_c \langle 0| + |0\rangle_c \langle 1| + |1\rangle_c \langle 0| - |1\rangle_c \langle 1| \right). \tag{4.5}$$

The shift operator has a form

$$S = |0\rangle_c \langle 0| \otimes \sum_x |x-1\rangle_p \langle x| + |1\rangle_c \langle 1| \otimes \sum_x |x+1\rangle_p \langle x| \tag{4.6}$$

which allows the walker to move one step forwards if the coin state is $|0\rangle_c$, or one step backwards if the coin state is $|1\rangle_c$. Generally, QW applies an evolution operator to the coin state followed by a conditional shift operator to the total quantum system. The purpose of the coin operator is to render the coin state in a superposition.

The motivation to study DTQW is two-fold. The first motivation is the potential to be new tools for quantum algorithms. Second, techniques developed for analyzing quantum walks may provide insights to analyze quantum processes more generally. Coined quantum walk is proven to achieve Grover efficiency down to $d = 2$ up to logarithmic corrections [9]. The long time behavior of quantum walks on regular lattices has been proven that for almost every coin, the walk dimension d_w^{QW} defined in Eq.(4.2) is 1, which is the weak limit of the probability density function [79, 66]. On self-similar networks without translational invariance, it is unknown whether the scaling relation in Eq.(4.2) holds or not. We assume that a scaling relation also holds for the coined quantum walk on hierarchical networks, which is numerically verified in [55, 31]. Results in [55, 31] have lead to the conjecture that the walk dimension d_w in Eq.(4.2) for a quantum walk with a Grover coin always is half of that for the corresponding random walk, $d_w^{QW} = \frac{1}{2} d_w^{RW}$. Beyond the regular lattice, RG is a good method to explore the asymptotic scaling of a walk [68, 72, 116].

Assuming that we possess the eigensolution for the propagator, $\mathcal{U}\phi_j = u_j \phi_j$ in Eq.(4.4) with an orthonormal set of eigenvectors $\{\phi_j(x)\}_{j=1}^{M}$, then the formal solution of Eq.(4.3) becomes

$$\Psi(\vec{x}, t) = \sum_{\vec{y}} \mathcal{U}^t(\vec{x}, \vec{y}) \Psi(\vec{y}, 0) = \sum_{j=1}^{M} a_j (u_j)^t \phi_j(\vec{x}). \tag{4.7}$$

For a classical random walk, the site amplitude itself provides the probability density, $\rho(x, t) = \Psi(\vec{x}, t)$, while for the quantum walk it is $\rho(\vec{x}, t) = |\Psi(\vec{x}, t)|^2$. For the stochastic operator of a random walk, aside from the unique eigenvalue of the stationary state, the remaining eigenvalues have $|u_j| < 1$, thus, according to Eq.(4.7) , the dynamics is determined by $\rho(\vec{x}, t) \sim e^{-\epsilon t}$ for large times t with

$\epsilon = -\ln\max\{|u_j| < 1; 1 \leq j \leq M\}$. In turn, for unitary $\mathcal{U}$ all eigenvalues are uni-modular, $|u_j| = 1$, such that $u_j = e^{i\theta_j}$ with real θ_j.

$$\rho(\vec{x}, t) = A(\vec{x}) + \sum_{l<j}^{M} B_{j,l}(\vec{x}) \cos[(\theta_j - \theta_l)t], \tag{4.8}$$

where A, B only depend on position and initial conditions. The cut-off relevant for the long-time asymptotic behavior here is provided by $\Delta\theta = \min\{|\theta_j - \theta_l| > 0; 1 \leq j, l \leq M\}$. Furthermore, we note that a discrete Laplace transform of Eq. (4.8) provides

$$\tilde{\rho}(\vec{x}, z) = \frac{C(\vec{x})}{\prod_{j,l}^{M}\left[1 - z\, e^{i(\theta_j - \theta_l)}\right]}, \tag{4.9}$$

after placing all terms in the transformation of Eq. (4.8) on their main denominator. Thus, all poles of $\tilde{\rho}(\vec{x}, z)$ in Eq. (4.9) are located right on the unit-circle in the complex-z plane.

4.2   Renormalization Group for Random Walks

To apply the renormalization group to a walk problems, it is convenient to eliminate time t via a discrete Laplace transform (or generating function) of the evolution equation in the site basis [116] ,

$$\tilde{\Psi}(\vec{x}, z) = \sum_{t=0}^{\infty} \Psi(\vec{x}, t)\, z^t, \qquad \Psi(\vec{x}, t) = \oint_{|z|=1} \frac{dz}{2\pi i z} z^{-t}\tilde{\Psi}(\vec{x}, z) \tag{4.10}$$

Assuming a walk with an initial condition at $t = 0$ that is localized at the origin, we get

$$\tilde{\Psi}(\vec{x}, z) = \sum_{\vec{y}} z\mathcal{U}(\vec{x}, \vec{y})\, \tilde{\Psi}(\vec{y}, z), +\delta_{\vec{x},0}\psi_{IC}. \tag{4.11}$$

To obtain the time dependence of Ψ at $t \to \infty$, one can use the local information around $z = 1$.

On self-similar networks, the linear system in Eq.(4.11) can now be decimated recursively by algebraically eliminating specific site amplitudes [30, 31]. Typically, the matrix $z\mathcal{U}$ can be represented in terms of just a small set $\vec{a}_0(z) = (a_0, b_0, \ldots)$ of site-independent "hopping parameters" of the unrenormalized state. Each iteration constitutes an RG-step from level μ to $\mu + 1$, starting at the unrenormalized state with $\mu = 0$. The $\vec{a}_\mu$ arises due to the mapping

$$\vec{a}_{\mu+1}(z) = \mathcal{RG}[\vec{a}_\mu(z)]. \tag{4.12}$$

which is the RG-flow. Hopping parameters parametrized $\vec{a}_\mu(z)$ actually contains the information of a system with b^μ nodes.

While the RG-flow in Eq. (4.12) usually can not be solved in general, the properties of its fixed points

$$\vec{a}_\infty = \mathcal{RG}(\vec{a}_\infty) \tag{4.13}$$

for $\mu \to \infty$ can be explored to reveal the dynamics of the walk asymptotically at large length and time scales. Specifically, $\mu \to \infty$ corresponds to a diverging system size while $|z| \to 1$ according to Eq. (4.10) accesses the large-t limit.

We can linearize the RG-flow in Eq. (4.12) via the Ansatz

$$\vec{a}_\mu(z) \sim \vec{a}_\infty + (1-z)\vec{\alpha}_\mu, \tag{4.14}$$

for $z \to 1$ and $\mu \to \infty$ with $(1-z)\vec{\alpha}_\mu \ll 1$. Then, we get the linear system

$$\vec{\alpha}_{\mu+1} = \vec{\alpha}_\mu \circ J, \tag{4.15}$$

with the Jacobean matrix

$$J = \left(\left. \frac{\partial \mathcal{RG}}{\partial \vec{a}_\mu} \right|_{\mu \to \infty} \right), \tag{4.16}$$

such that the solutions of Eq. (4.15) are linear combinations,

$$\vec{\alpha}_\mu \sim \lambda_1^\mu \vec{v}_1 \mathcal{A}_1 + \lambda_2^\mu \vec{v}_2 \mathcal{A}_2 + \ldots, \tag{4.17}$$

where λ_j are the eigenvalues of J in descending order, and $\vec{v}_j$ the associated eigenvectors.

For a random walk, almost all poles of $\vec{a}_\mu(z)$ are on the real-z axis with $|z| > 1$. Let z_μ being the pole that is closest to $z = 1$,

$$z_\mu \sim 1 + \epsilon_\mu, \qquad (\epsilon_\mu \to 0) \tag{4.18}$$

with real ϵ_μ. Then, the generic form for a simple pole near $z = 1$ with $\vec{a}_\mu(1) = \vec{a}_\infty$ is:

$$\vec{a}_\mu(z) \quad \sim \quad \frac{1 - z_\mu}{z - z_\mu} \vec{a}_\infty \sim \vec{a}_\infty \left[1 - \frac{1}{\epsilon_\mu}(1-z) + \ldots \right]. \tag{4.19}$$

Note that $1/\epsilon_\mu$ is not only the most divergent term of order $1 - z$, it is the only one. This is reflected

in Eq. (4.17) in the fact that there is only a single divergent eigenvalue, $\lambda_1 > 1$, in a classical walk. The comparison implies

$$\epsilon_\mu \sim |\vec{\alpha}_\mu|^{-1} \sim \lambda_1^{-\mu} \tag{4.20}$$

at the cross-over $(1-z)\alpha_\mu \sim 1$ that sets the cut-off.

With $\tilde{\rho}(\vec{x}, z) = f_{\vec{x}}[\vec{a}_\mu(z)]$, the classical probability density now attains the form for $z \to 1$:

$$\tilde{\rho}(\vec{x}, z) \sim \frac{1 - z'_\mu}{z - z'_\mu} A, \tag{4.21}$$

where its closest pole $z'_\mu \sim 1 + C\epsilon_\mu$ may differ from z_μ, but only by a constant C that does not affect the scaling. To see this, we consider the inverse Laplace transform and inserting Eq. (4.21):

$$\rho(\vec{x}, t) = \oint \frac{dz}{2\pi i z} z^{-t} \tilde{\rho}(\vec{x}, z) \sim AC\epsilon_\mu e^{-C\epsilon_\mu t}, \tag{4.22}$$

where ϵ_μ provides the cut-off. If we now calculate temporal moments, say, of the first passage time at some site $\vec{x}$, t is

$$\langle t^n \rangle_k = \frac{1}{\mathcal{N}} \int_0^\infty dt\, t^n \rho(\vec{x}, t) \sim \epsilon_\mu^{-n}, \tag{4.23}$$

where the norm $\mathcal{N}$ absorbs any factor so that $\langle t^0 \rangle_\mu \equiv 1$. Then, Eq. (4.20) implies for the scaling of the characteristic time-scale T with system size $N = 2^\mu$ for networks we consider:

$$T = \left[\langle t^n \rangle_\mu \right]^{\frac{1}{n}} \sim \epsilon_\mu^{-1} \sim \lambda_1^\mu \sim (2^\mu)^{\log_2 \lambda_1} \sim L^{d_w} = N^{d_w/d_f}, \tag{4.24}$$

such that the classical walk dimension becomes

$$d_w^{RW} = \log_2 \lambda_1. \tag{4.25}$$

We find the scaling of ϵ_μ^{-1} translates into that of the first passage time.

4.2.1 Application of RG on One Dimensional Line

We use the example of RW on one dimensional line to illustrate this procedure, where Eq. (4.11) reduces to

$$\tilde{\Psi}_x\left(z\right) = \delta_{x,0} + zB\tilde{\Psi}_x\left(z\right) + zA\tilde{\Psi}_{x-1}\left(z\right) + zA\tilde{\Psi}_{x+1}\left(z\right), \tag{4.26}$$

where A represents left and right movement, B represents staying in place. To simplify the RG calculation, we are interested in the unbiased case($A = 1/2, B = 0$). We write Eq. (4.26) for any even $x \neq 0$:

$$
\begin{aligned}
\tilde{\Psi}_{x-1}\left(z\right) &= a_\mu\tilde{\Psi}_{x-2}\left(z\right) + b_\mu\tilde{\Psi}_{x-1}\left(z\right) + a_\mu\tilde{\Psi}_x\left(z\right) = \frac{a_\mu}{1-b_\mu}\tilde{\Psi}_{x-2}\left(z\right) + \frac{a_\mu}{1-b_\mu}\tilde{\Psi}_x\left(z\right), \\
\tilde{\Psi}_x\left(z\right) &= a_\mu\tilde{\Psi}_{x-1}\left(z\right) + b_\mu\tilde{\Psi}_x\left(z\right) + a_\mu\tilde{\Psi}_{x+1}\left(z\right), \\
\tilde{\Psi}_{x+1}\left(z\right) &= a_\mu\tilde{\Psi}_x\left(z\right) + b_\mu\tilde{\Psi}_{x+1}\left(z\right) + a_\mu\tilde{\Psi}_{x+2}\left(z\right) = \frac{a_\mu}{1-b_\mu}\tilde{\Psi}_x\left(z\right) + \frac{a_\mu}{1-b_\mu}\tilde{\Psi}_{x+2}\left(z\right),
\end{aligned}
$$

with $a_0 = z/2$, and $b_0 = 0$. Again, eliminating algebraically all odd-site amplitudes, we obtain

$$a_{\mu+1} = \frac{a_\mu^2}{1-b_\mu} \qquad b = b_\mu + \frac{2a_\mu^2}{1-b_\mu}, \tag{4.27}$$

for which the fix point is $a_\infty = 0, b_\infty = 1$.

Perturbing the RG-flow in Eq.(4.27),

$$\{a,b\} = \{a,b\}_\infty + (1-z)\{\alpha,\beta\}_\mu.$$

For $z \to 1$ and large μ, the Jacobean is defined as

$$
\begin{aligned}
J &= \left(\left.\frac{\partial\left(a_{\mu+1}, b_{\mu+1}\right)}{\partial\left(a_\mu, b_\mu\right)}\right|_{\mu\to\infty}\right), \\
&= \begin{pmatrix} -\frac{2a_\infty}{b_\infty-1} & \frac{a_\infty^2}{(b_\infty-1)^2} \\ -\frac{4a_\infty}{b_\infty-1} & \frac{2a_\infty^2}{(b_\infty-1)^2} + 1 \end{pmatrix}.
\end{aligned} \tag{4.28}
$$

Since both numerators and denominators in the Jacobean vanish, a correlated solution has to be constructed that "peals off" the leading behavior to glance into the boundary layer. Using the ansatz

$a_\mu \sim A_\mu \cdot \varepsilon^\mu$ and $b_\mu \sim 1 - B_\mu \cdot \varepsilon^\mu$, the Jacobean matrix can be obtained from

$$\varepsilon A_{\mu+1} = \frac{A_\mu^2}{B_\mu}, \qquad \varepsilon B_{\mu+1} = B_\mu - \frac{2A_\mu^2}{B_\mu} \tag{4.29}$$

with a single fixed point that self-consistently determines $\frac{A_\infty}{B_\infty} = \varepsilon = \frac{1}{2}$. The Jacobean and its eigenvalues are

$$\frac{\partial \left(A_{\mu+1}, B_{\mu+1} \right)}{\partial \left(A_\mu, B_\mu \right)} = \begin{bmatrix} 2 & -1/2 \\ -4 & 3 \end{bmatrix} \Longrightarrow \lambda = \{4, 1\} . \tag{4.30}$$

From Eq.(4.25), we derive $d_w = 2$ for the diffusive solution.

4.3 Renormalization Group for Quantum Walks

In this section, we study the RG on quantum walks on self-similar networks. The Laplace-poles closest to $|z| \to 1$ assume an important role. Now, the location of the poles in the complex-z plane for any observable like the probability density do not necessarily correspond to those of $\vec{a}_\mu (z)$, although $\tilde{\rho}(\vec{x}, z) = f_{\vec{x}} [\vec{a}_\mu (z)]$ is a functional of the hopping parameters. However, this distinction does not pose a problem for the real poles in the classical walk: poles flows radially along the real-z axis towards $z = 1$ with the same scaling. In contrast, for QW observables have strictly uni-modular poles, such as in Eq. (4.9), that flow only tangentially on the unit circle in the complex-z plane, while the renormalized hopping parameters $\vec{a}_\mu (z)$ individually have poles that flow radially and tangentially shown in [37]. Since in RW the radial flow in poles of $\vec{a}_\mu (z)$ affects directly the scaling of $\tilde{\rho}(\vec{x}, z)$, intuitively the tangential flow in poles of $\vec{a}_\mu (z)$ is related to the that in $\tilde{\rho}(\vec{x}, z)$.

4.3.1 Application of RG on One Dimensional Line

We again illustrate RG in quantum walks via the example of one dimensional line. It is known the same asymptotic scaling in Eq.(4.2) apply for all the coins on lattices [79, 66]. Without loss of generality, we use the Hadamard coin in Eq.(4.5), whose matrix form is

$$\mathcal{C}_H = \frac{1}{\sqrt{2}} \begin{pmatrix} 1 & 1 \\ 1 & -1 \end{pmatrix} . \tag{4.31}$$

We generalize the shift operator in Eq.(4.6) to

$$S = \sum_x \left\{ P \otimes |x-1\rangle \langle x| + Q \otimes |x+1\rangle \langle x| + R \otimes |x\rangle \langle x| \right\}, \tag{4.32}$$

where the shift matrix P, Q and R are parametrized for moving left, right and staying in place respectively,

$$P = \begin{pmatrix} 1 & 0 \\ 0 & 0 \end{pmatrix}, \qquad Q = \begin{pmatrix} 0 & 0 \\ 0 & 1 \end{pmatrix}, \qquad R = \begin{pmatrix} 0 & 0 \\ 0 & 0 \end{pmatrix}. \tag{4.33}$$

Hence, $\mathcal{U}$ from Eq.(4.4)

$$\mathcal{U} = \sum_x \left\{ A \otimes |x-1\rangle \langle x| + B \otimes |x+1\rangle \langle x| + M \otimes |x\rangle \langle x| \right\}, \tag{4.34}$$

with $A = P \cdot \mathcal{C}, B = Q \cdot \mathcal{C}, M = R \cdot \mathcal{C}.$

The master equation in Eq.(4.11) becomes

$$\tilde{\Psi}_x(z) = \delta_{x,0} + zM\tilde{\Psi}_x(z) + zA\tilde{\Psi}_{x-1}(z) + zB\tilde{\Psi}_{x+1}(z), \tag{4.35}$$

where the initial position is located at the origin. The decimation from step μ to $\mu+1$ reads

$$\begin{aligned}
\tilde{\Psi}_{x-1}(z) &= A_\mu \tilde{\Psi}_{x-2}(z) + M_\mu \tilde{\Psi}_{x-1}(z) + B_\mu \tilde{\Psi}_x(z), \\
\tilde{\Psi}_x(z) &= A_\mu \tilde{\Psi}_{x-1}(z) + M_\mu \tilde{\Psi}_x(z) + B_\mu \tilde{\Psi}_{x+1}(z) + \delta_{x,0}\Psi_{IC}, \\
\tilde{\Psi}_{x+1}(z) &= A_\mu \tilde{\Psi}_x(z) + M_\mu \tilde{\Psi}_{x+1}(z) + B_\mu \tilde{\Psi}_{x+2}(z),
\end{aligned} \tag{4.36}$$

solving for

$$\tilde{\Psi}_x(z) = A_{\mu+1}\tilde{\Psi}_{x-2}(z) + M_{\mu+1}\tilde{\Psi}_x(z) + B_{\mu+1}\tilde{\Psi}_{x+2}(z) + \delta_{x,0}\Psi_{IC}, \tag{4.37}$$

with RG flow

$$
\begin{aligned}
A_{\mu+1} &= A_\mu \left(I - M_\mu \right)^{-1} A_\mu, \\
B_{\mu+1} &= B_\mu \left(I - M_\mu \right)^{-1} B_\mu, \\
M_{\mu+1} &= M_\mu + A_\mu \left(I - M_\mu \right)^{-1} B_\mu + B_\mu \left(I - M_\mu \right)^{-1} A_\mu.
\end{aligned}
$$

What is special to QW compared to RW is that the unitarity of $\mathcal{U}$ imposes conditions on matrices A, B and M such that

$$
\begin{aligned}
\mathbf{1} &= A^\dagger A + B^\dagger B + M^\dagger M, \\
\mathbf{0} &= A^\dagger M + M^\dagger B = \left(B^\dagger M + M^\dagger A \right)^\dagger, \\
\mathbf{0} &= A^\dagger B = \left(B^\dagger A \right)^\dagger.
\end{aligned}
\tag{4.38}
$$

The parameterization emerges as [55],

$$
A_\mu = \begin{pmatrix} a_\mu & 0 \\ 0 & 0 \end{pmatrix}, \qquad
B_\mu = \begin{pmatrix} 0 & 0 \\ 0 & -a_\mu \end{pmatrix}, \qquad
M_\mu = \begin{pmatrix} 0 & b_\mu \\ b_\mu & 0 \end{pmatrix}.
\tag{4.39}
$$

which yields recursions

$$
a_{\mu+1} = \frac{a_\mu^2}{\sqrt{2}\left(1 - \sqrt{2} b_\mu + b_\mu^2 \right)} \qquad
b_{\mu+1} = b_\mu + \frac{a_\mu^2 \left(\sqrt{2} - 2 b_\mu \right)}{-2 + 2\sqrt{2} b_\mu - 2 b_\mu^2}.
\tag{4.40}
$$

Fixed points are $\{a_\infty, b_\infty\} = \{1/\sqrt{2}, 1/\sqrt{2}\}$, and the Jacobean and its eigenvalues are

$$
J = \begin{pmatrix} 2 & 0 \\ 0 & 2 \end{pmatrix} \implies \lambda = \{2, 2\}.
\tag{4.41}
$$

Here, we take one step further to derive functional relation between $\tilde{\Psi}_x(z)$, $\rho_x(z)$ $\left(\left| \tilde{\Psi}_x(z) \right|^2 \right)$ and $\{a_\mu, b_\mu\}$ for quantum walk on one dimensional line $N = 2^g$ with periodic boundary condition. After $g - 2$ RG steps, four sites remain with

$$
\begin{aligned}
\tilde{\Psi}_0\left(z\right) &= A_{g-2}\tilde{\Psi}_{\frac{3N}{4}}\left(z\right) + M_{g-2}\tilde{\Psi}_0\left(z\right) + B_{g-2}\tilde{\Psi}_{\frac{N}{4}}\left(z\right) + \Psi_{IC}, \\
\tilde{\Psi}_{\frac{N}{4}}\left(z\right) &= A_{g-2}\tilde{\Psi}_0\left(z\right) + M_{g-2}\tilde{\Psi}_{\frac{N}{4}}\left(z\right) + B_{g-2}\tilde{\Psi}_{\frac{N}{2}}\left(z\right), \qquad (4.42) \\
\tilde{\Psi}_{\frac{N}{2}}\left(z\right) &= A_{g-2}\tilde{\Psi}_{\frac{N}{4}}\left(z\right) + M_{g-2}\tilde{\Psi}_{\frac{N}{2}}\left(z\right) + B_{g-2}\tilde{\Psi}_{\frac{3N}{4}}\left(z\right), \\
\tilde{\Psi}_{\frac{3N}{4}}\left(z\right) &= A_{g-2}\tilde{\Psi}_{\frac{N}{2}}\left(z\right) + M_{g-2}\tilde{\Psi}_{\frac{3N}{4}}\left(z\right) + B_{g-2}\tilde{\Psi}_0\left(z\right). \qquad (4.43)
\end{aligned}
$$

Therefore, we obtain

$$
\tilde{\Psi}_0\left(z\right) = \left[\mathbf{1} - \left(A_g + B_g + M_g\right)\right]^{-1}\Psi_{IC}. \qquad (4.44)
$$

Due to the constraints on hopping parameters in Eq.(4.38), $\{a_\mu, b_\mu\}$ satisfies

$$
\left|a_\mu\left(z\right)\right|^2 + \left|b_\mu\left(z\right)\right|^2 = 1, \qquad (4.45)
$$

which implies singularity of $\{a_\mu, b_\mu\}$ is not on the unit circle $|z = 1|$. Matrices A, B and M are unitary, and the singularity of $\tilde{\Psi}_0\left(z\right)$ and $\left|\tilde{\Psi}_0\left(z\right)\right|^2$ can be expressed as a function of z and the set of eigenvalues and eigenvectors, which is on the unit circle.

4.3.2   Analysis of Laplace Poles

Results in [31] have lead to the conjecture that the walk dimension d_w in Eq.(4.2) of a quantum walk with a Grover coin always is half that of the corresponding random walk, $d_w^{QW} = \frac{1}{2}d_w^{RW}$. In this section, we extend the RG analysis on Laplace poles used for classical walks to quantum walks with Grover coin. The general definition for the Grover coin is

$$
\mathcal{C}_G = 2\frac{|\mathbf{1}\rangle\langle\mathbf{1}|}{\langle\mathbf{1}|\mathbf{1}\rangle} - \mathbf{1}. \qquad (4.46)
$$

In random walks, as shown in Sec.(4.2), the poles of the the hopping parameters are on the real-z axis. For the long time behavior, the most relevant poles are those closest to $z = +1$. In quantum walks with a purely real coin, such as the Grover coin, all the poles are in conjugate pairs [109]. Poles of

$\vec{a}_\mu$ flow to the unit circle of the complex-z plane in radial and tangential directions [37] as decimation, parameterized as

$$z_\mu^{(\pm)} \sim (1 + \epsilon_\mu) e^{\pm i\theta_\mu} \sim 1 \pm i\theta_\mu + \epsilon_\mu, \quad \left(1 \gg \theta_\mu \gg \epsilon_\mu \gg \theta_\mu^2\right) \tag{4.47}$$

for large μ, while there also might be a real pole, $z_\mu^{(0)} \sim 1 + \epsilon_\mu$. Previous discussions suggest that radial flow is faster than tangential flow ($\theta_\mu \gg \epsilon_\mu$) for these poles [30, 31]. This is also confirmed numerically [37].

Then, like in Eq. (4.19) for the classical case, the most generic expression for any hopping parameter is:

$$\vec{a}_\mu(z) \sim \vec{a}_\infty \left[\frac{pe^{i\phi}}{2\cos\phi} \frac{1 - z_\mu^{(+)}}{z - z_\mu^{(+)}} + \frac{pe^{-i\phi}}{2\cos\phi} \frac{1 - z_\mu^{(-)}}{z - z_\mu^{(-)}} + (1 - p) \frac{1 - z_\mu^{(0)}}{z - z_\mu^{(0)}} \right] \tag{4.48}$$

with a real pole at $z^{(0)}$ and complex conjugate pairs at $z_\mu^{(\pm)} = \left[z_\mu^{(\mp)} \right]^*$ that are closest to $z \to 1$. Note that again $\vec{a}_\mu(1) = \vec{a}_\infty$, but also $\vec{a}_\mu(z^*) = [\vec{a}_\mu(z)]^*$. Here, p determines the balance in weight between real and complex roots, while $\phi \neq 0$ allows for a complex residue at the pole. Expanding similar to Eq. (4.19) in the classical case, we find

$$\vec{a}_\mu(z) \sim \vec{a}_\infty \left(1 - \left[\frac{B}{\epsilon_\mu} + C \begin{cases} \frac{\epsilon_\mu}{\theta_\mu^2}, & \phi = 0, \\ \frac{1}{\theta_\mu}, & \phi \neq 0 \end{cases} \right] (1 - z) + \ldots \right), \tag{4.49}$$

with some constants B, C. Thus, allowing for the tangential flow in Eq. (4.47) affords a second independent divergence at order $1 - z$ in Eq. (4.49). Hence, we expect both, leading and sub-leading eigenvalues $\lambda_{1,2} > 1$ in Eq. (4.17), to match up with Eq. (4.49). As in the classical case, Eq. (4.20), it is $\epsilon_\mu \sim \lambda_1^{-\mu}$, since the B-term is always larger than any C-term in Eq. (4.49). Comparing Eq. (4.49) with Eq. (4.17) assuming real residues ($\phi = 0$), it is $\epsilon_\mu / \theta_\mu^2 \sim \lambda_2^\mu$, i.e.,

$$\theta_\mu \sim \left(\sqrt{\lambda_1 \lambda_2} \right)^{-\mu}. \tag{4.50}$$

We know that there is a functional relation between the hopping parameters and the PDF, $\tilde{\rho}(\vec{x}, z) = f_{\vec{x}}[\vec{a}_k(z)]$. The functional must be such that the leading scaling resulting from the radial flow of poles in $\vec{a}_k(z)$ will cancel in the process. In fractal networks, it is not generally proven that the tangential

flow of poles in $\vec{a}_k(z)$ translates exactly into that of the poles in $\tilde{\rho}(\vec{x}, z)$ while the radial flow cancels. Nevertheless, this can be be shown explicitly for the one dimensional line [37]. Therefore, we argue that θ_μ describes the tangential flow of poles in $\tilde{\rho}(\vec{x}, z)$, which yields the walk dimension $d_w^{QW} = \log_2 \sqrt{\lambda_1 \lambda_2}$. Although the poles of $\rho(\overrightarrow{x}, z)$ that reside on the unit circle, either are closest to the real axis, or converge to points on the unit circle, we assume that the dominant are those closest to real axis $z \to 1$.

We can explain some of the previous results and the conjecture of $d_w^{QW} = \frac{1}{2} d_w^{RW}$ [30, 31]. The first case is the one dimensional line with any coin. The RG analysis yields degenerate Jacobean eigenvalues, $\lambda_1^{QW} = \lambda_2^{QW} = 2$ in quantum walks, and $\lambda_1^{RW} = 4$ in random walks, such that there is no distinction, i.e., $\lambda_1^{RW} = \lambda_1^{QW} \lambda_2^{QW}$. RG for QW with the Grover coin on the the dual Sierpinski gasket (DSG) [30] yields $\lambda_1^{QW} = 3$, $\lambda_2^{QW} = \frac{5}{3}$, and the RG for RW yields $\lambda_1^{RW} = 5$, such that $\lambda_1^{RW} = \lambda_1^{QW} \lambda_2^{QW}$ provides the numerically determined scaling, $d_w^{QW} = \log_2 \sqrt{5}$. The same pattern holds for the two Migdal-Kadanoff networks analyzed in [31]: For the 3-regular network MK3, it is $\lambda_1^{QW} = 7$ and $\lambda_2^{QW} = 3$ such that $\lambda_1^{QW} \lambda_2^{QW} = \lambda_1^{RW} = 21$, and for the 4-regular network MK4 it is $\lambda_1^{QW} = 13$ and $\lambda_2^{QW} = \frac{19}{7}$, such that $\lambda_1^{QW} \lambda_2^{QW} = \lambda_1^{RW} = \frac{247}{7}$. However, to HN3 with $\lambda_1^{QW} = 2$ and $\lambda_2^{QW} = \left(1 + \sqrt{17}\right)/4$, the product $\lambda_1^{QW} \lambda_2^{QW}$ is unrelated to the classical eigenvalue $\lambda_1^{RW} = 2\left(\sqrt{5} - 1\right)$. This suggests that the relation in Eq. (4.50) is not as fundamental. Some of the assumptions leading to it are violated by HN3. Even the simple alternative of $\phi \neq 0$ n Eq. (4.49), implying $\theta_\mu \sim \lambda_2^{-\mu}$, does not explain the discrepancy. Furthermore, it appears that a more general argument than Eq. (4.50) must exists to justify the conjecture $d_w^{QW} = \frac{1}{2} d_w^{RW}$.

Chapter 5

Griffiths Phase on Hierarchical Networks

In this chapter, we study the Griffiths phase on hierarchical networks that particularly possess a large-world architecture and hierarchical modularity. This class of hierarchical networks has been used to model the brain networks. Brain networks exhibit a feature of hierarchical modularity. Modules in each hierarchy are grouped into larger modules in the next higher hierarchy [122, 89, 75]. Strong modularity is advantageous for creating a balance between functional segregation and integration, efficient recurrent processing within modules and synchronous processing[122]. To ensure the efficient cooperation between modules, any local area can be linked to any other in a short path, i.e. a small-world feature [122]. Furthermore, it has been argued that information processing networks such as neural systems and computer circuits possess a fractal feature of embedding topologically complex systems in a relatively low-dimensional physical space [89, 75, 19].

Networks that combine the properties of a finite fractal dimension d_f and the small-world topology are proposed as a solution to incorporate progressively weaker inter-module edges while maintaining well defined modules [63]. Previous work models interconnections in brains using finite hierarchical modular networks (HMN) with a finite fractal dimension. The common structural characteristics of these networks is the hierarchical level-dependent inter-module wiring probabilities. Examples are shown in Fig.(5.1). A novel phase called Griffiths phase (GP) using fundamental dynamical models, emerges on these networks, which resides between the absorbing state and the active state, shown in Fig.(5.2). The Griffiths phase is characterized by generic power-laws over a broad region in the
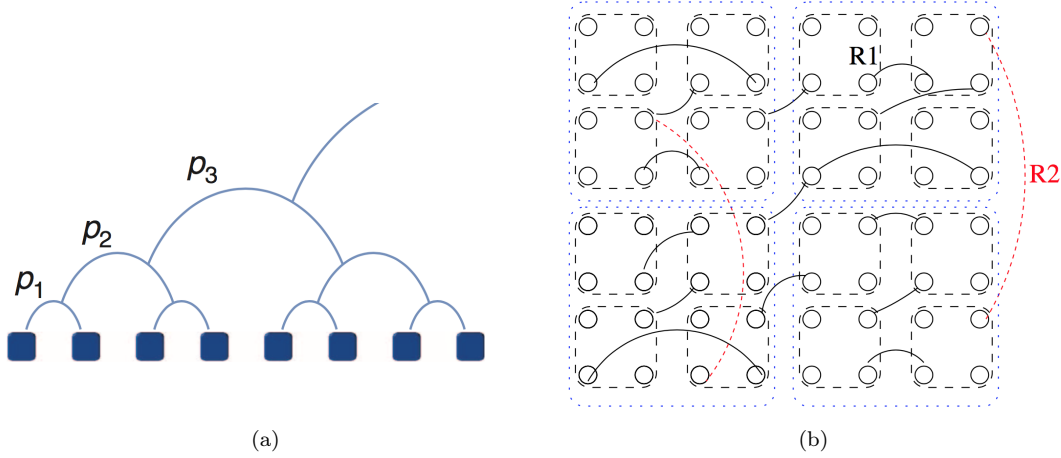
Figure 5.1: (a) Initially, nodes are grouped into fully connected modules of size m_0. Nodes in b different modules are clustered recursively into higher level blocks (for example, $b = 2$) linking their respective nodes with hierarchical level-dependent wiring probabilities: $p_i = \alpha p^i$ with $p \in (0, 1)$ and α as a constant [93]. (b) Dashed lines frame bottom level nodes, which are fully connected there, dotted lines frame the nodes of the next level. Solid lines denoted R1 are randomly chosen connections among the bottom level modules, ensuring single connectedness of the network, while those denoted R2 provide random connections on the next level [103].

parameter space [93, 103].

The criticality hypothesis states that the brain may operate at the borderline between the sustained active and inactive state. For many systems with a critical phase transition, self-organized criticality is easily implemented by a mechanism that increases the control parameter in the inactive phase and decreases it in the active phase. A single critical point has been reported in various biological processes such as gene expression [98], cell growth [62] and neuronal avalanches [21]. In different contexts, the critical point enables optimal transmission and storage of information [107, 20], maximal sensitivity to stimuli [77], optimal computational capabilities [82].

However, a critical point is too small a target to hit for a real biological tuning process with noise and imperfections. An interesting phenomenon found by empirical studies is that brain networks exhibit a stretched critical region [17, 117, 134, 119]. The stretched region is explained by the Griffiths phase as an alternative mechanism for critical behavior without fine tuning [93]. It is proposed that the heterogeneous structure of brain networks induces the Griffiths phase that eventually enhances the self-organization mechanism [93]. The existence of the Griffiths phase is successfully confirmed using fundamental dynamical models that describe the activity propagation, the Susceptible-Infected-Susceptible (SIS) model or the Contact Process (CP) [93, 103].
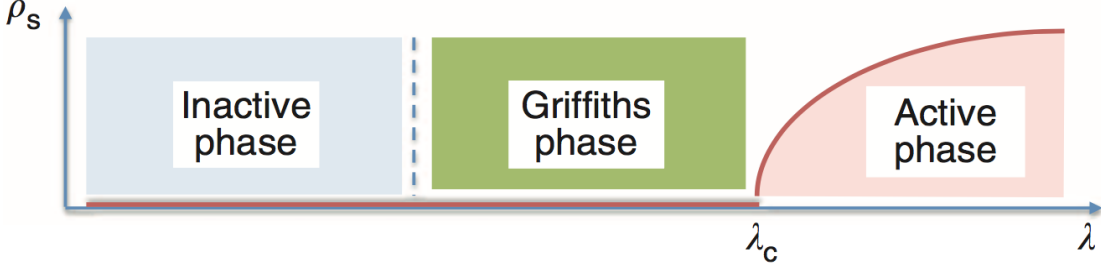
Figure 5.2:   The schematic diagram for the Griffiths phase [93]. A Griffiths phase exhibits a broad region of power-law scaling. The stationary density of activity, ρ_s, is depicted as a function of the spreading rate λ.

5.1   Hierarchical Modular Models

It is conjectured that plain modular networks do not support the Griffiths phase, and disorder in different scales significantly influences properties of critical behaviors [93]. We further explore the Griffith phase in other hierarchical networks, and especially extend it to new structures that are designed based on HN3 [83]. To model the modular property, each single node x in HN3 is replaced by a fully-connected clique that contains a finite number m of nodes, thus forming a network with size $N = n \times m$. By introducing different classes of inter-module edges, we aim to explore what hierarchical connectivity pattern provides the sufficient heterogeneity to induce the Griffiths phase on finite dimensional networks. We propose two connectivity patterns between modules in the same hierarchy. In the first paradigm, the single edge in the original HN3 is now formed by two randomly chosen nodes in different cliques, denoted as HMN1. The second paradigm is inspired by previous hierarchical modular models [93, 103]. To distinguish it from HMN1, we denote it as HMN2. Previous models share common features, hierarchical construction of modules and level-dependent wiring probabilities. Modules are grouped to form larger modules in the next level. They are connected in either a stochastic way with a level-dependent probability p_i or a deterministic way with a level-dependent number of edges.

An infinite dimensional network does not support the Griffiths phase, since the spreading is fast due to the short paths between any pair of nodes[93]. To maintain a finite fractal dimension, the number of inter-module edges is stable across hierarchical levels. In this work, we use the stochastic scheme to construct HMN2. As the size of modules increases with each hierarchical level, the inter-module wiring probability decreases. In HMN2, for the first hierarchy, modules in this level are basic cliques. Labels of basic cliques in HMN1 and HMN2 inherit the original labeling of HN3 in Eq.(2.1). Starting from

the second hierarchy, the clique labeled as $2(2j-1)$ is grouped with the neighbor clique $2(2j-1)-1$ and $2(2j-1)+1$ forming a module. For the third hierarchy, the clique labeled as $2^2(2j-1)$ is grouped with three left neighbor cliques to the clique $2^2(2j-1)-3$ and three right neighbor cliques to the clique $2^2(2j-1)+3$. Repeating this procedure g generations, the size of modules in i-th generation is $m(2^i-1)$. The number of all possible stochastic edges between two modules is $m^2\left(4^i-2^{i+1}+1\right)$. Thus, to ensure at least one edge between them to exist, the level-dependent probability p_i is bounded by $1/\left(m^2\left(4^i-2^{i+1}+1\right)\right)$.

5.2   SIS Model and Spectral Analysis

We base our study on the SIS model, in which each node in networks is described by a binary state, active ($\rho = 1$) or inactive ($\rho = 0$). An active node is deactivated with a unit rate; otherwise, it propagates the active state to its inactive neighbors with a rate λ. The evolution equation for the probability $\rho_x(t)$ that node x is active at time t is

$$\frac{d}{dt}\rho_x(t) \;\; = \;\; -\rho_x(t) + \sigma\left[1 - \rho_x(t)\right]\sum_{y=1}^{N} A_{xy}\rho_y(t), \tag{5.1}$$

in which A is the network adjacency matrix. The Laplacian matrix of a graph in Eq.(2.4) can be re-written with the adjacency matrix as

$$L_{xy} \;\; = \;\; = \delta_{xy}\sum_{z} A_{yz} - A_{xy}, \tag{5.2}$$

where L_{xy} is equal to $-A_{xy}$ when $x \neq y$, and L_{xx} is equal to $\sum_{y\neq x} A_{xy}$, i.e. the degree of node x. In this chapter, to distinguish the eigenvalues and eigenvectors of the adjacency matrix A and the Laplacian matrix L, we denote respectively as λ_i^A, ϕ_i^A and λ_i^L, ϕ_i^L.

   We briefly introduce the method used to perform the simulation for the SIS model. The large-scale numerical simulation method for the SIS model developed in [58] determines the critical propagation rate σ_c efficiently for various networks. This algorithm considers the SIS model in continuous time. At each time step, one randomly chosen active node deactivates with the probability $N_i/(N_i + \sigma N_n)$ where N_i is the number of active nodes at time t, and N_n is the number of edges emanating from them. With complementary probability $\sigma N_n/(N_i + \sigma N_n)$, the active state is transmitted to one inactive neighbor of the randomly selected node. Time is incremented by $\triangle t = 1/(N_i + \sigma N_n)$. This

process is iterated after updating the system.

As a complement to the computational approach, the spectral analysis on the adjacency and Laplacian matrix of networks can be also conducted. Griffiths phase is closely related to the structural disorder and localization of activity in special regions on networks Quenched Mean-Field (QMF) approximation suggests a localized principle eigenvector of the adjacency matrix indicates the network heterogeneity, which has been used to quantify the localization on networks above the critical propagation rate in the dynamical model [64]. Thus, this concept has been applied to analytically explain the emergence of rare regions and Griffiths phase [93, 103, 99].

The second spectral analysis considers the Lifshitz tails in the spectral density of the Laplacian. Lifshitz tails have been related to the Griffiths singularity in the equilibrium systems [96]. For synchronization and spreading dynamics on networks, simulation and Quenched Mean Field approximation indicate a connection between the Lifshitz tail and the slow dynamics [101, 93, 128]. In this section, the tail distribution of the Laplacian eigenvalues is tested to examine how well it predicts the Griffiths phase.

5.2.1   Spectral Analysis on the Agency Matrix

QMF approximation applies a spectral analysis on the network adjacency matrix that analytically explains the emerging Griffiths phase on networks with the quenched disorder [64, 99]. Quenched disorder, either intrinsic to nodes or topological, has been shown to smear the phase transition at critical points. A Griffiths phase may stem from a node-dependent propagation rate [94, 73], or emerge due to the quenched disorder on the edges, such as a correlated weight pattern in tree networks [102] and exponentially suppressed weight scheme in random networks [99]. The underlying mechanism is the existence of special *rare regions* (RR).

Statistically, the active state lingers in rare regions for a typical time that grows exponentially with their sizes, and eventually ends up in the absorbing state [65, 93]. When the size distribution of rare regions is exponential, it generates power-law decays with continuously varying exponents, i.e. the Griffiths phase. Not only in the spreading dynamics on networks, *rare regions* have also been shown to dramatically change the properties of classical phase transition in quenched disordered systems, such as randomly diluted Ising model or Ising model with planar defects, and quantum phase transitions in itinerant magnets with Heisenberg spin symmetry, leading to an essential singularity, the Griffiths singularity [129, 130].

Numerical studies suggest that the structural heterogeneity of finite dimensional networks may have a similar role as the quenched disorder [94, 93]. In absence of quenched disorder, the Griffiths phase can also be a consequence of structural disorder. A Griffiths phase on finite dimensional HMNs is analytically treated with the QMF approximation that originally targets systems with the quenched disorder [93].

We here briefly review the derivation of the spectral analysis on the adjacency matrix. The criterion for the localization of steady active state on networks is based on the evaluation of the inverse participation ratio (IPR) of the principle eigenvector corresponding to the largest eigenvalue. The probabilities ρ_x for each node at the steady state of Eq.(5.1) can be written as a linear superposition of the N orthogonal eigenvectors [64],

$$\rho_x = \sum_{i=1}^{N} c\left(\lambda_i^A\right) \phi_i^A. \tag{5.3}$$

If the largest eigenvalue Λ_N^A is significantly larger than all the others, the QMF approximation predicts the critical point σ_c as $1/\Lambda_N^A$, and the steady state probability as

$$\rho_x \sim c\left(\lambda_N^A\right) \phi_i^A. \tag{5.4}$$

According to the Perron-Frobenius theorem, the largest eigenvalue λ_N and the corresponding principal eigenvector ϕ_N of a real nonnegative symmetric matrix are nonnegative [91]. The order parameter $\rho(t)$ is defined as the average $\rho = \frac{1}{N} \sum_{x=1}^{N} \rho_x(t)$ over all the nodes. At the critical σ_c, the order parameter ρ at the steady state can be expanded as,

$$\rho \sim a_1 \triangle + a_2 \triangle^2 + \dots, \tag{5.5}$$

in which $\triangle = \sigma \lambda_N - 1 \ll 1$. The coefficients are given in [64] as,

$$a_i = \frac{\sum_{x=1}^{N} \phi_i^A(x)}{N \sum_{x=1}^{N} \left[\phi_i^A(x)\right]^3}. \tag{5.6}$$

With the dominant largest eigenvalue and the principle eigenvector, the order parameter ρ is approximated with $\rho \sim a_1 \triangle$. In the limit $N \to \infty$, for a localized principle eigenvector ϕ_N^A, the components $\phi_N^A(x)$ are of the order of $O(1)$ only at a few nodes, and then $a_1 \sim O(1/N)$ and $\rho \sim$

Figure 5.3: (a) IPR vs m for network configurations of HMN1 with different maximum generation g. The red squares are values of IPR for $g = 10$; the black circles are values of IPR for $g = 11$; the blue diamonds are values of IPR for $g = 12$. Each data point averages values of IPR over 100 independent realizations of HMN1 configuration. (b) the localized eigenvectors corresponding to five largest eigenvalues of the adjacency matrix of one graph realization of HMN1 configuration with $g = 11, m = 16$.

$O(1/N)$, which means the active state is localized on the a few nodes of the network. On the other hand, for a delocalized principle eigenvector ϕ_N^A, we usually have $\phi_N^A(x) \sim O(\frac{1}{\sqrt{N}})$, and then $a_1 \sim const$ and $\rho \sim const$. The active state extends over a finite fraction of nodes of the network. The localization of eigenvectors is quantified by their inverse participation ratio (IPR) [64],

$$IPR\left(\lambda_N^A\right) \quad = \quad \sum_{x=1}^{N} \left[\phi_N^A(x)\right]^4. \tag{5.7}$$

A finite IPR value of the principle eigenvector corresponds to a localized eigenvector, while a IPR approaching to zero, i.e. $O(1/N)$, corresponds to a delocalized principle eigenvector. We apply the concept of IPR on all the relevant networks to examine whether a localized principle eigenvector exists, which may suggest the emergence of rare regions and the Griffiths phase in the QMF approximation [93, 103].

As shown in Fig.(5.3a), the IPR of the principle eigenvector increases with clique size m towards to a finite value for different maximum generation g of HMN1. It suggests the principle eigenvectors for HMN1 configurations are localized. Additionally, localized eigenvectors corresponding to largest eigenvalues are also found, shown in Fig.(5.3b). For HMN2, we focus on level-dependent inter-module wiring probabilities, $p_i = 4^{-(i+1)}$ and $p_i = 4^{-i}$. The backbone as well as the first level inter-module wiring probability is fixed at $1/4$, where the modules are the basic cliques. Values of IPR are shown in Fig.(5.4a). The largest value comes from the network configuration in which the single clique contains 2
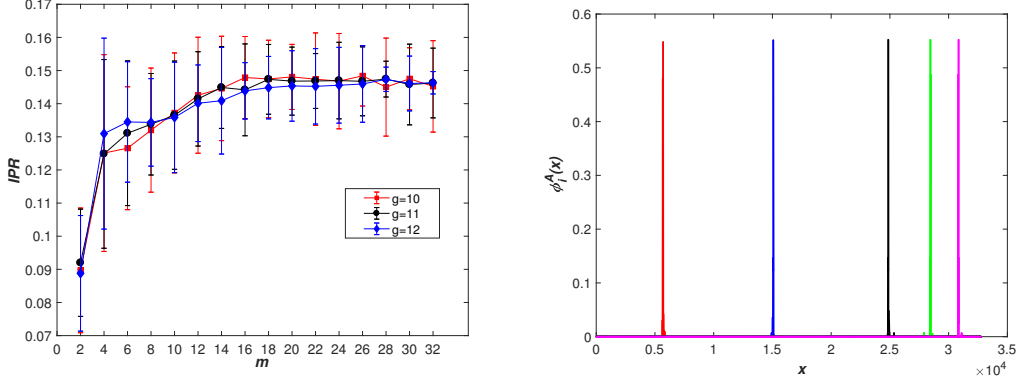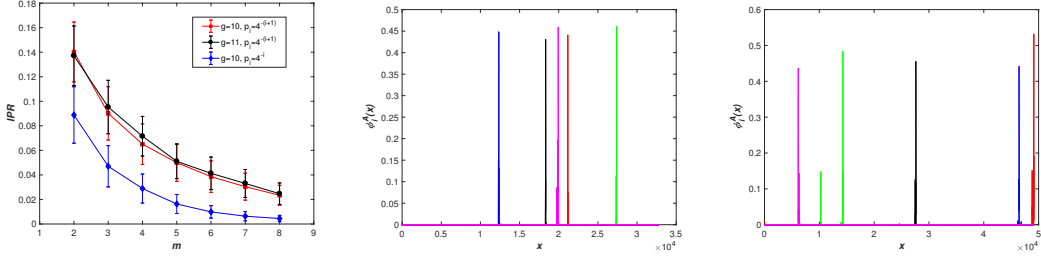
Figure 5.4: (a) IPR vs m for network configurations of HMN2 with different g. The red squares are values of the IPR with $g = 10$; the black circles are IPRs for $g = 11$. The hierarchical level-dependent inter-module probability is $p_i = 4^{-(i+1)}$. Compared to them, the blue diamonds are IPRs for $g = 10$ with a level-dependent probability $p_i = 4^{-i}$. Each data point averages IPRs over 100 independent realizations of HMN2 configuration. (b): localized eigenvectors corresponding to five largest eigenvalues of the adjacency matrix of one graph realization of HMN2 configuration with $g = 14, m = 2, p_i = 4^{-(i+1)}$; (c): localized eigenvectors corresponding to five largest eigenvalues of the adjacency matrix of one graph realization of HMN2 with $g = 14, m = 3, p_i = 4^{-(i+1)}$.

nodes, and the probability is $p_i = 4^{-(i+1)}$. In this case, the network is statistically almost fragmented. Numerical results in Sec.5.3 indeed show the emergence of the Griffiths phase as a trivial consequence of the network disconnectedness. To examine the Griffiths phase on a connected network with a finite fractal dimension, the network configuration of $m = 3$ and $p_i = 4^{-(i+1)}$ is also chosen for the numerical simulation. For stochastically constructed HMN2, as the clique size m or level-dependent probability increases while keeping the other factor fixed, modules becomes more and more connected with other modules in the same level, and the value of IPR decreases, shown in Fig.(5.4a). The regime over the parameter m and the level-dependent p_i that possibly supports the Griffiths phase is narrow. It is not surprising to see that the localized principle eigenvector exists for network configurations of HMN2 with a finite value of IPR. In Fig.(5.4b) and Fig.(5.4c), we illustrate the localized eigenvectors corresponding to large eigenvalues in two network configurations.

5.2.2 Spectral Analysis on the Laplacian Matrix

The spectral analysis on the network Laplacian provides another approach to predict the Griffiths phase, which is confirmed in [93, 100]. Here, we review how the Lifshitz tail suggests the Griffiths phase according to the calculation in [100]. Near the critical point, in the inactive phase, the evolution equation of the SIS model Eq.(5.1) can be approximated as

$$\frac{d}{dt}\rho_x(t) \;\; = \;\; -\rho_x(t) + \sigma \sum_{y=1}^{N} A_{xy}\rho_y(t), \tag{5.8}$$

which can be rewritten using the Laplacian form in Eq.(5.2) as

$$\frac{d}{dt}\rho_x(t) = \left(\sigma\delta_{xy}\sum_{z=1}^{N}A_{yz} - 1\right)\rho_x(t) - \sigma\sum_{y=1}^{N}L_{xy}\rho_y(t).$$
(5.9)

A linear stability analysis can be performed similar to the synchronization process [16]. The normal modes of the perturbations above the absorbing state can be written,

$$\frac{d}{dt}\rho_x(t) = -\sigma\sum_{y}L_{xy}\rho_y(t),$$
(5.10)

in which the spontaneous decaying rate is changed from 1 in Eq.(5.8) to σL_{xx}. This change may shift σ_c. In the inactive phase, it is not expected to introduce relevant rare region effects. Using the Laplacian spectrum, $\rho_x(t)$ can be expressed as the expansion with the Laplacian eigenvalues and eigenvectors,

$$\rho_x(t) = \sum_{iy}e^{-\sigma\lambda_i^L t}\phi_i^L(x)\phi_i^L(x)\rho_y(0),$$
(5.11)

and the total density is determined by the lowest eigenvalues of the spectrum,

$$\rho(t) \sim \sum_{i=2}^{N}e^{-\sigma\lambda_i^L t}.$$
(5.12)

In the continuum limit,

$$\rho(t) \sim \int_{\lambda_2^L}^{\lambda_c^L}d\lambda P(\lambda)e^{-\sigma\lambda t},$$
(5.13)

in which λ_c^L is the experimentally determined end of tail value. A power-law distribution $P(\lambda)$ of the lower edge of the Laplacian spectrum suggests the Griffiths phase behavior above the absorbing state,

$$\rho(t) \sim \int_{\lambda_2}^{\lambda_c}d\lambda\lambda^a e^{-\sigma\lambda t},$$
(5.14)

$$\sim t^{-\sigma(a+1)}.$$
(5.15)

For comparison I calculated the Lifshitz tails for HMN1 and HMN2, shown in Fig.(5.5). In the plot, the probability distribution $P(\lambda)$ is calculated with the bin size $\delta\lambda = 0.0001$ over 100 independent graph realizations. The Lifshitz tail for HMN2 configuration with $g = 13, m = 2, p_i = 4^{-(i+1)}$, and
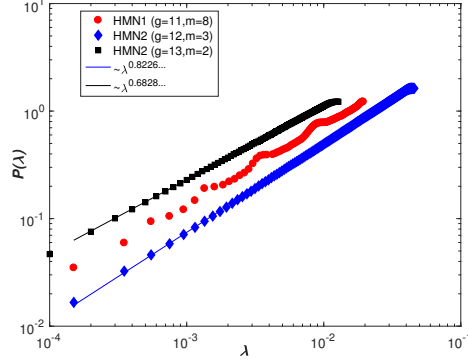
Figure 5.5:   Lifshitz tails for HMN1 and HMN2: The red circles are tail distribution for HMN1 configuration with $g = 11, m = 8$; the black squares are tail distribution for HMN2 configuration with $g = 13, m = 2, p_i = 4^{-(i+1)}$, fitted with a power law $P(\lambda) \sim \lambda^{0.683}$; the blue diamonds are tail distribution for HMN2 configuration with $g = 12, m = 3, p_i = 4^{-(i+1)}$, fitted with $P(\lambda) \sim \lambda^{0.823}$.

with $g = 12, m = 3, p_i = 4^{-(i+1)}$, are fitted with power laws as,

$$P(\lambda) \sim \lambda^{0.683}, \tag{5.16}$$

and

$$P(\lambda) \sim \lambda^{0.823}, \tag{5.17}$$

while the Lifshitz tail for HMN1 slightly deviates from a power law, suggesting the lack of the Griffiths phase.

5.3   Simulation Results

We present here results from numerical study of the SIS model on all the network configurations of HMN1 and HMN2. The network is initialized as a fully-active graph. The system is updated each step until the maximum time $t_{max}\left(10^6\right)$ is reached or in case of activity extinction. Simulations for each propagation rate σ are repeated on $1000 \sim 5000$ independent network realizations. The order parameter $\rho(t)$ for each σ is the average of all the runs. We also derive the effective decay exponent by fitting critical power laws $\rho(t) \sim t^{-\alpha_{eff}}$ with the efficient exponent defined as [99, 103],
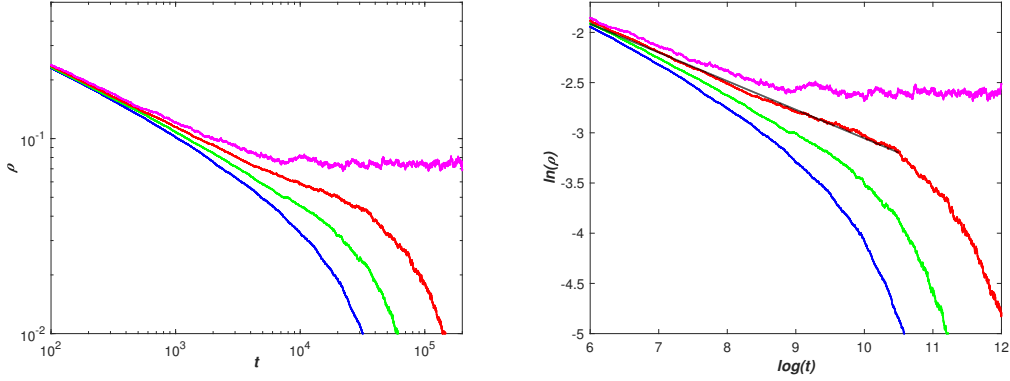
Figure 5.6: (a): ρ vs t for network configuration of HMN1 with $g = 11, m = 8$. Lines from bottom to top are for $\lambda = 0.1650, 0.1651, 0.1652, 0.1653$. (b): $\log(\rho)$ versus $\log(t)$, the black straight line is the fitted curve with $\rho \sim t^{-0.285}$. The critical propagation rate is $\lambda_c \approx 0.1652$
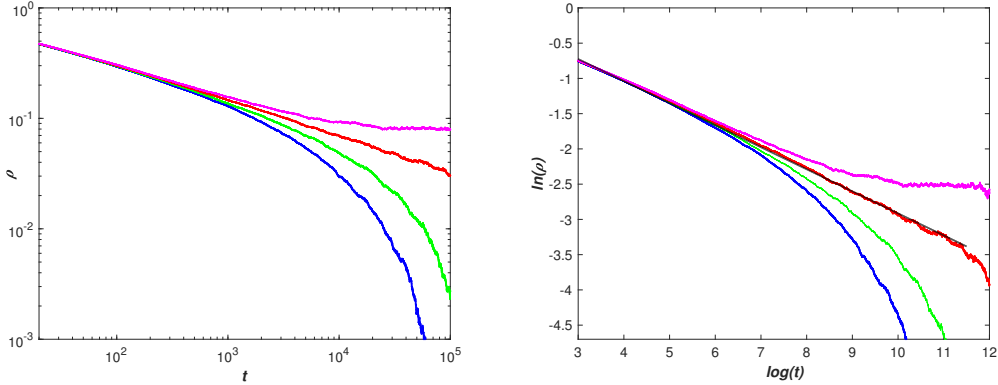
Figure 5.7: (a): ρ vs t for network configuration of HMN1 with $g = 11, m = 16$. Lines from bottom to top are for $\sigma = 0.07475, 0.07480, 0.07485, 0.0749$. (b): $\log(\rho)$ versus $\log(t)$, the black straight line is the fitted curve with $\rho \sim t^{-0.313}$. The critical propagation rate is $\sigma_c \approx 0.07485$.

$$\alpha_{eff} = -\frac{\ln\left[\rho(t)/\rho\left(t'\right)\right]}{\ln(t/t')}, \tag{5.18}$$

where t and t' are chosen such a way that the discrete approximate of the derivative is sufficiently smooth.

Fig.(5.6) and Fig.(5.7) present the simulation results for network configurations of HMN1 with $g = 11, m = 8$ and $g = 11, m = 16$, and fit with the effective decay exponent at the critical point. It shows that the Griffiths phase is absent in HMN1, and we see a trivial phase transition at a single critical point. For network configuration of HMN2 with $m = 2$ and $p_i = 4^{-(i+1)}$, the size-independent
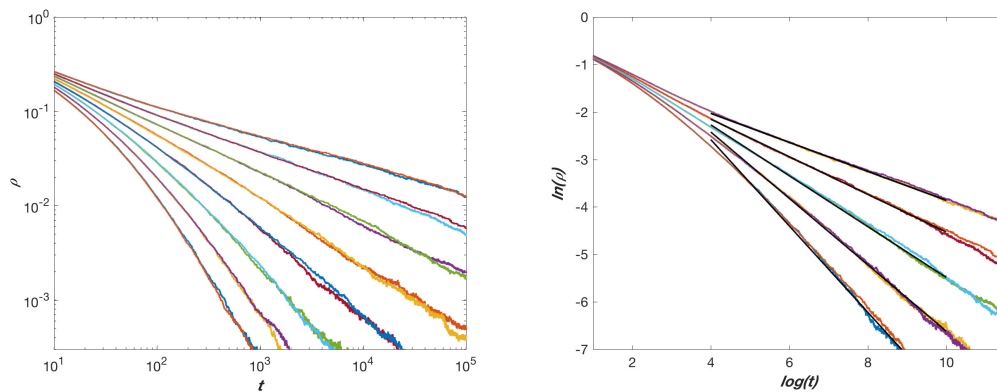
Figure 5.8: (a): ρ vs t for network configurations of HMN2 with $g = 13, m = 2$ and with $g = 14, m = 2$. Lines from bottom to top are for $\sigma = 0.46, 0.47, 0.48, 0.49, 0.50, 0.51, 0.52, 0.53$. (b): $\log(\rho)$ versus $\log(t)$, the black straight lines are the fitted curves with $\rho \sim t^{-0.909}$, $\rho \sim t^{-0.699}$, $\rho \sim t^{-0.536}$, $\rho \sim t^{-0.396}$ and $\rho \sim t^{-0.305}$ from bottom to top for $\sigma = 0.49, 0.50, 0.51, 0.52, 0.53$
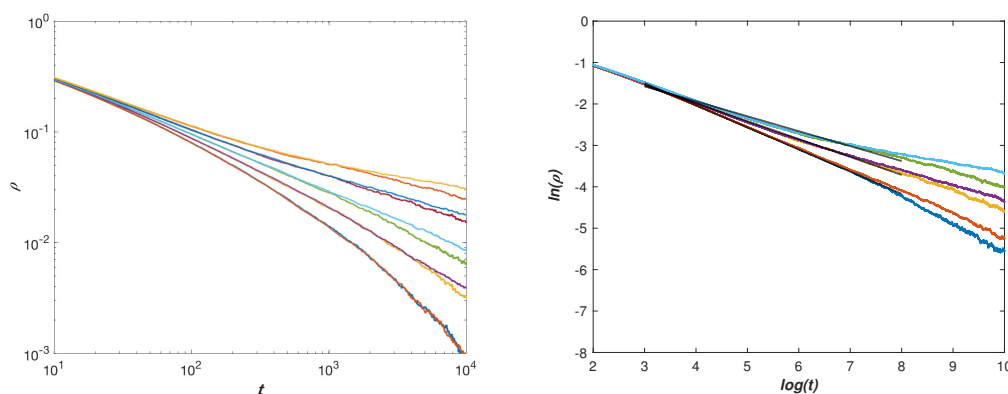
Figure 5.9: (a): ρ vs t for network configurations of HMN2 with $g = 13, m = 3$ and with $g = 12, m = 3$. Lines from bottom to top are for propagation rates $\sigma = 0.258, 0.259, 0.260, 0.261, 0.262$. (b): $\log(\rho)$ versus $\log(t)$, the black straight lines from bottom to top are the fitted curves with $\rho \sim t^{-0.534}$, $\rho \sim t^{-0.433}$, $\rho \sim t^{-0.361}$ for $\sigma = 0.260, 0.261, 0.262$

Griffiths phase emerges, shown in Fig.(5.8). However, the Griffiths phase is a trivial consequence of the disconnectedness of HMN2. For network configurations of HMN2 that is connected, I choose the case of $m = 3, p_i = 4^{-(i+1)}$ at which the corresponding value of IPR is sufficiently large. Since inter-module connections are established stochastically, there is a chance that all the possible inter-module edges fails to be connected. To avoid this case, at least one inter-module connection is enforced to exist by repeating the construction of graphs in the simulation. Numerical results for a connected HMN2 is presented in Fig.(5.9). We see a nearly size-independent power laws in a stretched regime of σ. Comparing Fig.(5.8) with Fig.(5.9), as m increases while keeping p_i fixed and *vice versa*, the regime in the parameter space of λ for the Griffiths phase is expected to become narrow until it disappears when HMN2 becomes highly connected.

One significant advantage of biological systems operating at criticality is the diverging reaction to highly diverse stimuli. From the perspective of statistical mechanics, this is caused by the divergence of susceptibility at criticality. To measure the divergence of response in the Griffiths phase, we use the concept of dynamic susceptibility that is applied to gauge the overall response to a continuous localized stimulus in [93]. This dynamic susceptibility is defined as,

$$\Sigma\left(\sigma\right) \;\; = N\left[\rho_f\left(\sigma\right) - \rho_s\left(\sigma\right)\right], \tag{5.19}$$

where $\rho_s\left(\sigma\right)$ is the stationary density in the absence of stimuli and $\rho_f\left(\sigma\right)$ is the steady-state density reached when one single node is constrained to remain active. As shown in Fig.(5.10), Σ becomes large in the region of the Griffiths phase, and more importantly it grows with the network size N that implies a divergent response over an extended region.

The results suggest the importance of level dependent inter-module wiring probability on the emergence of the Griffiths phase. HMN1 network configurations are not able to support the Griffiths phase, although they satisfy the structural criteria, such as the finite fractal dimension, the modular structure, the hierarchical heterogeneity. HMN2 network configurations are constructed to possess a hierarchical pattern in the inter-module wiring probabilities, which therefore require a delicate tuning to maintain a connected, finite dimensional network. The hierarchical pattern of inter-module connections results in more heterogeneous networks of HMN2, while network configurations of HMN1 are more homogenous. This can be shown by considering the Lifshitz tails for HMN1 and HMN2 in Fig.(5.5). The Lifshitz tail of HMN1 deviates from that of HMN2, and compared to HMN2, the spectrum of HMN1 is closer to the original network HN3 [34]. Although HN3 possesses a hierarchical structure, it is not sufficiently
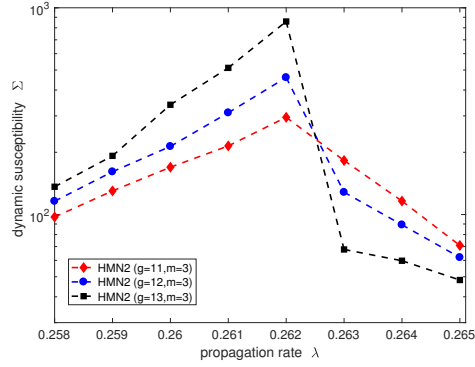
Figure 5.10: : Dynamic susceptibility Σ, measured for network configurations of HMN2 with $g = 11, m = 3$ (red diamonds), $g = 12, m = 3$ (blue circles) and $g = 13, m = 3$ (black squares) with the $p_i = 4^{-(i+1)}$. The overall response increases significantly near and in the Griffiths phase (from $\sigma = 0.260$ to $\sigma = 0.262$), and decreases away from the critical region.

disordered to induce the Griffiths phase. The difference between hierarchical patterns of HMN1 and HMN2 significantly affects the phase transition and existence of the Griffiths phase.

The spectral analysis suggests that a finite IPR of the principle eigenvector of the adjacency matrix can be considered to indicate the localization of activity that may result in the emergence of rare regions and the Griffiths phase under certain circumstances. Although all the network configurations of HMN1 prove to have a finite IPR and localized eigenvectors corresponding to the largest eigenvalues, only when the structural disorder of inter-module connections is sufficient as in HMN2, the Griffiths phase appears. As a counter example to previous finite dimensional models with localized principle eigenvectors that support the Griffiths phase [93, 103], a class of finite dimensional networks with a localized principle eigenvector is found where the Griffiths phase is absent. This observation has been previously reported in highly-connected networks with intrinsic weight disorder or finite-size random networks with power-law degree distributions [103, 48]. This raises questions on a more generalized theoretical analysis on the network adjacency matrix that applies to all the networks considered previously and currently. Besides the spectral analysis on the adjacency matrix, the Lifshitz tail of Laplacian spectrum presents a power law probability distribution at the lower edge of spectrum of HMN2 networks, while the tail distribution in HMN1 deviates from a power law. Numerical results confirm the property of phase transition may be related to this difference between Lifshitz tails of HMN1 and HMN2.

Chapter 6

Conclusion

In this thesis, we discuss hierarchical networks that possess the self-similar, fractal feature. These networks are constructed in an iterative fashion, which are therefore also defined as fractals. In each step, individual edges are replaced by a pre-defined graph-let, forming the next generation. Rich dynamics arises on fractal networks, of which we particular study synchronization, continuous and discrete time quantum walk, and the epidemic spreading. Due to the self-similar nature, the RG techniques lend themselves to study of properties of systems at large time and spatial scale.

RG is applied to hierarchical networks to obtain spectral properties of the network Laplacian matrix. We calculate the spectral dimension d_s that describes the scaling of smallest eigenvalues of the network Laplacian matrix, shown in Eq.(2.29), and evaluate the determinant and zeta function of the Laplacian in Eq.(2.31), and even single eigenvalues using the power method explained in Sec.7.2. Due to the relation between the Laplacian determinant and the graph complexity as in Eq.(2.6), we measure the graph complexity, i.e. enumeration of spanning trees, in large limit of the network size N. Conclusions suggest on fractal networks we study, Hanoi networks and hierarchical lattices, the number of spanning trees exponentially increases as N in Eq.(2.20) and Eq.(2.23). Furthermore, the network synchronizability can be estimated through the evaluation on individual Laplacian eigenvalues. In summary, in addition to geometric characteristics, such as the degree distribution, clustering coefficients and shortest path lengths, RG provides a framework to study the network topology via their spectral properties.

We also explore the quantum processes, i.e. the discrete and continuous time quantum walk, on hierarchical networks, and apply RG to describe the scaling behavior at large time and spatial

scales. In DTQW, we treat the system of stochastic master equations on the Laplace transform of site amplitudes and evaluate the singularities of hopping parameters and site amplitudes. Under rescaling the system length, $L' = 2L$, characteristic times rescale as $t' = 2^{d_w^{QW}} t$ with the exact walk exponent d_w^{QW}. Based on studies on specific networks, we analytically conjecture a general relation between the d_w^{RW} of discrete-time random walks and d_w^{QW} of quantum walks with the Grover coin. In each hierarchical network, i.e. MK3, MK4 and DSG, we find that d_w^{QW} is exactly half the value for the classical random walk on the same network. Such a relation holds for regular lattices, and it also holds for networks without translational invariance. RG proves to be a complementary approach to extensive numerical simulation for the asymptotic of quantum walks.

We further consider the quantum search problem with a continuous time quantum walk on hierarchical networks of finite spectral dimension d_s of the network Laplacian. For networks of fractal dimension d_f, for which in general $d_f \neq d_s$, it suggests that d_s is the scaling exponent that determines the computational complexity of the search. Our results are consistent with those of lattices of integer dimension, where $d = d_f = d_s$, and complement the recent discussion on random networks showing that for all random networks with $p \geq (\ln N)^{3/2}/N$, i.e. $d_s \to \infty$, the spatial search by quantum walk is optimal. For fractal networks, we find that the Grover limit of quantum search can be obtained whenever $d_s > 4$.

Hierarchical networks exhibit novel behaviors in various self-organizing processes, such as synchronization and epidemic spreading, which are extensively studied in in real complex systems especially the biological systems. We study the Griffiths phase using the SIS model in hierarchical modular networks that capture the system-level organization of brain components. The idea of a Griffiths phase is used to explain the stretched critical region for optimal functioning of brain networks, with a single critical point extended to a region in the Griffiths phase. This provides an alternative self-organization mechanism. This phase stems from the intrinsic structural heterogeneity of brain networks, particularly the hierarchical modular structure in this case. We extend this concept to modified hierarchical networks with small-world edges based on Hanoi networks. Through extensive simulations, the hierarchical level-dependent inter-module wiring probabilities are identified to determine the emergence of the Griffiths phase. Numerical results and the complementary spectral analysis of the relevant networks can be helpful for a deeper understanding of the essential structural characteristics of finite-dimensional networks to support the Griffiths phase.

Through this thesis, we present dynamical processes on self-similar hierarchical structures and

the application of renormalization group that provides the exact analytical treatment to topological properties and asymptotic dynamical behaviors. For exploration of novel phenomena, these fractal networks, due to their special structure, emerge as alternative choices to homogenous lattices, random networks and scale-free networks.

Chapter 7

Appendix

This Appendix provides details on applying RG to calculate the determinant and largest eigenvalue of the Laplacian. In Sec.7.1, we first present to procedure that derives the recursions of a set of parameters $(p, q, l, \ldots)$ for Hanoi networks and hierarchical lattices, and and apply these recursions to evaluate the spectral properties. In Sec.7.2, we apply RG to the power method that calculates the largest eigenvalue λ_N.

7.1 RG for the Laplacian determinant

In this section, we derive the recursions in Hanoi Networks and hierarchical lattices. Following the procedure as discussed on HN3 and HN5 (see Sec.2.2.1), we evaluate the Laplacian determinant using recursive equations on HNNP, HN6 and hierarchical lattices.

7.1.1 RG for Spectra of HN3 and HN5

We evaluate general $2^g \times 2^g$-determinant for the matrix L_g that is used in the analysis of Hanoi networks. Instead of providing a formal description of L_g for general size g, we simply illustrate its generic recursive pattern for HN3 and HN5 with $g = 4$:

$$L_{g=4}^{(3,5)} = \begin{bmatrix}
q_4 & -p_0 & -l_1 & 0 & -l_2 & 0 & 0 & 0 & -2l_3 & 0 & 0 & 0 & -l_2 & 0 & -l_1 & -p_0 \\
-p_0 & q_1 & -p_0 & -p_1 & 0 & 0 & 0 & 0 & 0 & 0 & 0 & 0 & 0 & 0 & 0 & 0 \\
-l_1 & -p_0 & q_2 & -p_0 & -l_1 & 0 & -p_2 & 0 & 0 & 0 & 0 & 0 & 0 & 0 & 0 & 0 \\
0 & -p_1 & -p_0 & q_1 & -p_0 & 0 & 0 & 0 & 0 & 0 & 0 & 0 & 0 & 0 & 0 & 0 \\
-l_2 & 0 & -l_1 & -p_0 & q_3 & -p_0 & -l_1 & 0 & -l_2 & 0 & 0 & 0 & -p_3 & 0 & 0 & 0 \\
0 & 0 & 0 & 0 & -p_0 & q_1 & -p_0 & -p_1 & 0 & 0 & 0 & 0 & 0 & 0 & 0 & 0 \\
0 & 0 & -p_2 & 0 & -l_1 & -p_0 & q_2 & -p_0 & -l_1 & 0 & 0 & 0 & 0 & 0 & 0 & 0 \\
0 & 0 & 0 & 0 & 0 & -p_1 & -p_0 & q_1 & -p_0 & 0 & 0 & 0 & 0 & 0 & 0 & 0 \\
-2l_3 & 0 & 0 & 0 & -l_2 & 0 & -l_1 & -p_0 & q_4 & -p_0 & -l_1 & 0 & -l_2 & 0 & 0 & 0 \\
0 & 0 & 0 & 0 & 0 & 0 & 0 & 0 & -p_0 & q_1 & -p_0 & -p_1 & 0 & 0 & 0 & 0 \\
0 & 0 & 0 & 0 & 0 & 0 & 0 & 0 & -l_1 & -p_0 & q_2 & -p_0 & -l_1 & 0 & -p_2 & 0 \\
0 & 0 & 0 & 0 & 0 & 0 & 0 & 0 & 0 & -p_1 & -p_0 & q_1 & -p_0 & 0 & 0 & 0 \\
-l_2 & 0 & 0 & 0 & -p_3 & 0 & 0 & 0 & -l_2 & 0 & -l_1 & -p_0 & q_3 & -p_0 & -l_1 & 0 \\
0 & 0 & 0 & 0 & 0 & 0 & 0 & 0 & 0 & 0 & 0 & 0 & -p_0 & q_1 & -p_0 & -p_1 \\
-l_1 & 0 & 0 & 0 & 0 & 0 & 0 & 0 & 0 & -p_2 & 0 & -l_1 & -p_0 & q_2 & -p_0 \\
-p_0 & 0 & 0 & 0 & 0 & 0 & 0 & 0 & 0 & 0 & 0 & 0 & 0 & -p_1 & -p_0 & q_1
\end{bmatrix}$$

(7.1)

The bare parameters q_i on the diagonal refer to on-site factors of each node x that belongs to the i-th hierarchy as determined by Eq.(2.1). For the Laplacian, q_i is simply the node degree. The off-diagonal parameters label already existing or potentially emerging links between nodes. To keep parameters fundamentally non-negative, we insert negative signs explicitly. While the p_i correspond to the solid black lines in Fig.(2.1), the parameters l_i refer to those long-range links shaded in green in Fig.(2.1). Although all l_i are originally zero for HN3, we still need to consider them, as they emerge as a relevant parameter during RG. We have imposed periodic boundary conditions by identifying node $N = 2^g$

with site $n = 0$. We can write Eq.(2.8) as

$$
\begin{aligned}
\left[\det L_g^{(3,5)}\right]^{-\frac{1}{2}} &= C_g \iint\limits_{-\infty}^{\infty} \frac{dx_0 dx_{2g-1}}{\pi} \exp\left\{-q_g\left(x_0^2 + x_{2g-1}^2\right) + 4l_{g-1}x_0 x_{2g-1}\right\} \\
&\quad \int\limits_{-\infty}^{\infty} \cdots \int \left(\prod_{i=1}^{g-1}\prod_{j=1}^{2^{g-i}} \frac{dx_{2^{i-1}(2j-1)}}{\sqrt{\pi}}\right) \\
&\quad \exp\left\{-\sum_{i=1}^{g-1} q_i \sum_{j=1}^{2^{g-i}} x_{2^{i-1}(2j-1)}^2 + 2\sum_{i=1}^{g-2} l_i \sum_{j=1}^{2^{g-i}} x_{2^{i-1}(2j-2)} x_{2^{i-1}(2j)} \right. \\
&\quad \left. + 2\sum_{i=1}^{g-1} p_i \sum_{j=1}^{2^{g-i-1}} x_{2^{i-1}(4j-3)} x_{2^{i-1}(4j-1)} + 2p_0 \sum_{j=1}^{2^{g-1}} x_{2j-1}\left(x_{2j-2} + x_{2j}\right)\right\}.
\end{aligned}
\tag{7.2}
$$

The factor C_g, initially unity, captures the contribution of integrals from any prior RG-step.

To solve $\det L_g^{(3,5)}$ recursively, we integrate only over all variables x of odd index i.e. those with $i = 1$. We focus on the case $i = 1$ in Eq.(7.2) and re-write $\prod_{j=1}^{2^{g-i}} dx_{2^{i-1}(2j-1)}\Big|_{i=1} = \prod_{j=1}^{2^{g-1}} dx_{2j-1} = \prod_{j=1}^{2^{g-2}} dx_{4j-3} dx_{4j-1}$ to get:

$$
\begin{aligned}
&\prod_{j=1}^{2^{g-2}} \iint\limits_{-\infty}^{\infty} \frac{dx_{4j-3} dx_{4j-1}}{\pi} \exp\left\{-q_1\left(x_{4j-3}^2 + x_{4j-1}^2\right) + 2p_1 x_{4j-3} x_{4j-1} \right. \\
&\qquad\qquad\qquad \left. + 2p_0\left[x_{4j-3}\left(x_{4j-4} + x_{4j-2}\right) + x_{4j-1}\left(x_{4j-2} + x_{4j}\right)\right]\right\}, \\
&= \prod_{j=1}^{2^{g-2}} \left(q_1^2 - p_1^2\right)^{-\frac{1}{2}} \exp\left\{\frac{q_1 p_0^2}{q_1^2 - p_1^2}\left[\left(x_{4j-4} + x_{4j-2}\right)^2 + \left(x_{4j-2} + x_{4j}\right)^2\right]\right. \\
&\qquad\qquad\qquad \left. + \frac{2p_1 p_0^2}{q_1^2 - p_1^2}\left(x_{4j-4} + x_{4j-2}\right)\left(x_{4j-2} + x_{4j}\right)\right\}, \\
&= \left(q_1^2 - p_1^2\right)^{-2^{g-3}} \exp\left\{\frac{2q_1 p_0^2}{q_1^2 - p_1^2}\left(x_0^2 + x_{2^{k-1}}^2\right) + \frac{2q_1 p_0^2}{q_1^2 - p_1^2}\sum_{i=2}^{g-2}\sum_{j=1}^{2^{g-i-1}} x_{2^{i-1}(2j-1)2}^2 \right. \\
&\qquad\qquad\qquad \left. + \frac{2p_0^2}{q_1 - p_1}\sum_{j=1}^{2^{g-2}} x_{(2j-1)2}^2 + \frac{2p_0^2}{q_1 - p_1}\sum_{j=1}^{2^{g-1}} x_{2j-2} x_{2j} + \frac{2p_1 p_0^2}{q_1^2 - p_1^2}\sum_{j=1}^{2^{g-2}} x_{(2j-2)2} x_{(2j)2}\right\}.
\end{aligned}
\tag{7.3}
$$

With that result, the remaining integral over the even-indexed variables can be written as

$$
\left[\det L_g^{(3,5)}\right]^{-\frac{1}{2}} \;=\; C_g \left(q_1^2 - p_1^2\right)^{-2^{g-3}} \iint\limits_{-\infty}^{\infty} \frac{dx_0 dx_{2^g-1}}{\pi}
$$

$$
\exp\left\{-\left[q_g - \frac{2q_1 p_0^2}{q_1^2 - p_1^2}\right]\left(x_0^2 + x_{2^g-1}^2\right) + 4l_{g-1} x_0 x_{2^g-1}\right\}
$$

$$
\int\limits_{-\infty}^{\infty}\!\!\cdots\!\!\int \left(\prod_{i=1}^{g-2} \prod_{j=1}^{2^{g-1-i}} \frac{dx_{2^i(2j-1)}}{\sqrt{\pi}}\right)
$$

$$
\exp\left\{-\sum_{i=2}^{g-2}\left[q_{i+1} - \frac{2q_1 p_0^2}{q_1^2 - p_1^2}\right]\sum_{j=1}^{2^{g-1-i}} x_{2^i(2j-1)}^2 - \left[q_2 - \frac{2p_0^2}{q_1 - p_1}\right]\sum_{j=1}^{2^{g-2}} x_{2(2j-1)}^2 \right.
$$

$$
+2\sum_{i=1}^{g-2} p_{i+1} \sum_{j=1}^{2^{g-i-2}} x_{2^i(4j-3)} x_{2^i(4j-1)} \tag{7.4}
$$

$$
+2\sum_{i=2}^{g-3} l_{i+1} \sum_{j=1}^{2^{g-i-1}} x_{2^i(2j-2)} x_{2^i(2j)} + 2\left(l_2 + \frac{p_1 p_0^2}{q_1^2 - p_1^2}\right)\sum_{j=1}^{2^{g-2}} x_{2(2j-2)} x_{2(2j)}
$$

$$
\left. +2\left(l_1 + \frac{p_0^2}{q_1 - p_1}\right)\sum_{j=1}^{2^{g-2}} x_{2(2j-1)}\left(x_{2(2j-2)} + x_{2(2j)}\right)\right\}.
$$

Substituting $x_i' = x_{2i}$, this expression is identical in form with Eq.(7.2), and we can identify

$$
\begin{aligned}
q_1' &= q_2 - 2\frac{p_0^2}{q_1 - p_1}, \\
q_i' &= q_{i+1} - 2\frac{q_1 p_0^2}{q_1^2 - p_1^2}, \qquad (i \geq 2), \\
p_0' &= l_1 + \frac{p_0^2}{q_1 - p_1}, \\
p_i' &= p_{i+1}, \qquad (i \geq 1), \\
l_1' &= l_2 + \frac{p_1 p_0^2}{q_1^2 - p_1^2}, \\
l_i' &= l_{i+1}, \qquad (i \geq 2),
\end{aligned}
\tag{7.5}
$$

The difference between the primed and unprimed quantities represents the step from the μ-th to the $\mu+1$-st level in the RG recursion, with $0 \leq \mu < g$. The recursion for the overall scale-factor C_g is

$$
C_g' = C_g \left(q_1^2 - p_1^2\right)^{-2^{g-\mu-3}}. \tag{7.6}
$$

Initial conditions for recursions in Eq.(7.5) and Eq.(7.6) are:

$$
\begin{aligned}
C_g^{(0)} &= 1, \\
q_i^{(0)} &= 3 + \epsilon \quad (i \geqslant 1), \\
p_i^{(0)} &= 1 \quad (i \geqslant 0), \\
l_i^{(0)} &= 0 \quad (i \geqslant 1),
\end{aligned}
\tag{7.7}
$$

reflecting the fact that all the nodes in HN3 have a constant degree $k_i = 3$. Since all the diagonal entries are identical, the hierarchy for the q_i collapses and we obtain only two nontrivial relations, one for q_1 and one for all other $q_i \equiv q_2$ for all $i \geq 2$. Here, all p_i are non-zero, encompassing the backbone links ($i = 0$) and long-range links ($i \geq 1$). But it remains $p_i \equiv 1$ for $i \geq 1$ at any step μ of the RG, in particular, $p_1^{(\mu)} \equiv 1$ throughout; only the backbone p_0 renormalizes nontrivially. Although all the links of type l_i are absent in this network, the details of the calculation show that under renormalization terms of type l_1 emerge while those for l_i for $i \geq 2$ remain zero at any step. Thus, Eq.(7.5-7.6) reduce to RG recursion equations:

$$
\begin{aligned}
C_g^{(\mu+1)} &= C_g^{(\mu)} \left\{ \left[q_1^{(\mu)} \right]^2 - 1 \right\}^{-2^{k-3-\mu}}, \\
q_1^{(\mu+1)} &= q_2^{(\mu)} - 2 \frac{\left[p_0^{(\mu)} \right]^2}{q_1^{(\mu)} - 1}, \\
q_2^{(\mu+1)} &= q_2^{(\mu)} - 2 \frac{q_1^{(\mu)} \left[p_0^{(\mu)} \right]^2}{\left[q_1^{(\mu)} \right]^2 - 1}, \\
p_0^{(\mu+1)} &= l_1^{(\mu)} + \frac{\left[p_0^{(\mu)} \right]^2}{q_1^{(\mu)} - 1}, \\
l_1^{(\mu+1)} &= \frac{\left[p_0^{(\mu)} \right]^2}{\left[q_1^{(\mu)} \right]^2 - 1}.
\end{aligned}
\tag{7.8}
$$

We can further eliminate q_2 from Eqs.(7.8) by noting that these equations possess an invariant:

$$
q_2^{(\mu)} = q_1^{(\mu)} + 2 l_1^{(\mu)} \quad (0 \leqslant \mu < k).
\tag{7.9}
$$

Then, abbreviating $q_\mu \equiv q_1^{(\mu)}$, $p_\mu \equiv p_0^{(\mu)}$, and $l_\mu = l_1^{(\mu)}$, Eq.(7.8) reduces to

$$
\begin{aligned}
q_{\mu+1} &= q_\mu + 2l_\mu - 2\frac{p_\mu^2}{q_\mu - 1} \quad (q_0 = 3 - \lambda), \\
p_{\mu+1} &= l_\mu + \frac{p_\mu^2}{q_\mu - 1} \quad (p_0 = 1), \\
l_{\mu+1} &= \frac{p_\mu^2}{q_\mu^2 - 1} \quad (l_0 = 0).
\end{aligned}
\tag{7.10}
$$

HN5 contains HN3 but possesses many additional links between sites, see Fig.(2.1). In HN5, the initial conditions for recursions in Eq.(7.5) and Eq.(7.6) are

$$
\begin{aligned}
C_g^{(0)} &= 1, \\
q_i^{(0)} &= 2i + 1 + \epsilon \quad (i \geqslant 1), \\
p_i^{(0)} &= 1 \quad (i \geqslant 0), \\
l_i^{(0)} &= 1 \quad (i \geqslant 1),
\end{aligned}
\tag{7.11}
$$

reflecting the fact that all sites in HN5 have a hierarchy-dependent, increasing degree of $k_i = 2i + 1$ with average 5. Now, diagonal entries are no longer identical and we have to modify the equations for the q_i when compared to HN3. Yet, the difference between q_i and q_{i+1} is constant throughout, $q_{i+1} - q_i = 2$, and taking that modification into account, only the renormalization of q_1 and q_2 evolves nontrivially, as before for HN3. Again, all p_i are non-zero, encompassing the backbone links ($i = 0$) and all levels of long-range links ($i \geq 1$). But it remains $p_i \equiv 1$ for $i \geq 1$ at any step μ of the RG-flow, in particular, $p_1^{(\mu)} \equiv 1$ throughout; only the backbone p_0 renormalizes nontrivially. Special to HN5, all links of type l_i are already present initially in this network. Though, only l_1 renormalizes, as in HN3, whereas it is $l_i \equiv 1$ for all $i \geq 2$. Thus, we obtain just slightly more elaborate RG recursion equations which merely differ in the last relation from Eq.(7.8):

$$
l_1^{(\mu+1)} = 1 + \frac{\left[p_0^{(\mu)}\right]^2}{\left[q_1^{(\mu)}\right]^2 - 1}.
\tag{7.12}
$$

The formal solution for $C_g^{(\mu)}$ is unchanged from HN3, given in Eq. (2.11). Furthermore, we note that, despite the changes to the recursions for q_2 and l_1, the invariant in Eq. (7.9) *remains* valid, allowing

the elimination of the recursion for $q_2^{(\mu)}$ for $\mu < k - 2$. Then, abbreviating again $q_\mu = q_1^{(\mu)}$, $p_\mu = p_0^{(\mu)}$, and $l_\mu = l_1^{(\mu)}$ reduces the RG-recursions to

$$
\begin{aligned}
q_{\mu+1} &= q_\mu + 2l_\mu - 2\frac{p_\mu^2}{q_\mu - 1} & (q_0 = 3 - \lambda), \\
p_{\mu+1} &= l_\mu + \frac{p_\mu^2}{q_\mu - 1} & (p_0 = 1), \\
l_{\mu+1} &= 1 + \frac{p_\mu^2}{q_\mu^2 - 1} & (l_0 = 1).
\end{aligned}
\tag{7.13}
$$

The procedure to obtain the spectral properties through Eq.(7.10) and Eq.(7.13) has been explained in Sec.2.2.1.

7.1.2   RG for Spectra of HNNP and HN6

Now, we evaluate the most general $2^g \times 2^g$-determinant for the matrix $L_g^{(NP,6)}$ representing HNNP and HN6. Again, we simply provide a description of $L_g^{(NP,6)}$ for the case $g = 4$:

$$L_g^{(NP,6)} = \begin{bmatrix}
q_4 & -p_0 & -l_1 & -p_1 & -l_2 & 0 & -p_2 & 0 & -2l_3 & 0 & -p_2 & 0 & -l_2 & -p_1 & -l_1 & -p_0 \\
-p_0 & q_1 & -p_0 & 0 & -p_1 & 0 & 0 & 0 & 0 & 0 & 0 & 0 & 0 & 0 & 0 & 0 \\
-l_1 & -p_0 & q_2 & -p_0 & -l_1 & 0 & 0 & 0 & -p_2 & 0 & 0 & 0 & 0 & 0 & 0 & 0 \\
-p_1 & 0 & -p_0 & q_1 & -p_0 & 0 & 0 & 0 & 0 & 0 & 0 & 0 & 0 & 0 & 0 & 0 \\
-l_2 & -p_1 & -l_1 & -p_0 & q_3 & -p_0 & -l_1 & -p_1 & -l_2 & 0 & 0 & 0 & 0 & 0 & 0 & 0 \\
0 & 0 & 0 & 0 & -p_0 & q_1 & -p_0 & 0 & -p_1 & 0 & 0 & 0 & 0 & 0 & 0 & 0 \\
-p_2 & 0 & 0 & 0 & -l_1 & -p_0 & q_2 & -p_0 & -l_1 & 0 & 0 & 0 & 0 & 0 & 0 & 0 \\
0 & 0 & 0 & 0 & -p_1 & 0 & -p_0 & q_1 & -p_0 & 0 & 0 & 0 & 0 & 0 & 0 & 0 \\
-2l_3 & 0 & -p_2 & 0 & -l_2 & -p_1 & -l_1 & -p_0 & q_4 & -p_0 & -l_1 & -p_1 & -l_2 & 0 & -p_2 & 0 \\
0 & 0 & 0 & 0 & 0 & 0 & 0 & 0 & -p_0 & q_1 & -p_0 & 0 & -p_1 & 0 & 0 & 0 \\
-p_2 & 0 & 0 & 0 & 0 & 0 & 0 & 0 & -l_1 & -p_0 & q_2 & -p_0 & -l_1 & 0 & 0 & 0 \\
0 & 0 & 0 & 0 & 0 & 0 & 0 & 0 & -p_1 & 0 & -p_0 & q_1 & -p_0 & 0 & 0 & 0 \\
-l_2 & 0 & 0 & 0 & 0 & 0 & 0 & 0 & -l_2 & -p_1 & -l_1 & -p_0 & q_3 & -p_0 & -l_1 & -p_1 \\
-p_1 & 0 & 0 & 0 & 0 & 0 & 0 & 0 & 0 & 0 & 0 & 0 & -p_0 & q_1 & -p_0 & 0 \\
-l_1 & 0 & 0 & 0 & 0 & 0 & 0 & 0 & -p_2 & 0 & 0 & 0 & -l_1 & -p_0 & q_2 & -p_0 \\
-p_0 & 0 & 0 & 0 & 0 & 0 & 0 & 0 & 0 & 0 & 0 & 0 & -p_1 & 0 & -p_0 & q_1
\end{bmatrix}$$

$$(7.14)$$

In particular, the dark-shaded links in Fig.(2.2) correspond to p_i, while the green-shaded ones again refer to l_i, which may be originally absent but emergent in HNNP. The determinant of $L_g^{(NP,6)}$ can be evaluated by using the identity in Eq.(2.8) to write

$$\left[\det L_g^{(NP,6)}\right]^{-\frac{1}{2}} = C_g \iint\limits_{-\infty}^{\infty} \frac{dx_0 dx_{2^g-1}}{\pi} \exp\left\{-q_g\left(x_0^2 + x_{2^g-1}^2\right) + 4l_{g-1}x_0 x_{2^g-1}\right\}$$

$$\int\limits_{-\infty}^{\infty}\!\!\cdots\!\!\int \left(\prod_{i=1}^{g-1}\prod_{j=1}^{2^{g-i}} \frac{dx_{2^{i-1}(2j-1)}}{\sqrt{\pi}}\right) \tag{7.15}$$

$$\exp\left\{-\sum_{i=1}^{g-1} q_i \sum_{j=1}^{2^{g-i}} x_{2^{i-1}(2j-1)}^2 + 2\sum_{i=1}^{g-2} l_i \sum_{j=1}^{2^{g-i}} x_{2^{i-1}(2j-2)} x_{2^{i-1}(2j)}\right.$$

$$+2\sum_{i=1}^{g-2} p_i \sum_{j=1}^{2^{g-i-1}} \left(x_{2^{i-1}(4j-3)} x_{2^{i-1}(4j)} + x_{2^{i-1}(4j-1)} x_{2^{i-1}(4j-4)}\right)$$

$$\left. 2p_0 \sum_{j=1}^{2^{g-1}} x_{2j-1}(x_{2j-2} + x_{2j})\right\}.$$

To solve $\det L_g^{(NP,6)}$ recursively, we again integrate over all variables x with odd index (i.e. the $i=1$ term in the product):

$$\prod_{j=1}^{2^{g-2}} \iint\limits_{-\infty}^{\infty} \frac{dx_{4j-3} dx_{4j-1}}{\pi} \exp\left\{-q_1\left(x_{4j-3}^2 + x_{4j-1}^2\right) + 2p_1\left(x_{4j-3}x_{4j} + x_{4j-1}x_{4j-4}\right)\right.$$

$$\left.+2p_0\left[x_{4j-3}\left(x_{4j-4} + x_{4j-2}\right) + x_{4j-1}\left(x_{4j-2} + x_{4j}\right)\right]\right\}, \tag{7.16}$$

$$= \prod_{j=1}^{2^{g-2}} \frac{1}{q_1} \exp\left\{\frac{\left[p_1 x_{4j-4} + p_0\left(x_{4j} + x_{4j-2}\right)\right]^2 + \left[p_1 x_{4j} + p_0\left(x_{4j-2} + x_{4j-4}\right)\right]^2}{q_1}\right\}$$

$$= q_1^{-2^{g-2}} \exp\left\{2\frac{p_0^2 + p_1^2}{q_1}\left(x_0^2 + x_{2^k-1}^2\right) + 2\frac{p_0^2 + p_1^2}{q_1}\sum_{i=2}^{g-2}\sum_{j=1}^{2^{g-i-1}} x_{2^{i-1}(2j-1)2} + 2\frac{p_0^2}{q_1}\sum_{j=1}^{2^{g-2}} x_{(2j-1)2}^2\right.$$

$$\left. 2\frac{p_0^2 + p_0 p_1}{q_1}\sum_{j=1}^{2^{g-1}} x_{2j-2}x_{2j} + 4\frac{p_0 p_1}{q_1}\sum_{j=1}^{2^{g-2}} x_{(2j-2)2}x_{(2j)2}\right\}$$

Substituting back into Eq.(7.15) obtains:

$$\left[\det L_g^{(NP,6)}\right]^{-\frac{1}{2}} = C_g q_1^{-2^{g-2}} \int\!\!\!\int\limits_{-\infty}^{\infty} \frac{dx_0 dx_{2^{g-1}}}{\pi} \exp\left\{-\left[q_g - 2\frac{p_0^2 + p_1^2}{q_1}\right](x_0 + x_{2^{g-1}}) + 4l_{g-1}x_0 x_{2^{g-1}}\right\}$$

$$\int\limits_{-\infty}^{\infty}\!\!\!\cdots\!\!\int \left(\prod_{i=1}^{g-2}\prod_{j=1}^{2^{g-1-i}} \frac{dx_{2^i(2j-1)}}{\sqrt{\pi}}\right) \tag{7.17}$$

$$\exp\left\{-\sum_{i=2}^{g-2}\left(q_{i+1} - 2\frac{p_0^2 + p_1^2}{q_1}\right)\sum_{j=1}^{2^{g-1-i}} x_{2^i(2j-1)}^2 - \left(q_2 - 2\frac{p_0^2}{q_1}\right)\sum_{j=1}^{2^{g-2}} x_{2(2j-1)}^2\right.$$

$$+2\sum_{i=1}^{g-3} p_{i+1} \sum_{j=1}^{2^{g-i-2}} \left(x_{2^i(4j-3)}x_{2^i(4j)} + x_{2^i(4j-1)}x_{2^i(4j-4)}\right)$$

$$+2\sum_{i=2}^{g-3} l_{i+1} \sum_{j=1}^{g-i-1} x_{2^i(2j-2)}x_{2^i(2j)} + 2\left(l_2 + 2\frac{p_0 p_1}{q_1}\right)\sum_{j=1}^{2^{g-2}} x_{2(2j-2)}x_{2(2j)}$$

$$\left.+2\left(l_1 + \frac{p_0^2 + p_0 p_1}{q_1}\right)\sum_{j=1}^{2^{g-2}} x_{2(2j-1)}\left(x_{2(2j-2)} + x_{2(2j)}\right)\right\}$$

Substituting $x_i' = x_{2i}$, this expression that we identify

$$\begin{aligned}
q_1' &= q_2 - 2\frac{p_0^2}{q_1}, \\
q_i' &= q_{i+1} - 2\frac{p_0^2 + p_1^2}{q_1} \qquad (i \geq 2), \\
p_0' &= l_1 + \frac{p_0^2 + p_0 p_1}{q_1}, \\
p_i' &= p_{i+1} \qquad\qquad\quad (i \geq 1), \\
l_1' &= l_2 + 2\frac{p_0 p_1}{q_1}, \\
l_i' &= l_{i+1} \qquad\qquad\quad (i \geq 2).
\end{aligned} \tag{7.18}$$

The difference between the primed and unprimed quantities represents the step from the μ-th to the $\mu + 1$-st level in the RG recursion, with $0 \leq \mu < g$. As for HN3 and HN5 above, the recursion for the overall scale-factor C_g is

$$C_g' = C_g\, q_1^{-2^{g-\mu-2}}. \tag{7.19}$$

Initial conditions for Eq.(7.18-7.19) in the case of HNNP are:

$$
\begin{aligned}
C_g^{(0)} &= 1, \\
q_1^{(0)} &= 3 + \epsilon, \\
q_i^{(0)} &= 2i - 1 + \epsilon \quad (i \geqslant 2), \\
p_i^{(0)} &= 1 \qquad (i \geqslant 1), \\
l_i^{(0)} &= 0 \qquad (i \geqslant 1),
\end{aligned}
\tag{7.20}
$$

reflecting the fact that all sites in HNNP have a hierarchy-dependent, increasing degree of $k_i = 2i - 1$, $2 \leqslant i < g$, as for HN5 above, but instead with average degree 4. Here, too, the difference between q_i and q_{i+1} for $i \geq 2$ is constant throughout, $q_{i+1} - q_i = 2$, such that only the renormalization of q_1 and q_2 evolve nontrivially. Again, it remains $p_i \equiv 1$ for $i \geqslant 1$ at any step μ of the RG, in particular, $p_1^{(\mu)} \equiv 1$ throughout and only the backbone p_0 renormalizes nontrivially. Although all links of type l_i are initially absent in this network, under renormalization terms of type l_1 emerge while those for l_i for $i \geqslant 2$ remain zero at any step. These considerations reduce Eq.(7.18-7.19) to

$$
\begin{aligned}
C_g^{(\mu+1)} &= C_g^{(\mu)}[q_1^{(\mu)}]^{-2^{(g-\mu-2)}}, \\
q_1^{(\mu+1)} &= q_2^{(\mu)} - 2\frac{[p_0^{(\mu)}]^2}{q_1^{(\mu)}}, \\
q_2^{(\mu+1)} &= q_2^{(\mu)} + 2 - 2\frac{[p_0^{(\mu)}]^2 + 1}{q_1^{(\mu)}}, \\
p_0^{(\mu+1)} &= l_1^{(\mu)} + \frac{[p_0^{(\mu)}]^2 + p_0^{(\mu)}}{q_1^{(\mu)}}, \\
l_1^{(\mu+1)} &= 2\frac{p_0^{(\mu)}}{q_1^{(\mu)}}.
\end{aligned}
\tag{7.21}
$$

Then, abbreviating $q_\mu \equiv q_1^{(\mu)}$, $r_\mu \equiv q_2^{(\mu)}$, $p_\mu \equiv p_0^{(\mu)}$, and $l_\mu = l_1^{(\mu)}$, Eqs.(7.21) further simplify to

$$
\begin{aligned}
q_{\mu+1} &= r_\mu - 2\frac{p_\mu^2}{q_\mu}, \\
r_{\mu+1} &= r_\mu + 2 - 2\frac{p_\mu^2 + 1}{q_\mu}, \\
p_{\mu+1} &= l_\mu + \frac{p_\mu^2 + p_\mu}{q_\mu}, \\
l_{\mu+1} &= 2\frac{p_\mu}{q_\mu}.
\end{aligned}
\tag{7.22}
$$

Evolving the RG for $g-2$ steps results in a reduced network that consists of 4 sites, formerly in 0, 2^{g-2}, 2^{g-1}, $3\,2^{g-2}$. Hence the determinant for HNNP reads

$$
\begin{aligned}
det\left[\mathbf{L^{(NP)}} - \lambda\mathbf{1}\right] &= \frac{1}{\left[C_g^{(g-2)}\right]^2} \det
\begin{bmatrix}
r_{g-2} & -p_{g-2} & -2l_{g-2} & -p_{g-2} \\
-p_{g-2} & q_{g-2} & -p_{g-2} & 0 \\
-2l_{g-2} & -p_{g-2} & r_{g-2} & -p_{g-2} \\
-p_{g-2} & 0 & -p_{g-2} & q_{g-2}
\end{bmatrix} \\
&= \left[C_g^{(g-2)}\right]^{-2}\left\{-q_{g-2}\left(2l_{g-2}+r_{g-2}\right)\left[4p_{g-2}^2+q_{g-2}\left(2l_{g-2}-r_{g-2}\right)\right]\right\}.
\end{aligned}
\tag{7.23}
$$

For HNNP, Eq.(7.22) has a fixed point at $\mu \to \infty$, with $q_\infty = 5, r_\infty = 33/5, p_\infty = 2, l_\infty = 4/5$. A simple perturbation for small ϵ on Eq.(7.22) then yields [105]

$$
\begin{aligned}
q_\mu &\sim 5 + \epsilon 2^\mu Q_1, \\
r_\mu &\sim \frac{33}{5} + \epsilon 2^\mu Q_1 \frac{26}{25} \\
p_\mu &\sim 2 - \epsilon 2^\mu Q_1 \frac{2}{5}, \\
l_\mu &\sim \frac{4}{5} - \epsilon 2^\mu Q_1 \frac{4}{25}.
\end{aligned}
\tag{7.24}
$$

Here, $\left[C_g^{(g-2)}\right]^{-2} \sim \alpha^N$, where α is estimated to be $2.949007876\ldots$ at $g = 30$.

Initial conditions for Eq.(7.18-7.19) in the case of HN6 are:

$$
\begin{aligned}
C_g^{(0)} &= 1 \\
q_1^{(0)} &= 3 + \epsilon \\
q_i^{(0)} &= 4i - 3 + \epsilon \quad (i \geqslant 2) \\
p_i^{(0)} &= 1 \qquad (i \geqslant 1) \\
l_i^{(0)} &= 1 \qquad (i \geqslant 1)
\end{aligned}
\tag{7.25}
$$

reflecting the fact that all sites in HN6 have a hierarchy-dependent, increasing degree of $k_i = 4i-3 (2 \leqslant i < k)$ with average 6. The difference between q_i and q_{i+1} is constant throughout, here $q_{i+1} - q_i = 4$.

Only the renormalization of q_1 and q_2 evolve nontrivially, as before. Again, all p_i are non-zero, encompassing the backbone links ($i = 0$) and all levels of long-range links ($i \geqslant 1$). But it remains $p_i \equiv 1$ for $i \geqslant 1$ at any step μ of the RG, in particular, $p_1^{(\mu)} \equiv 1$ throughout; only the backbone p_0 renormalizes nontrivially. As for HN5, in HN6 bare links of type l_i are present in this network. Though, only l_1 renormalizes, as in HN5, while $l_i \equiv 1$ remains unrenormalized for all $i \geq 2$. Applying these considerations to Eq.(7.18-7.19) results in:

$$
\begin{aligned}
C_g^{(\mu+1)} &= C_g^{(\mu)} \left[q_1^{(\mu)} \right]^{-2^{(k-\mu-2)}}, \\
q_1^{(\mu+1)} &= q_2^{(\mu)} - 2\frac{\left[p_0^{(\mu)} \right]^2}{q_1^{(\mu)}}, \\
q_2^{(\mu+1)} &= q_2^{(\mu)} + 4 - 2\frac{\left[p_0^{(\mu)} \right]^2 + 1}{q_1^{(\mu)}}, \\
p_0^{(\mu+1)} &= l_1^{(\mu)} + \frac{\left[p_0^{(\mu)} \right]^2 + p_0^{(\mu)}}{q_1^{(\mu)}}, \\
l_1^{(\mu+1)} &= 1 + 2\frac{p_0^{(\mu)}}{q_1^{(\mu)}}.
\end{aligned}
\tag{7.26}
$$

Then, abbreviating $q_\mu \equiv q_1^{(\mu)}$, $r_\mu \equiv q_2^{(\mu)}$, $p_\mu \equiv p_0^{(\mu)}$, and $l_\mu = l_1^{(\mu)}$, Eqs. (7.26) reduce to

$$
\begin{aligned}
q_{\mu+1} &= r_\mu - 2\frac{p_\mu^2}{q_\mu} \\
r_{\mu+1} &= r_\mu + 4 - 2\frac{p_\mu^2 + 1}{q_\mu} \\
p_{\mu+1} &= l_\mu + \frac{p_\mu^2 + p_\mu}{q_\mu} \\
l_{\mu+1} &= 1 + 2\frac{p_\mu}{q_\mu}.
\end{aligned}
\tag{7.27}
$$

For HN6, Eq.(7.27) has a fixed point at $\mu \to \infty$ with $q_\infty = 5 + 2\sqrt{5}$, $r_\infty = 7 + 14/\sqrt{5}$, $p_\infty = 2 + \sqrt{5}$, and $l_\infty = 1 + 2/\sqrt{5}$. A simple perturbation for small ϵ on Eq.(7.27) then yields [105]

$$q_\mu \sim 5 + 2\sqrt{5} + \epsilon 2^\mu Q_1, \tag{7.28}$$

$$r_\mu \sim 7 + \frac{14}{\sqrt{5}} + \epsilon 2^\mu Q_1 \frac{14 - 4\sqrt{5}}{5},$$

$$p_\mu \sim 2 + \sqrt{5} - \epsilon 2^\mu Q_1 \frac{10 - 3\sqrt{5}}{10},$$

$$l_\mu \sim 1 + \frac{2}{\sqrt{5}} - \epsilon 2^\mu Q_1 \frac{12 - 5\sqrt{5}}{10}.$$

Again, $\left[C_g^{(g-2)}\right]^{-2} \sim \alpha^N$, where α for HN6 is estimated to be $4.097722948\ldots$ at $g = 30$.

7.1.3   RG for Spectra of Hierarchical Lattices

For hierarchical lattices, instead of providing a description of L_g for a specific g, we reconstruct the integral in Eq.(2.8) piece-by-piece with a simple algebra. As suggested by Fig.(2.6.c), in each RG-step the network consists a collection of graph-lets of the type shown in Fig.(2.6.d). By evaluating how one of those graph-lets renormalizes, we renormalize the whole network in one generic step! In that graph-let, the b inner vertices belong to the currently lowest level ($i = 0$) of the hierarchy that will be integrated out in the next RG-step. One of the two outer vertices is exactly one level higher ($i = 1$) as it would be integrated at the next step. The other outer vertex must be of some unspecified but higher level ($i > 1$). We can now define a helpful function pertaining to each bond, each of which is bound to have a vertex with $i = 0$ on one end and some vertex with $i > 0$ on the other. Its part of the integrand in Eq.(2.8) has the form

$$B_i(x, y) = C_i \exp\left\{-\frac{q_i}{2}x^2 - \frac{q_0}{2}y^2 + 2pxy\right\}, \tag{7.29}$$

such that the RG-step depicted in Fig.(2.6.d) amounts to

$$
\begin{aligned}
B'_{i-1}(x,z) &= \int \cdots \int_{-\infty}^{\infty} \prod_{j=1}^{b} \frac{dy_j}{\sqrt{\pi}} \, B_i(x,y_j) \, B_1(y_j,z), \\
&= C_i^b C_1^b \exp\left\{-\frac{b}{2}\left(q_i x^2 + q_1 z^2\right)\right\} \int \cdots \int_{-\infty}^{\infty} \prod_{j=1}^{b} \frac{dy_j}{\sqrt{\pi}} \, \exp\left\{-q_0 y_j^2 + 2p\left(x+z\right)y_j\right\}, \\
&= C_i^b C_1^b q_0^{-\frac{b}{2}} \exp\left\{-\frac{b}{2}\left(q_i - \frac{2p^2}{q_0}\right)x^2 - \frac{b}{2}\left(q_1 - \frac{2p^2}{q_0}\right)z^2 + 2b\frac{p^2}{q_0}xz\right\}, \\
&= C'_{i-1} \exp\left\{-\frac{q'_{i-1}}{2}x^2 - \frac{q'_0}{2}z^2 + 2p'xz\right\},
\end{aligned}
\tag{7.30}
$$

where unprimed parameters are μ-times renormalized while primes indicate $\mu + 1$-times renormalized parameters. From the last two lines, we can read off the RG-recursions at the μth step:

$$
\begin{aligned}
C_{i-1}^{(\mu+1)} &= \left(\frac{C_1^{(\mu)} C_i^{(\mu)}}{\sqrt{q_0^{(\mu)}}}\right)^b, \\
q_{i-1}^{(\mu+1)} &= b\left(q_i^{(\mu)} - \frac{2\left(p^{(\mu)}\right)^2}{q_0^{(\mu)}}\right), \\
p^{(\mu+1)} &= b\frac{\left(p^{(\mu)}\right)^2}{q_0^{(\mu)}},
\end{aligned}
\tag{7.31}
$$

for $i > 0$. Considering that initially, at $\mu = 0$ in the unrenormalized network, all vertex-weights defined in Eq.(7.29) are the same, $q_i^{(0)} \equiv 2$ for all i, the distinction between levels i in Eq. (7.31) disappears. Note that a vertex at level $i > 0$ contributes to the Gaussian integral $2b^i$-fold through respective factors B_i, and 2-fold for $i = 0$ by appearing in two such factors $B_{i'}$, $i' > 0$. In this manner, the lattice Laplacian at $\mu = 0$ in Eq.(2.8) receives its proper weights on its diagonal. Equally, $C_i^{(0)} = 1$ for all $i > 0$. Thus, defining $C_\mu = C_i^{(\mu)}$, $p_\mu = b^{-\mu} p^{(\mu)}$, and $q_\mu = b^{-\mu} q_i^{(\mu)}$ for all $i \geq 0$, we obtain:

$$
\begin{aligned}
C_{\mu+1} &= \left[\frac{C_\mu^2}{\sqrt{b^\mu q_\mu}}\right]^b, \qquad (C_0 = 1), \\
q_{\mu+1} &= q_\mu - 2\frac{p_\mu^2}{q_\mu}, \qquad (q_0 = 2 + \epsilon), \\
p_{\mu+1} &= \frac{p_\mu^2}{q_\mu}, \qquad (p_0 = 1).
\end{aligned}
\tag{7.32}
$$

Note that the recursions in Eq.(7.32) is not exactly identical to Eq.(7.31). The initial condition for $q_i^{(0)}$ Eq.(7.31) is, in fact,

$$q_i^{(0)} \;=\; 2 + \epsilon/b^i, \qquad 0 \le i < g, \tag{7.33}$$

$$q_k^{(0)} \;=\; 2 + 2\epsilon/b^k, \qquad i = g,$$

which does not allow to collapse the i-th hierarchy as in the Hanoi networks. However, in the Taylor expansion in small ϵ, order-by-order such a collapse is allowed. The difference between the $\left\{q_0^{(\mu)}, p^{(\mu)}\right\}$ from Eq.(7.32) and $\{q_\mu, p_\mu\}$ from Eq.(7.31) is

$$q_0^{(\mu)} - q_\mu \;\sim\; Q_1 \epsilon + Q_2 \epsilon^2 + Q_3 \epsilon^3 + \dots, \tag{7.34}$$

$$p^{(\mu)} - p_\mu \;\sim\; P_1 \epsilon + P_2 \epsilon^2 + P_3 \epsilon^3 + \dots \tag{7.35}$$

in which coefficients are generally constants dependent on parameter b. After $k - 1$ iterations, the network is renormalized to two end nodes, the Laplacian determinant is

$$
\det\left[\mathbf{L_g^{MK}} + \epsilon \mathbf{1}\right] \;=\; C_g^{-2} b^{2g} \det \begin{bmatrix} q_g/2 & -p_g \\ -p_g & q_g/2 \end{bmatrix}
$$
$$
= \; C_g^{-2} b^{2g} \left(q_g^2/4 - p_g^2\right), \tag{7.36}
$$

where the C_g^{-2} can be expressed in closed form,

$$
C_g^{-2} \;=\; \left(b^0 q_0\right)^{2^{g-1} b^g} \left(b^1 q_1\right)^{2^{g-2} b^{g-1}} \left(b^2 q_2\right)^{2^{g-3} b^{g-2}} \dots \left(b^{g-1} q_{k-1}\right)^{2^{g-g} b}
$$
$$
= \; \left(\prod_{\mu=0}^{g-1} b^{(2b)^{g-\mu} \mu/2}\right) \left(\prod_{\mu=0}^{g-1} q_\mu^{b\,(2b)^{g-1-\mu}}\right). \tag{7.37}
$$

The ansatz for fixed points of rescaled $\{q_\mu, p_\mu\}$ is

$$q_\mu \sim 2^{-\mu} \left(Q_0 + \epsilon 4^\mu Q_1 + \epsilon^2 4^{2\mu} Q_2 \dots\right),$$

$$p_\mu \sim 2^{-\mu} \left(Q_0/2 - \epsilon 4^\mu P_1/4 + \epsilon^2 4^{2\mu} P_2 + \dots\right). \tag{7.38}$$

The fixed point scaling of parameters q_μ and p_μ in Eq.(7.38) verifies the validity of approximations in Eq.(7.32), since the differences between the approximated and exact parameters in Eq.(7.34) will not affect the scaling of any quantity we consider. With respect to ϵ, we can calculate the jth derivative of determinant for any b.

7.2 Evaluation of Individual Eigenvalues with RG

We can use the power method, commonly used to numerically extract particular eigenvalues of a matrix, to obtain the largest eigenvalue of the Laplacian for HN3 analytically. The power method simply proceeds as follows: Choose any generic vector $\mathbf{x}_0$ (that is non-zero and not already an eigenvector associated with another eigenvalue), then the evolution of

$$\mathbf{x}_{t+1} = \frac{1}{\bar{\lambda}_t}\mathbf{L}\mathbf{x}_t, \tag{7.39}$$

converges to the eigenvector associated with the (absolute) largest eigenvalue (if unique) of any matrix $\mathbf{M}$, where

$$\bar{\lambda}_t = \|\mathbf{x}_t\| \tag{7.40}$$

ensures proper normalization of the evolving vector $\mathbf{x}_t$. The magnitude of that largest eigenvalue is provided by $\lambda_N = \lim_{t\to\infty} \bar{\lambda}_t$. Hence, analytically, we are faced with solving the fixed point equation

$$\mathbf{x}^* = \frac{1}{\lambda_N}\mathbf{L}\mathbf{x}^*, \tag{7.41}$$

which is typically hopeless in general. But in case of the very sparse, hierarchical Laplacian matrix for HN3, the set of $N = 2^k$ coupled linear equations defined by Eq.(7.41) can be solved again recursively. Then, we can write for Eq.(7.41):

$$
\begin{aligned}
0 &= (3 - \lambda_N)\, x_0 - x_{2^k-1} - x_1 - x_{2^{k-1}}, \\
0 &= (3 - \lambda_N)\, x_{2^{k-1}} - x_{2^{k-1}-1} - x_{2^{k-1}+1} - x_0, \\
0 &= (3 - \lambda_N)\, x_{2^{i-1}(4j-3)} - x_{2^{i-1}(4j-3)-1} - x_{2^{i-1}(4j-3)+1} - x_{2^{i-1}(4j-1)}, \\
0 &= (3 - \lambda_N)\, x_{2^{i-1}(4j-1)} - x_{2^{i-1}(4j-1)-1} - x_{2^{i-1}(4j-1)+1} - x_{2^{i-1}(4j-3)},
\end{aligned}
\tag{7.42}
$$

for all $1 \leq i < k$ and $1 \leq j \leq 2^{i-2}$. The recursion consists of solving for and eliminating all odd-index $(i = 1)$ variables. To that end, we re-write Eqs.(7.42) as

$$
\begin{aligned}
0 &= q_2\, x_{n-2} - p\,(x_{n-3} + x_{n-1}) - l\,(x_{n-4} + x_n) - x_+, \\
0 &= q_1\, x_{n-1} - p\,(x_{n-2} + x_n) - x_{n+1}, \\
0 &= q_2\, x_n - p\,(x_{n-1} + x_{n+1}) - l\,(x_{n-2} + x_{n+2}) - x_{n\pm4}, \\
0 &= q_1\, x_{n+1} - p\,(x_{n+2} + x_n) - x_{n-1}, \\
0 &= q_2\, x_{n+2} - p\,(x_{n+3} + x_{n+1}) - l\,(x_{n+4} + x_n) - x_-,
\end{aligned}
\tag{7.43}
$$

for all $n = 2(2j - 1)$, $j = 1, \ldots, 2^{k-2}$, where initially

$$
\begin{aligned}
q_1^{(0)} = q_2^{(0)} &= 3 - \lambda_N, \\
p^{(0)} &= 1, \\
l^{(0)} &= 0.
\end{aligned}
\tag{7.44}
$$

Solving for and eliminating all odd-indexed variables $x_{n\pm1}$, we find

$$
\begin{aligned}
0 &= \left(q_2 - \frac{2p^2 q_1}{q_1^2 - 1}\right) x_{n-2} - \left(l + \frac{p^2}{q_1 - 1}\right)(x_{n-3} + x_{n-1}) - \frac{p^2}{q_1^2 - 1}(x_{n-4} + x_n) - x_+, \\
0 &= \left(q_2 - \frac{2p^2}{q_1 - 1}\right) x_n - \left(l + \frac{p^2}{q_1 - 1}\right)(x_{n-2} + x_{n+2}) - x_{n\pm4}, \\
0 &= \left(q_2 - \frac{2p^2 q_1}{q_1^2 - 1}\right) x_{n+2} - \left(l + \frac{p^2}{q_1 - 1}\right)(x_{n+3} + x_{n+1}) - \frac{p^2}{q_1^2 - 1}(x_{n+4} + x_n) - x_-.
\end{aligned}
\tag{7.45}
$$

We relabel $x'_{n'+2} = x_{n+2}$, $x'_{n'+1} = x_n$, and $x'_{n'} = x_{n-2}$, and obtain

$$
\begin{aligned}
q_1' &= q_2 - \frac{2p^2}{q_1 - 1}, \\
q_2' &= q_2 - \frac{2p^2 q_1}{q_1^2 - 1}, \\
p' &= l + \frac{p^2}{q_1 - 1}, \\
l' &= \frac{p^2}{q_1^2 - 1},
\end{aligned}
\tag{7.46}
$$

considering which should be compared with Eqs.(2.10). Then, Eqs.(7.45) in terms of the primed quantities take on exactly the form of the (lower three) Eqs.(7.43) and the circle closes. The recursion

terminates after $k - 2$ steps with the equations

$$
\begin{aligned}
0 &= q_2^{(k-2)} x_0 - p^{(k-2)} (x_1 + x_3) - \left(2l^{(k-2)} + 1\right) x_2, \\
0 &= q_1^{(k-2)} x_1 - p^{(k-2)} (x_0 + x_2) - x_3, \\
0 &= q_2^{(k-2)} x_2 - p^{(k-2)} (x_1 + x_3) - \left(2l^{(k-2)} + 1\right) x_0, \\
0 &= q_1^{(k-2)} x_3 - p^{(k-2)} (x_0 + x_2) - x_1,
\end{aligned}
\tag{7.47}
$$

which lead to the constraint

$$
0 = q_2^{(k-2)} - 2l^{(k-2)} + 1.
\tag{7.48}
$$

Combining Eqs.(7.44), (7.46), and (7.48) provide an efficient procedure to determine the largest eigenvalue λ_N, albeit implicit. For instance, for $k = 2$, we can directly insert Eqs.(7.44) into Eq.(7.48) to find $\lambda_4 = 4$, for $k = 3$, we recur the initial conditions in Eqs.(7.44) once through Eqs.(7.46) before we apply the constraint in Eq.(7.48) to get

$$
0 = (3 - \lambda_8) - \frac{2(3 - \lambda_8)}{(3 - \lambda_8)^2 - 1} + \frac{2}{(3 - \lambda_8)^2 - 1} + 1
$$

with the solution $\lambda_8 = 4 + \sqrt{2} = 5.414\ldots$. Beyond that, a closed-form solution becomes quite difficult, and we have to resort to an implicit "shooting" procedure, which is nonetheless exponentially more efficient, $O(k = \log_2 N)$, than a numerical evaluation with the power method: simply choose a trial value for λ_N in Eqs.(7.44) and evolve the recursion in Eqs.(7.46) until the right-hand side of Eq.(7.48) has sufficiently converged, then vary the value of λ_N (using bisectioning or regula-falsi) such that the constraint in Eq.(7.48) is ever-better satisfied. In this way, we find

$$
\lambda_N = 5.37272879308215\ldots,
\tag{7.49}
$$

where in the end we need to evolve the recursions in Eq.(7.46) nearly 50 times before we can discern the convergence of the constraint. This corresponds to an accuracy in the asymptotic value of λ_N that would have required to evolve with the numerical power method the Laplacian for HN3 of size $N = 2^{50}$.

Similar to HN3, the renormalization group treatment with power method is also applied to HN5.

We obtain the recursions as

$$
\begin{aligned}
q' &= q + 2l - \frac{2p^2}{q-1}, \\
r' &= r - \frac{2p^2 q}{q^2 - 1}, \\
p' &= l + \frac{p^2}{q-1}, \\
l' &= 1 + \frac{p^2}{q^2 - 1},
\end{aligned}
\tag{7.50}
$$

the initial condition is

$$
\begin{aligned}
q^{(0)} &= 3 - \lambda_N, \\
r^{(0)} &= 2\,k - \lambda_N, \tag{7.51} \\
p^{(0)} &= 1, \tag{7.52} \\
l^{(0)} &= 1.
\end{aligned}
$$

The recursion terminates after $k-2$ steps with the equations

$$
\begin{aligned}
0 &= r^{(k-2)}\, x_0 - p^{(k-2)}\,(x_1 + x_3) - 2l^{(k-2)} x_2, \\
0 &= q^{(k-2)}\, x_1 - p^{(k-2)}\,(x_0 + x_2) - x_3, \tag{7.53} \\
0 &= r^{(k-2)}\, x_2 - p^{(k-2)}\,(x_1 + x_3) - 2l^{(k-2)} x_0, \\
0 &= q^{(k-2)}\, x_3 - p^{(k-2)}\,(x_0 + x_2) - x_1,
\end{aligned}
$$

which lead to the constraint

$$
0 = r^{(k-2)} + 2l^{(k-2)}.
\tag{7.54}
$$

Same method also apply to MKRG, in which the recursions

$$
\begin{aligned}
q_i' &= q_{i+1} - 2\frac{p^2}{q_0}, \\
p' &= \frac{p^2}{q_0},
\end{aligned}
\tag{7.55}
$$

the initial condition is

$$
\begin{aligned}
q_i^{(0)} &= 2 - \lambda_N/b^i, \qquad 0 \le i < k, \\
q_k^{(0)} &= 2 - 2\lambda_N/b^k, \tag{7.56} \\
p^{(0)} &= 1. \tag{7.57}
\end{aligned}
$$

The recursion terminates after k steps with the equations

$$
\begin{aligned}
0 &= b^k \left[q^{(k)}/2\, x_0 - p^{(k)} x_1 \right], \\
0 &= b^k \left[q^{(k)}/2\, x_1 - p^{(k)} x_0 \right],
\end{aligned}
\tag{7.58}
$$

which lead to the constraint

$$
0 = q^{(k)}/2 + p^{(k)}.
\tag{7.59}
$$

Bibliography

[1] Scott Aaronson and Andris Ambainis. Quantum search of spatial regions. In *Foundations of Computer Science, 2003. Proceedings. 44th Annual IEEE Symposium on*, pages 200–209. IEEE, 2003.

[2] E. Agliari, A. Blumen, and O. Mülken. Quantum-walk approach to searching on fractal structures. *Phys. Rev. A*, 82:012305, Jul 2010. doi: 10.1103/PhysRevA.82.012305. URL http://link.aps.org/doi/10.1103/PhysRevA.82.012305.

[3] Elena Agliari, Adriano Barra, Andrea Galluzzi, Francesco Guerra, Daniele Tantari, and Flavia Tavani. Retrieval capabilities of hierarchical networks: From dyson to hopfield. *Phys. Rev. Lett.*, 114:028103, Jan 2015.

[4] Elena Agliari, Adriano Barra, Andrea Galluzzi, Francesco Guerra, Daniele Tantari, and Flavia Tavani. Hierarchical neural networks perform both serial and parallel processing. *Neural Networks*, 66:22–35, 2015.

[5] Eric Akkermans, Gerald V Dunne, and Alexander Teplyaev. Physical consequences of complex dimensions of fractals. *EPL (Europhysics Letters)*, 88(4):40007, 2009.

[6] Réka Albert and Albert-László Barabási. Statistical mechanics of complex networks. *Rev. Mod. Phys.*, 74:47–97, Jan 2002.

[7] Réka Albert, István Albert, and Gary L Nakarado. Structural vulnerability of the north american power grid. *Physical review E*, 69(2):025103, 2004.

[8] Andris Ambainis, Eric Bach, Ashwin Nayak, Ashvin Vishwanath, and John Watrous. One-dimensional quantum walks. In *Proceedings of the thirty-third annual ACM symposium on Theory of computing*, pages 37–49. ACM, 2001.

[9] Andris Ambainis, Julia Kempe, and Alexander Rivosh. Coins make quantum walks faster. In *Proceedings of the sixteenth annual ACM-SIAM symposium on Discrete algorithms*, SODA '05, pages 1099–1108, Philadelphia, PA, USA, 2005. Society for Industrial and Applied Mathematics. ISBN 0-89871-585-7.

[10] José S. Andrade, Hans J. Herrmann, Roberto F. S. Andrade, and Luciano R. da Silva. Apollonian networks: Simultaneously scale-free, small world, euclidean, space filling, and with matching graphs. *Phys. Rev. Lett.*, 94:018702, Jan 2005.

[11] Albert-László Barabási and Réka Albert. Emergence of scaling in random networks. *Science*, 286(5439):509–512, 1999. ISSN 0036-8075.

[12] Albert-László Barabási and Réka Albert. Emergence of scaling in random networks. *science*, 286 (5439):509–512, 1999.

[13] Albert-Laszlo Barabasi and Zoltan N Oltvai. Network biology: understanding the cell's functional organization. *Nature reviews genetics*, 5(2):101–113, 2004.

[14] Albert-László Barabási, Erzsébet Ravasz, and Tamás Vicsek. Deterministic scale-free networks. *Physica A: Statistical Mechanics and its Applications*, 299(3-4):559–564, oct 2001.

[15] Mauricio Barahona and Louis M. Pecora. Synchronization in small-world systems. *Phys. Rev. Lett.*, 89(5):054101, Jul 2002. doi: 10.1103/PhysRevLett.89.054101.

[16] Mauricio Barahona and Louis M. Pecora. Synchronization in small-world systems. *Phys. Rev. Lett.*, 89:054101, Jul 2002.

[17] Riccardo Barbieri and Masanori Shimono. Criticality in large-scale brain fmri dynamics unveiled by a novel point process analysis. *Networking of Psychophysics, Psychology and Neurophysiology*, page 61, 2012.

[18] Marc Barthelemy. Spatial networks. *Physics Reports*, 499:1–101, October 2011.

[19] Danielle S. Bassett, Daniel L. Greenfield, Andreas Meyer-Lindenberg, Daniel R. Weinberger, Simon W. Moore, and Edward T. Bullmore. Efficient physical embedding of topologically complex information processing networks in brains and computer circuits. *PLoS Computational Biology*, 6(4):e1000748, apr 2010.

[20] John M Beggs. The criticality hypothesis: how local cortical networks might optimize information processing. *Philosophical Transactions of the Royal Society of London A: Mathematical, Physical and Engineering Sciences*, 366(1864):329–343, 2008.

[21] John M Beggs and Dietmar Plenz. Neuronal avalanches in neocortical circuits. *The Journal of neuroscience*, 23(35):11167–11177, 2003.

[22] A N Berker and S Ostlund. Renormalisation-group calculations of finite systems: order parameter and specific heat for epitaxial ordering. *Journal of Physics C: Solid State Physics*, 12(22):4961–4975, 1979.

[23] Norman Biggs. *Algebraic Graph Theory*. Cambridge University Press, 1974.

[24] Stefano Boccaletti, Vito Latora, Yamir Moreno, Martin Chavez, and D-U Hwang. Complex networks: Structure and dynamics. *Physics reports*, 424(4):175–308, 2006.

[25] S. Boettcher. Reduction of spin glasses applied to the Migdal-Kadanoff hierarchical lattice. *Euro. Phys. J. B*, 33:439, 2003.

[26] S. Boettcher and C. T. Brunson. Fixed point properties of the Ising ferromagnet on the Hanoi networks. *Phys. Rev. E*, 83:021103, 2011.

[27] S. Boettcher and B. Gonçalves. Anomalous diffusion on the Hanoi networks. *Europhysics Letters*, 84:30002, 2008.

[28] S. Boettcher, B. Gonçalves, and H. Guclu. Hierarchical regular small-world networks. *J. Phys. A: Math. Theor.*, 41:252001, 2008.

[29] S. Boettcher, J. L. Cook, and R. M. Ziff. Patchy percolation on a hierarchical network with small-world bonds. *Phys. Rev. E*, 80:041115, 2009.

[30] S. Boettcher, S. Falkner, and R. Portugal. Renormalization and scaling in quantum walks. *Phys. Rev. A*, 90:032324, 2014.

[31] S. Boettcher, S. Falkner, and R. Portugal. Relation between random walks and quantum walks. *Physical Review A*, 91:052330, 2015.

[32] Stefan Boettcher and Shanshan Li. Real-space renormalization group for spectral properties of hierarchical networks. *J. Phys. A*, 48:415001, 2015.

[33] Stefan Boettcher and Shanshan Li. Real-space renormalization group for spectral properties of hierarchical networks. *Journal of Physics A: Mathematical and Theoretical*, 48(41):415001, 2015.

[34] Stefan Boettcher and Shanshan Li. Evaluation of spectral zeta-functions with the renormalization group. *Journal of Physics A: Mathematical and Theoretical*, 50(12):125003, 2017.

[35] Stefan Boettcher, Vijay Singh, and Robert M. Ziff. Ordinary percolation with discontinuous transitions. *Nature Communications*, 3:787, 2012.

[36] Stefan Boettcher, Stefan Falkner, and Renato Portugal. Relation between random walks and quantum walks. *Phys. Rev. A*, 91:052330, May 2015.

[37] Stefan Boettcher, Shanshan Li, and Renato Portugal. Renormalization of the unitary evolution equation for coined quantum walks. *Journal of Physics A: Mathematical and Theoretical*, 50(12): 125302, 2017.

[38] Jean-Philippe Bouchaud and Antoine Georges. Anomalous diffusion in disordered media: Statistical mechanisms, models and physical applications. *Phys. Rep.*, 195:127–293, 1990.

[39] Shantanav Chakraborty, Leonardo Novo, Andris Ambainis, and Yasser Omar. Spatial search by quantum walk is optimal for almost all graphs. *Phys. Rev. Lett.*, 116:100501, 2016.

[40] Shu-Chiuan Chang, Lung-Chi Chen, and Wei-Shih Yang. Spanning trees on the Sierpinski gasket. *J. Stat. Phys.*, 126:649–667, 2007.

[41] Andrew M. Childs and Yimin Ge. Spatial search by continuous-time quantum walks on crystal lattices. *Phys. Rev. A*, 89:052337, May 2014.

[42] Andrew M. Childs and Jeffrey Goldstone. Spatial search by quantum walk. *Phys. Rev. A*, 70: 022314, 2004.

[43] Andrew M. Childs and Jeffrey Goldstone. Spatial search and the dirac equation. *Phys. Rev. A*, 70:042312, Oct 2004.

[44] Andrew M Childs, Enrico Deotto, Edward Farhi, Jeffrey Goldstone, Sam Gutmann, and Andrew J Landahl. Quantum search by measurement. *Physical Review A*, 66(3):032314, 2002.

[45] A. Clauset, C. Moore, and M. E. J. Newman. Hierarchical structure and the prediction of missing links in networks. *Nature*, 453:98–101, 2008.

[46] Reuven Cohen and Shlomo Havlin. Scale-free networks are ultrasmall. *Phys. Rev. Lett.*, 90: 058701, Feb 2003.

[47] S. Condamin, O. Benichou, V. Tejedor, R. Voituriez, and J. Klafter. First-passage times in complex scale-invariant media. *Nature*, 450:77, 2007.

[48] Wesley Cota, Silvio C. Ferreira, and Géza Ódor. Griffiths effects of the susceptible-infected-susceptible epidemic model on random power-law networks. *Phys. Rev. E*, 93:032322, Mar 2016.

[49] D. Dhar. The abelian sandpile and related models. *Physica A*, 263:4–25, 1999.

[50] Deepak Dhar. Lattices of effectively nonintegral dimensionality. *J. Math. Phys.*, 18:578, 1977.

[51] Eytan Domany, Shlomo Alexander, David Bensimon, and Leo P. Kadanoff. Solutions to the schrödinger equation on some fractal lattices. *Phys. Rev. B*, 28:3110–3123, 1983.

[52] S. N. Dorogovtsev, A. V. Goltsev, and J. F. F. Mendes. Critical phenomena in complex networks. *Rev. Mod. Phys.*, 80:1275–1335, 2008.

[53] Sergey N Dorogovtsev, Alexander V Goltsev, and José Ferreira F Mendes. Pseudofractal scale-free web. *Physical Review E*, 65(6):066122, 2002.

[54] Gerald V Dunne. Heat kernels and zeta functions on fractals. *J.Phys. A*, 45:374016, 2012.

[55] Stefan Falkner. *Quantum Walks and the Renormalization Group*. PhD thesis, Emory University, 2014.

[56] Edward Farhi and Sam Gutmann. Analog analogue of a digital quantum computation. *Physical Review A*, 57(4):2403, 1998.

[57] Edward Farhi, Jeffrey Goldstone, Sam Gutmann, and Michael Sipser. Quantum computation by adiabatic evolution. *arXiv preprint quant-ph/0001106*, 2000.

[58] Silvio C Ferreira, Claudio Castellano, and Romualdo Pastor-Satorras. Epidemic thresholds of the susceptible-infected-susceptible model on networks: A comparison of numerical and theoretical results. *Physical Review E*, 86(4):041125, 2012.

[59] K. H. Fischer and J. A. Hertz. *Spin Glasses*. Cambridge University Press, Cambridge, 1991.

[60] Iain Foulger, Sven Gnutzmann, and Gregor Tanner. Quantum search on graphene lattices. *Phys. Rev. Lett.*, 112:070504, Feb 2014.

[61] Masatoshi Fukushima and Tadashi Shima. On a spectral analysis for the sierpinski gasket. *Potential Analysis*, 1(1):1–35, 1992.

[62] Chikara Furusawa and Kunihiko Kaneko. Adaptation to optimal cell growth through self-organized criticality. *Phys. Rev. Lett.*, 108:208103, May 2012.

[63] Lazaros K Gallos, Hernán A Makse, and Mariano Sigman. A small world of weak ties provides optimal global integration of self-similar modules in functional brain networks. *Proceedings of the National Academy of Sciences*, 109(8):2825–2830, 2012.

[64] A. V. Goltsev, S. N. Dorogovtsev, J. G. Oliveira, and J. F. F. Mendes. Localization and spreading of diseases in complex networks. *Phys. Rev. Lett.*, 109:128702, Sep 2012.

[65] Robert B Griffiths. Nonanalytic behavior above the critical point in a random ising ferromagnet. *Physical Review Letters*, 23(1):17, 1969.

[66] Geoffrey Grimmett, Svante Janson, and Petra F. Scudo. Weak limits for quantum random walks. *Physical Review E*, 69:026119+, February 2004. doi: 10.1103/physreve.69.026119.

[67] Lov K. Grover. Quantum mechanics helps in searching for a needle in a haystack. *Phys. Rev. Lett.*, 79:325–328, 1997.

[68] S. Havlin and D. Ben-Avraham. Diffusion in disordered media. *Adv. Phys.*, 36:695–798, 1987.

[69] B. A. Hendrickson and R. Leland. A multilevel algorithm for partitioning graphs. In *Proceedings of Supercomputing '95*, 1995.

[70] M. Hinczewski and A. N. Berker. Inverted Berezinskii-Kosterlitz-Thouless singularity and high-temperature algebraic order in an Ising model on a scale-free hierarchical-lattice small-world network. *Phys. Rev. E*, 73:066126, 2006.

[71] Michael Hinczewski and A. Nihat Berker. Inverted berezinskii-kosterlitz-thouless singularity and high-temperature algebraic order in an ising model on a scale-free hierarchical-lattice small-world network. *Phys. Rev. E*, 73:066126, Jun 2006.

[72] B. D. Hughes. *Random Walks and Random Environments*. Oxford University Press, Oxford, 1996.

[73] Róbert Juhász, Géza Ódor, Claudio Castellano, and Miguel A Muñoz. Rare-region effects in the contact process on networks. *Physical Review E*, 85(6):066125, 2012.

[74] L. P. Kadanoff. Notes on Migdal's recursion formulas. *Ann. Phys.*, 100:359–394, 1976.

[75] Marcus Kaiser. A tutorial in connectome analysis: topological and spatial features of brain networks. *Neuroimage*, 57(3):892–907, 2011.

[76] U Kang, Charalampos Tsourakakis, Ana Paula Appel, Christos Faloutsos, and Jure Leskovec. Hadi: Fast diameter estimation and mining in massive graphs with hadoop. *ACM Trasactions on Knowledge Discovery from Data (TKDD)*, 5(2):8, 2008.

[77] Osame Kinouchi and Mauro Copelli. Optimal dynamical range of excitable networks at criticality. *Nature physics*, 2(5):348–351, 2006.

[78] Jon M Kleinberg. Navigation in a small world. *Nature*, 406(6798):845–845, 2000.

[79] Norio Konno. Quantum random walks in one dimension. *Quantum Information Processing*, 1: 345–354, 2002.

[80] J Kuczyński and H Woźniakowski. Estimating the largest eigenvalue by the power and lanczos algorithms with a random start. *SIAM journal on matrix analysis and applications*, 13(4):1094–1122, 1992.

[81] Vito Latora and Massimo Marchiori. Is the boston subway a small-world network? *Physica A: Statistical Mechanics and its Applications*, 314(1-4):109–113, nov 2002.

[82] Robert Legenstein and Wolfgang Maass. Edge of chaos and prediction of computational performance for neural circuit models. *Neural Networks*, 20(3):323–334, 2007.

[83] Shanshan Li. Griffiths phase on hierarchical modular networks with small-world edges. *Phys. Rev. E*, 95:032306, Mar 2017.

[84] Shanshan Li and Stefan Boettcher. Renormalization group for a continuous-time quantum search in finite dimensions. *Phys. Rev. A*, 95:032301, Mar 2017.

[85] R. Lyons. Asymptotic enumeration of spanning trees. *Combin. Probab. Comput.*, 14:491–522, 2005.

[86] Christoph Maas. Transportation in graphs and the admittance spectrum. *Discrete Applied Mathematics*, 16(1):31–49, 1987.

[87] Sergei Maslov and Kim Sneppen. Specificity and stability in topology of protein networks. *Science*, 296(5569):910–913, 2002. ISSN 0036-8075.

[88] David Meunier, Renaud Lambiotte, and Edward T. Bullmore. Modular and hierarchically modular organization of brain networks. *Frontiers in Neuroscience*, 4, 2010.

[89] David Meunier, Renaud Lambiotte, and Edward T Bullmore. Modular and hierarchically modular organization of brain networks. *Frontiers in neuroscience*, 4:200, 2010.

[90] A. A. Migdal. Recursion relations in gauge field theories. *J. Exp. Theo. Phys.*, 42:743–746, 1976.

[91] Henryk Minc. *Nonnegative matrices.* JSTOR, 1988.

[92] P. Moretti and M. A. Muñoz. Griffiths phases and the stretching of criticality in brain networks. *Nat. Comm.*, 4:2521, 2013.

[93] Paolo Moretti and Miguel A Muñoz. Griffiths phases and the stretching of criticality in brain networks. *Nature communications*, 4, 2013.

[94] Miguel A Muñoz, Róbert Juhász, Claudio Castellano, and Géza Ódor. Griffiths phases on complex networks. *Physical review letters*, 105(12):128701, 2010.

[95] Mark EJ Newman. The structure of scientific collaboration networks. *Proceedings of the National Academy of Sciences*, 98(2):404–409, 2001.

[96] Th M Nieuwenhuizen. Griffiths singularities in two-dimensional random-bond ising models: Relation with lifshitz band tails. *Physical review letters*, 63(17):1760, 1989.

[97] Takashi Nishikawa and Adilson E. Motter. Synchronization is optimal in nondiagonalizable networks. *Phys. Rev. E*, 73:065106, 2006.

[98] Matti Nykter, Nathan D Price, Maximino Aldana, Stephen A Ramsey, Stuart A Kauffman, Leroy E Hood, Olli Yli-Harja, and Ilya Shmulevich. Gene expression dynamics in the macrophage exhibit criticality. *Proceedings of the National Academy of Sciences*, 105(6):1897–1900, 2008.

[99] Géza Ódor. Spectral analysis and slow spreading dynamics on complex networks. *Physical Review E*, 88(3):032109, 2013.

[100] Géza Ódor. Localization transition, lifschitz tails, and rare-region effects in network models. *Phys. Rev. E*, 90:032110, Sep 2014.

[101] Géza Ódor. Slow, bursty dynamics as a consequence of quenched network topologies. *Physical Review E*, 89(4):042102, 2014.

[102] Géza Odor and Romualdo Pastor-Satorras. Slow dynamics and rare-region effects in the contact process on weighted tree networks. *Physical Review E*, 86(2):026117, 2012.

[103] Géza Ódor, Ronald Dickman, and Gergely Ódor. Griffiths phases and localization in hierarchical modular networks. *Scientific reports*, 5, 2015.

[104] Romualdo Pastor-Satorras and Alessandro Vespignani. *Evolution and structure of the Internet: A statistical physics approach*. Cambridge University Press, 2007.

[105] R. K. Pathria. *Statistical Mechanics, 2nd Ed.* Butterworth-Heinemann, Boston, 1996.

[106] Niklas Peinecke, Franz-Erich Wolter, and Martin Reuter. Laplace spectra as fingerprints for image recognition. *Computer-Aided Design*, 39(6):460–476, 2007.

[107] Dietmar Plenz and Tara C Thiagarajan. The organizing principles of neuronal avalanches: cell assemblies in the cortex? *Trends in neurosciences*, 30(3):101–110, 2007.

[108] M. Plischke and B. Bergersen. *Equilibrium Statistical Physics, 2nd edition*. World Scientifc, Singapore, 1994.

[109] Renato Portugal. *Quantum Walks and Search Algorithms*. Springer, Berlin, 2013.

[110] Alex Pothen, Horst D Simon, and Kang-Pu Liou. Partitioning sparse matrices with eigenvectors of graphs. *SIAM journal on matrix analysis and applications*, 11(3):430–452, 1990.

[111] R. Rammal. Spectrum of harmonic excitations on fractals. *J. Physique*, 45:191–206, 1984.

[112] Rammal Rammal and Gérard Toulouse. Random walks on fractal structures and percolation clusters. *Journal de Physique Lettres*, 44(1):13–22, 1983.

[113] Pierre Ramond. *Field Theory: A Modern Primer*. Westview Press, 1997.

[114] Erzsébet Ravasz and Albert-László Barabási. Hierarchical organization in complex networks. *Phys. Rev. E*, 67:026112, Feb 2003.

[115] Erzsébet Ravasz, Anna Lisa Somera, Dale A Mongru, Zoltán N Oltvai, and A-L Barabási. Hierarchical organization of modularity in metabolic networks. *science*, 297(5586):1551–1555, 2002.

[116] S. Redner. *A Guide to First-Passage Processes*. Cambridge University Press, Cambridge, 2001.

[117] Mikail Rubinov, Olaf Sporns, Jean-Philippe Thivierge, and Michael Breakspear. Neurobiologically realistic determinants of self-organized criticality in networks of spiking neurons. *PLoS Comput Biol*, 7(6):e1002038, 2011.

[118] Christophe H Schilling, David Letscher, and Bernhard Ø Palsson. Theory for the systemic definition of metabolic pathways and their use in interpreting metabolic function from a pathway-oriented perspective. *Journal of theoretical biology*, 203(3):229–248, 2000.

[119] Woodrow L Shew, Wesley P Clawson, Jeff Pobst, Yahya Karimipanah, Nathaniel C Wright, and Ralf Wessel. Adaptation to sensory input tunes visual cortex to criticality. *Nature Physics*, 11 (8):659–663, 2015.

[120] Tadashi Shima. On eigenvalue problems for the random walks on the sierpinski pre-gaskets. *Japan Journal of Industrial and Applied Mathematics*, 8(1):127–141, 1991.

[121] Robert Shrock and Fa Yueh Wu. Spanning trees on graphs and lattices in d dimensions. *Journal of Physics A: Mathematical and General*, 33(21):3881, 2000.

[122] Olaf Sporns, Dante R Chialvo, Marcus Kaiser, and Claus C Hilgetag. Organization, development and function of complex brain networks. *Trends in cognitive sciences*, 8(9):418–425, 2004.

[123] Alexander Teplyaev. Gradients on fractals. *Journal of Functional Analysis*, 174(1):128–154, 2000.

[124] Elmar Teufl and Stephan Wagner. Spanning trees of finite sierpiński graphs. *DMTCS Proceedings*, (1), 2006.

[125] Elmar Teufl and Stephan Wagner. On the number of spanning trees on various lattices. *J. Phys. A: Math. Theor.*, 43:415001, 2010.

[126] Elmar Teufl and Stephan Wagner. Resistance scaling and the number of spanning trees in self-similar lattices. *Journal of Statistical Physics*, 142(4):879–897, 2011.

[127] Salvador Elías Venegas-Andraca. Quantum walks: a comprehensive review. *Quantum Information Processing*, 11(5):1015–1106, 2012.

[128] Pablo Villegas, Paolo Moretti, and Miguel A Muñoz. Frustrated hierarchical synchronization and emergent complexity in the human connectome network. *Scientific reports*, 4, 2014.

[129] Thomas Vojta. Rare region effects at classical, quantum and nonequilibrium phase transitions. *Journal of Physics A: Mathematical and General*, 39(22):R143, 2006.

[130] Thomas Vojta and Jörg Schmalian. Quantum griffiths effects in itinerant heisenberg magnets. *Physical Review B*, 72(4):045438, 2005.

[131] Andre Voros. Spectral zeta functions. *Advanced Studies in Pure Mathematics*, 21:327–358, 1992.

[132] Andreas Wagner. The yeast protein interaction network evolves rapidly and contains few redundant duplicate genes. *Molecular biology and evolution*, 18(7):1283–1292, 2001.

[133] Andreas Wagner and David A Fell. The small world inside large metabolic networks. *Proceedings of the Royal Society of London B: Biological Sciences*, 268(1478):1803–1810, 2001.

[134] Sheng-Jun Wang and Changsong Zhou. Hierarchical modular structure enhances the robustness of self-organized criticality in neural networks. *New Journal of Physics*, 14(2):023005, 2012.

[135] D. J. Watts and S. H. Strogatz. Collective dynamics of 'small-world' networks. *Nature*, 393: 440–442, 1998.

[136] G. H. Weiss. *Aspects and Applications of the Random Walk*. North-Holland, Amsterdam, 1994.

[137] F Y Wu. The potts model. *Reviews of Modern Physics*, 54:235–268, 1982.

[138] Zhenhua Wu, Lidia A. Braunstein, Shlomo Havlin, and H. Eugene Stanley. Transport in weighted networks: Partition into superhighways and roads. *Phys. Rev. Lett.*, 96:148702, 2006.